AEC Rept. No. COO-2053-4

Technical Report

CONE FRUSTUMS IN A SHEAR LAYER

by

C. R. Symes and R. N. Meroney

Prepared for

U. S. Atomic Energy Commission
Contract AT (11-1)- 2053
Fallout Studies Branch
Division of Biology and Medicine
Atomic Energy Commission

Fluid Dynamics and Diffusion Laboratory
College of Engineering
Colorado State University
Fort Collins, Colorado 80521

August 1970

CER70-71CRS-RNM11

ABSTRACT

CONE FRUSTUMS IN A SHEAR LAYER

Experimental results are presented for wind tunnel tests on a series of increasingly tapered cone frustums placed in a shear flow. A cylinder of the same base diameter and altitude was also tested and used as a standard by which to compare the other models. Extensive pressure, drag and wake measurements are tabulated as well as diffusion characteristics derived from the release of radioactive gas from the models.

TABLE OF CONTENTS

LIST OF TABLES

LIST OF FIGURES

LIST OF FIGURES - Continued

LIST OF SYMBOLS

Geometric	Definition	Dimensions
X	Downstream co-ordinate	L
Y	Transverse co-ordinate	L
Z	Vertical co-ordinate	L
D	Base diameter	L
r	Local radius	L
h	Altitude (vertical height)	L
s	Slant height	L
k	Mean sand grain diameter	L
δ	Boundary layer thickness	L
A_x	Projected area	L^2
θ	Angular displacement from streamwise direction	---
ϕ	Frustum taper angle	---
Kinematic		
ρ	Density	ML^{-3}
ν	Kinematic viscosity	L^2T^{-1}
Dynamic		
$U_\infty\vert_z$	Freestream velocity at height z	LT^{-1}
$U_\infty\vert_{ref.ht.}$	Freestream velocity at the reference height	LT^{-1}
V_s	Kr-85 tracer source velocity	LT^{-1}
u	Average velocity behind the model	LT^{-1}
u_d	Defect velocity	LT^{-1}
u'	Turbulent velocity fluctuation about the mean	LT^{-1}

Symbol	Definition	Dimensions
Dynamic		
u_{rms}	Root mean square of the turbulent velocity fluctations about the mean $(u_{rms} = \sqrt{\overline{u'^2}})$	LT^{-1}
P_{total}	Total pressure	$ML^{-1}T^{-2}$
P_{static}	Static pressure	$ML^{-1}T^{-2}$
$P_{dynamic}$	Dynamic pressure	$ML^{-1}T^{-2}$
Diffusion		
χ	Local concentration (A - activity)	AL^{-3}
Q	Source concentration x source flow rate	AT^{-1}
K	Dimensionless isopleths $K = \dfrac{\chi U_\infty\vert_{ref.\ ht.} A_x}{Q}$	---
Parameter		
R	Reynolds number $R = \dfrac{U_\infty\vert_{ref.\ ht.} D}{\nu}$	---
C_d	Drag coefficient $C_d = \dfrac{\text{drag force}}{\text{(reference dynamic pressure) x projected area}}$	---
C_p	Pressure coefficient $C_p = \dfrac{\text{dynamic pressure}}{\text{reference dynamic pressure}}$	---
Electrical		
$\overline{E}$	Time averaged bridge D.C. voltage	V
E_o	Bridge voltage at zero flow	V
e_{rms}	Root mean square bridge A.C. voltage	V
Constants		
c	Pressure units conversion factor	---

Chapter I

INTRODUCTION

Nuclear power reactors are generally enclosed within a containment vessel to prevent the harmful release of solid contaminants or radioactive gases into the atmosphere. In the event of a power failure, the containment vessel may conceivably be ruptured allowing radioactive gases to escape and cause serious contamination downwind of the reactor complex. The unusual shape of some of the modern nuclear reactors prompted the present wind tunnel study of four increasingly tapered cone frustums situated in a shear layer. A cylinder of the same base diameter and altitude was also tested to afford a standard by which the other models could be judged. Radioactive Krypton-85 gas was released from various positions on the models at a rate that would simulate the "leakage" condition of the prototype.

Diffusion in the turbulent cavity-wake region of a building has been studied both in the field and wind tunnel with increasing interest during the past ten years. Many formulae for the prediction of downstream concentration distributions have been proposed in the light of these studies and Barry (1964) provides a summary of the more popular ones. Before discussing them in more detail a description of the nature of flow fields near an object is presented from Halitsky (1963).

> "The flow field around an object in a wind stream contains several zones having markedly different characteristics:
>
> a) Adjacent to each surface, and completely surrounding the object, there exists a thin boundary layer in which the mean velocity increases asymptotically from zero at the object surface to a slowly-varying value in the outer portion of the boundary layer.

b) Outside of the boundary layer and immediately downwind of the object, there exists an ellipsoidal region called a cavity in which the velocities and pressures are low and the turbulence is very high.

c) Surrounding the cavity and extending a considerable distance downwind from the object, there exists a paraboloidal region called a wake, characterized by ambient pressures and velocities lower than free-stream velocity.

d) Surrounding the wake and the upwind boundary layer, there exists a region called a displacement zone in which the fluid is displaced laterally as it flows around the object and the wake. The flow in the displacement zone is substantially potential, and is characterized by well-defined, curved streamlines, low turbulence, and pressures and velocities related through Bernoulli's Law along a streamline.

e) The object and its boundary layer, cavity, wake and displacement zone are all immersed in the background flow, which, in the case of a building resting on the ground, is the earth's boundary layer."

Figure 47 taken from the same paper, shows how these zones are arranged about his reactor shell model and help to give a clearer picture of the problem.

For turbulent diffusion phenomena in the lower atmosphere Sutton (1953) presents equations which have been used to estimate concentration distributions for an elevated point source, but the application of his equations is restricted because of many "ideal" assumptions. In an attempt to improve sensitivity to real conditions the Pasquill-Gifford (1963) semi-empirical formulae have become popular. A set of transverse and vertical standard deviations of the dispersion are plotted as functions of downstream distance. A "stability category" which classifies six kinds of possible atmospheric stratifications relates the various plume dispersions to different meteorological conditions, The primary drawback of this method is its insensitivity to the effect of terrain roughness.

Because of strong turbulent mixing motions, adverse pressure gradients and non-stationary fluctuations in the cavity-wake region, both the Sutton and Pasquill-Gifford methods fail to predict the dispersion of gases in the vicinity of a building.

Halitsky (in the paper just mentioned) did a wind tunnel study of the diffusion from a leak in the shell of a model of the EBR-II reactor situated at the Nuclear Reactor Testing Station at Idaho Falls, Idaho. He plots K-isopleths (isoconcentration lines) which are basically independent of scale but subject to some variation as a result of changes in Reynolds number and turbulence in the background flow. In a similar manner K-isopleths for the five models and their release configurations are plotted for the present paper. As Halitsky points out, the sensitivity to Reynolds number and turbulence is bound up in the rounded shape of the model which permits movement of the separation line and consequent variation of the cavity size. This condition does not exist for buildings with sharp edges, since the separation line is fixed at the edges for all Reynolds numbers. A field test for the same EBR-II reactor complex performed by Dickson (1967) found the range of K values for neutral atmospheres to be similar to those determined by Halitsky in the wind tunnel.

Hinds (1967) in a series of field tests to define the effect of wake flow on the variance of concentration concluded point source unobstructed ground level plumes are an upper bound on mean concentration and a lower bound on concentration variance. In general, wakes may decrease the mean concentration but certainly seem to increase the variance.

In view of the previous research a study into the effect of building shape on the downstream concentration distribution was undertaken. Data was taken for downstream distances as far as $X/D = 35$. The gas was released at the ambient temperature and no temperature stratification of the flow was included in the experiment.

The second half of the investigation was suggested by the similarity of the models shapes to those of one-sheet hyperboloid cooling towers. These cooling towers have been used in Europe for many years to cool condenser water at inland power stations. Because of the large size and thin shell of these structures (375 feet high, 100 feet base diameter and 5 inch wall thickness) large stresses arising from both self-weight and wind loading are present. The stresses due to self-weight can be accurately calculated, but the stresses due to wind loading are sensitive to changes in the pressure distribution around the tower.

Gardner (1969) considers the response of a cooling tower in a turbulent wind. He notes that one of the major experimental difficulties lies in obtaining a large Reynolds number in a wind tunnel. The dynamic similarity requirement that the Reynolds number be the same for both model and prototype is hard to achieve. Full size cooling towers have Reynolds numbers above 10^8, whereas most wind tunnels are only capable of 10^6 which may be below the critical point where turbulent flow separation occurs over a smooth model. (For a discussion of atmospheric simulation in a wind tunnel see Cermak (1966)).

Cowdrey and O'Neill (1956) measured the pressure distribution for a model cooling tower in a uniform flow and in a velocity gradient flow. The experiment was performed in a compressed air tunnel at two Reynolds numbers to check for any scaling effect. The maximum

Reynolds number ($11 \cdot 3 \times 10^6$/foot linear dimension of the model) was still only about one fifth of the potential full scale value for the uniform flow. There was no evidence of scale effect but for the velocity gradient situation some slight differences were found. Whether this was due to true scale effect or to the method of generating the velocity gradient was not decided.

D'Amato (1968) considered the pressure distribution on sphere-cone radomes in uniform and gradient flows and found that the maximum and minimum pressure coefficients decreased progressively as the velocity gradient increased. The greatest difference in pressure distribution occurred on the leeward side of the model, probably due to the alteration in the boundary layer separation produced by the gradient flow.

From a more general point of view Purdy (1967) in a study of wind loads on flat-top cylinders found that considerable differences in pressure distribution accompany changes in geometry (aspect ratio) and relative position with respect to the boundary layer. Love (1963) investigating the effect on the wake of an obstacle placed in a wall boundary layer found that varying size of the obstacle had little effect but variations in shape had a marked effect on the flow.

Chapter II

EXPERIMENTAL EQUIPMENT AND TECHNIQUES

1. Wind Tunnel

The experimental work was carried out in the Micro-meteorological Wind Tunnel at the Fluid Dynamics and Diffusion Laboratory, Colorado State University. The tunnel is shown in Figure 1. It is generally operated in the closed circuit mode. The air leaving the power-section slowly expands into a diverging duct which has heat exchanger coils located at its end which enable the air temperature to be raised or lowered if required. After turning 180 degrees the air enters the converging section through turbulence damping screens which eliminate all large scale velocity fluctuations. The flow at the entrance to the test section is then uniform with turbulence intensity of the order of 0.05%.

The test section is 80 ft long and has a cross-section of approximately 6 ft by 6 ft. The first 6 ft length of the test section has been roughened with 1/2" gravel attached to its perimeter in order to thicken the boundary layer and thus reduces the wall effects. Also a trip fence at the entrance is utilized to further stablize the flow patterns. The ceiling of the tunnel is adjustable for control of pressure gradient in the direction of flow, which in this study was adjusted to zero. The air speed can be controlled by varying both the RPM of the drive motor and the pitch of the propeller.

2. Models

Five models with varying degrees of taper were chosed for this study. The basic shape was a 6 inch diameter, 6 inch altitude cylinder. The remaining 4 models were cone frustums of the same base diameter and altitude as the cylinder. The largest frustum had a top diameter of 4 inches and will be referred to as frustum 4. The remaining frustums were of 3, 2 and 1 inch top diameter and will be referred to accordingly.

Two sets of the five models were turned from solid "Lucite". The first set had one top center hole and three side holes lying on a generator (Figure 7). All holes were 5/16 inch diameter and drilled normal to the surface. These were used for the diffusion and flow visualization sections of the experiment. The second set was used in the pressure distribution analysis and had 5 pressure tap holes of 1/16 inch diameter down the side and varying number across the top depending on the particular frustum (Figures 2 to 6). All tests except the flow visualization and the smooth cylinder study were run with the models covered in 80 D weight open coat cabinet paper. The ratio of boundary layer thickness to model height (δ/h) was 3.58 and tunnel blockage due to the model was less than 1%. The upstream velocity and turbulent intensity profiles are shown in Figure 46.

3. Concentration Profiles

(a) Calibration of the Source

Radioactive Krypton-85 gas was used as a tracer for obtaining the concentration distributions. It is produced by the nuclear fission of Uranium and averages about 5% of total Krypton. Since Kr-85 has a half-life of 10.6 years there is no appreciable decay during a diffusion experiment. The gas is diluted with air about one million times before use and in this form has properties essentially equivalent to those of air.

The activity of the diluted Kr-85 was determined by comparing it to the activity of a standard source. Thallium-204 of present activity 5.188 microcurie was the standard used. Kr-85 gas was passed through a small planchet situated under an end-window Geiger-Müller tube. The G.M. tube and planchet were enclosed in a massive iron shield (Figure 15). After determining the operating voltage of this G.M. tube, the Th-204 was put in the iron shield and the number of counts ("observed counts") in one minute noted several times using an electronic scaler set at the operating voltage. The gas planchet was then placed in exactly the same position and Kr-85 passed through it for five minutes. The observed counts/minute were taken several times and then the average of both sets of data computed. A correction for the G.M. tube "dead time" was then applied to give the exact counts/minute.

$$\text{Exact counts/minute} = \frac{\text{observed counts/minute}}{1 - (\text{dead time}) \times (\text{observed counts/minute})}$$

where the dead time = 100 microseconds.

Assuming that the activity of the two sources are in the same ratio as their exact counts/unit time the activity of the Kr-85 can be determined. Dividing this result by the volume of the planchet gives the concentration of the source in microcuries/cc. For a complete explanation of the techniques used in the diffusion analysis see Chaudry (1969).

(b) Concentration of the Sample

The object of the diffusion section of the experiment was to determine downstream concentration profiles for various model release configurations.

The Kr-85 was released from the model and sampled downstream with a set of eight probes, each drawing a sample at a fixed rate of 250 cc/minute. The source was released at 3500 cc/minute which is equivalent to a release velocity of 1.2 meters/second. To simulate the leakage situation this velocity (relative to the freestream velocity) is such that the source will not "jet" through the cavity formed by the model. The generally accepted criterion is $V_s/U_\infty|_{ref.ht.} << 1$, where V_s is the source velocity. For this study $V_s/U_\infty|_{ref.ht.}$ was approximately 1/4. The source was released for one minute during which time the samples were also taken. These samples were drawn by vacuum pump from the probes through a set of eight G.M. tubes. Each tube had a solenoid-operated valve in its line to the pump so that with the pump on the sampling could be started or stopped by activating the series-connected solenoids. After being counted the original sample was pushed out by the incoming sample and run back into the tunnel. A small door opening into the tunnel scavenged some of the air plus gas mixture out to the atmosphere to keep the background concentration to a reasonable level.

Four G.M. tubes were connected to an Ortec 484 Scaler in conjunction with a 482 Timer and 446 High Voltage Power Supply set at their operating voltage. The remaining four were connected to a Nuclear Chicago Corp. Model 192 A Ultrascaler set at their operating voltage. This enabled two tubes to be counted at once saving a considerable amount of time.

A program was written which corrected these observed counts to exact counts and presented the results in the dimensionless K-isopleth form

$$K = \frac{\chi U_\infty|_{ref.ht.}\ A_x}{Q}$$

where χ is the local concentration and Q is (source concentration) x (source flow rate).

(c) Measurement Configurations

The set of five models used for the diffusion analysis had one top hole and three side holes all normal to the surface and of 5/16 inch diameter. The models were turned from solid Lucite and the surface was covered with 80 D weight open coat cabinet paper to encourage turbulent separation. The source was released from the top, side top and side bottom holes with orientations to the freestream of $\theta = 0, 90, 180$ degrees.

The eight sampling probes were individually clamped to a rod which could be fixed to take either horizontal or vertical concentration profiles. By loosening the clamps the probes could be staggered for closer spacing in a region of interest (Figure 19).

For the ground concentration the individual probes were taped to the floor along the centerline at eight downstream (X) positions. The horizontal profiles were taken for six X co-ordinates while the vertical profiles were taken for eight X co-ordinates. All vertical profiles were taken on the centerline except for the $\theta = 90$ degrees release positions. In these cases the approximate maximum from the horizontal profile was selected and the vertical rake located at this point for each X.

4. Wake Profiles

A pitot-static tube in conjunction with the Trans-Sonics pressure meter was used to measure the mean dynamic pressure and hence the mean velocity. The pitot-static tube was attached to the upstream arm of the wind tunnel carriage. The tube could then be positioned anywhere in the test section by operating the carriage control console from outside the wind tunnel. The wake profiles were taken by traversing the tunnel (in the Y-direction) at various positions downstream of the model with the pitot-static tube. The D.C. output of the pressure meter and the displacement co-ordinate were plotted against each other using a Moseley Model 135 X-Y recorder.

5. Calculation of the Drag Force on a Frustum

The drag force on the set of models was determined in two different ways. Firstly by integrating the pressure distribution over the surface of a model and secondly by using a shear plate set flush with the wind tunnel floor.

(a) Integration of Pressure Distribution Method

The drag force on each model was determined by integrating the pressure distribution over the surface of the model. Each pressure tap was in turn connected to a Trans-Sonics Type 120 B Equibar Pressure Meter which measured the difference in total pressure at that point on the model and static pressure at a reference height in the freestream, 0.52 meters above the tunnel floor.

The model was set on a rotating table in the downstream end of the tunnel (Figure 21) and was rotated through 180 degrees in increments of 15 degrees. The pressure at each of the taps was recorded for each θ. A check on the symmetry of the flow over the model was made by rotating the model through 360 degrees and comparing the pressure distribution on each side of the model. It was decided that the flow was sufficiently symmetrical to measure the pressure distribution on one side of the model only.

(b) Shear Plate Method

The second method involved a shear plate which is shown in Figure 25. The shear plate was made of aluminum plate which had dimensions 0.635 cm x 59.6 cm x 59.0 cm. This plate was separated from the foundation plate by three chrome-steel balls. The ball diameter was 0.635 cm. Two stainless steel restoring arms, 0.317 cm x 1.27 cm x 45.6 cm each, were used. One end of the arm was attached to the shear plate and the other to the foundation plate. Four semi-conductor strain gages, one to each side of the restoring arm, were installed at 1.27 cm from the end of the restoring arm which was attached to the foundation plate.

To reduce friction the balls rolled between hardened tungsten-colbalt disks which were imbedded in the shear plate and in the foundation plate. The shear plate was able to move back and forth in a horizontal plane only, and had a natural frequency of 6 Hz. The construction of the plate is shown in Figure 23.

When a horizontal force is applied to the shear plate, the plate will displace according to the spring constant of the restoring arms and the magnitude of the applied force. It was experimentally proven that the shear plate will return to its original position after the applied force is removed. The bridge formed by the four strain gages was driven by an 8 volt D.C. power supply and the bridge output was measured with a D.C. micro-ammeter. The shear plate could measure a drag force ranging from 0.1 to 2000 grams.

By placing a false floor in the wind tunnel, the shear plate was set such that only the model projected into the freestream. The shear plate was calibrated on location by applying a known horizontal force to the plate and recording the bridge output in millivolts. Figure 93 shows the arrangement together with the calibration curve. The shear force on the plate (without the model) due to the freestream velocity was allowed for by adjusting the bridge balance for zero output on the millivolt-ammeter.

6. Turbulence Intensity Measurement

The turbulent field associated with the turbulent separation of each model was investigated using a Disa Constant Temperature Anemometer Type 55A01.

In the conventional manner the Bridge D.C. voltage $(\overline{E})$ giving the mean flow velocity and the Bridge A.C. voltage rms (e_{rms}) giving the rms value of the velocity fluctuations were measured. Assuming a linear relationship between the electrical power input to the transducer (a hot wire) and the square root of the flow velocity (King's law), the longitudinal turbulence intensity may be expressed as

$$\left.\frac{u_{rms}}{U_\infty}\right|_z = \frac{4\overline{E}^2}{\overline{E}^2 - E_o^2} \frac{e_{rms}}{\overline{E}} \quad .$$

E_o is the bridge voltage at zero flow velocity and the overbar denotes time-averaged values.

Measurements were taken at $Z/D = 0.66$ for two downstream (X) positions. Table II gives the turbulence intensity at these positions which are plotted in Figures 106 and 107.

7. Flow Visualization

In the final section of the investigation the flow about the models was examined using titanium tetrachloride released through the top and side middle holes of the models. Titanium tetrachloride liquid was placed in a pressure container to which a small pump was connected. With the pump on, air bubbled through the liquid and the dense white gas generated was tapped from the top of the container through a valve to the model. To improve the definition of the smoke photographs the freestream velocity was lowered from 4.7 meters/sec to 2.2 meters/sec and a parallel-beam lighting system was set up in the tunnel downstream of the models.

A Graphlex Speed Graphic camera using Polaroid 3000 speed-4x5 land film was positioned outside the tunnel and focused through the glass window of the tunnel.

Chapter III

EXPERIMENTAL THEORY AND RESULTS

1. Diffusion Characteristics

K-isopleths, dimensionless parameters describing the local downstream concentrations were computed for each model and release configuration. These values were plotted against Z/D in the case of vertical concentration profiles and against Y/D in the case of horizontal concentration profiles. For a particular K value (the four chosen were 0.5, 0.2, 0.1 and 0.05) the Z/D or Y/D co-ordinate was picked off from the smoothed curves. By plotting the corresponding co-ordinate for a particular K value against downstream distance (X/D) isoconcentration lines were formed for each model and release configuration (Figures 55 to 89). The ground concentration data was also put into K-isopleth form (on log-log paper) and Figures 48 to 54 give the K values for all models for a particular release configuration. As expected the model with the largest projected area (viz., the cylinder) has the largest defect velocity (see Figure 90) and the largest cavity. This would imply larger downstream ground concentrations which is generally observed in the ground concentration figures. For the different models varying concentrations in the cavity region ($X/D < 2\frac{1}{2}$) are observed but for the near wake ($10 < X/D < 20$) and far wake regions ($X/D > 20$) these concentrations converge to straight lines of almost constant slope for all models and all release configurations (Figures 48 to 54). The average value of the slope is -0.95.

It is interesting to note the lower ground concentrations for $X/D < 10$ for the frustums compared to the cylinder for top and side top releases (Figures 48 to 51). This is believed due to the effect of frustum taper. The increasing taper of the frustums tends to deflect the released gas higher into the freestream. (The smoke photographs also show this). Thus for elevated releases lofting of the plume due to frustum taper causes lower ground concentrations (cf. the cylinder) near the models. This effect was not present for side bottom releases where the rate of downstream dilution was almost constant for all models.

In the EBR-II field study by Dickson (1967) the ground concentrations are plotted in the same way as in Figures 48 to 54. For $X/D < 15$ Dickson fits straight lines of slope -0.6 to these curves. As just discussed, the effect of frustum taper on ground concentration for top and side top releases makes fitting of a general straight line to these curves unreasonable. It is possible, however, to fit straight lines to the side bottom release curves (Figures 52 to 54). The slope of -0.95 is again steeper then that fitted by Dickson.

One anomaly in the overall picture is the side bottom $\theta = 0^o$ release where the projected area effect is almost exactly reversed. The cylinder has the lowest ground concentration and the smaller frustums the highest. In the case of the cylinder the gas is being injected into the upstream part of the horseshoe vortex system developed at the base of the upstream face of the cylinder and is then swept downstream outside the cavity formed by the model. Roper (1965) has a good picture of this effect for the cylinder. Possibly this upstream vortex is lost after a certain amount of frustum taper explaining the increased center line ground concentrations of the more tapered frustums.

Turning now to the vertical and horizontal isoconcentration lines of Figures 55 to 89 consider first the top release configuration. The isoconcentration lines show that the shape of the model has almost no effect on the final plume height but that plume rise rate did tend to decrease slightly with decrease in model size. As expected the plume width decreased with decrease in model projected area. This can easily be verified by observation or by considering the ordinate of Figures 55 to 89 for a fixed K value curve. The release configuration having the most marked effect on plume width was the side bottom $\theta = 0^{o}$ position. The rate of plume width growth was much greater for the cylinder and frustum 4 than for the other frustums (Figures 75 to 79). The explanation for this was tendered in the ground concentration discussion for the same release configuration. Gas is leaked into the upstream horseshoe vortex system that is generated by the two larger models (cylinder and frustum 4). It is entrained in this regime and swept downstream in the "legs" of this vortex system causing the very sudden plume width growth observed. The crowding of the isoconcentration lines for the cylinder and frustum 4 is due to this entrainment. In the change from frustum 4 to frustum 3 it seems that the upstream horseshoe vortex system present for the cylinder and frustum 4 is lost and this loss also deprives the wake of some of its high velocity component around the side of frustum 3. This line of thinking would agree with the defect parameter for $Z/D = 1/3$, $2/3$ of Figures 90 and 91 where repeated data analysis failed to bring the defect curve for frustum 3 below that of frustum 4, as would be expected due to the smaller projected area.

An estimation of the average K value at the end of the cavity region has been proposed by Halitsky where he considers the average concentration at the end of the cavity to be approximately the source strength divided by the total volume flow. The wake area at the end of the cavity is assumed to be twice the model projected area and the average velocity across the section to be half the freestream velocity. On this basis the average K value is unity. (For discussion of this see Yang (1970)). For the cylinder the average K value is 0.61. Barry (1964) in his summary of estimation formulae gives the average K value a range of 0.5 to 2 for the various methods he describes.

It is obvious from the isoconcentration curves that model shape effects are predominantly reflected in plume width changes. Both side top and bottom releases for all θ have little effect on the final plume height $(X/D > 30)$; however faster plume rise was noted for the side bottom releases and especially the $\theta = 0^{\circ}$ orientation. The highest plumes occurred when the gas was leaked directly into the cavity $(\theta = 180^{\circ})$ from either the side top or side bottom positions. This plume height and corresponding plume width growth decreased with decreasing model projected area (due to decreasing cavity size).

The final major conclusion to be drawn from this section is from the $\theta = 90^{\circ}$ orientations. Here again there was little change in final plume height for side top and side bottom releases for each model and between all models. The plume height tended to decrease with decreasing model projected area. The asymmetry of the horizontal plume was much more pronounced in the side bottom than in the side top release. This is due to the increased velocity near the top of the models tending to wash out this effect.

2. Wake Profiles

Using the wake profiles taken at $Z/D = 0, 1/3, 2/3, 1$ for X/D positions of 1/2, 1, 1 1/2, 2, 2 1/2 a parameter describing the mean velocity field downstream of a model was formed.

$U_\infty|_Z$ the free stream velocity at a fixed Z was chosen as a reference velocity. u, the average velocity behind the model was computed by graphically integrating under the wake profile and dividing by the interval of integration.

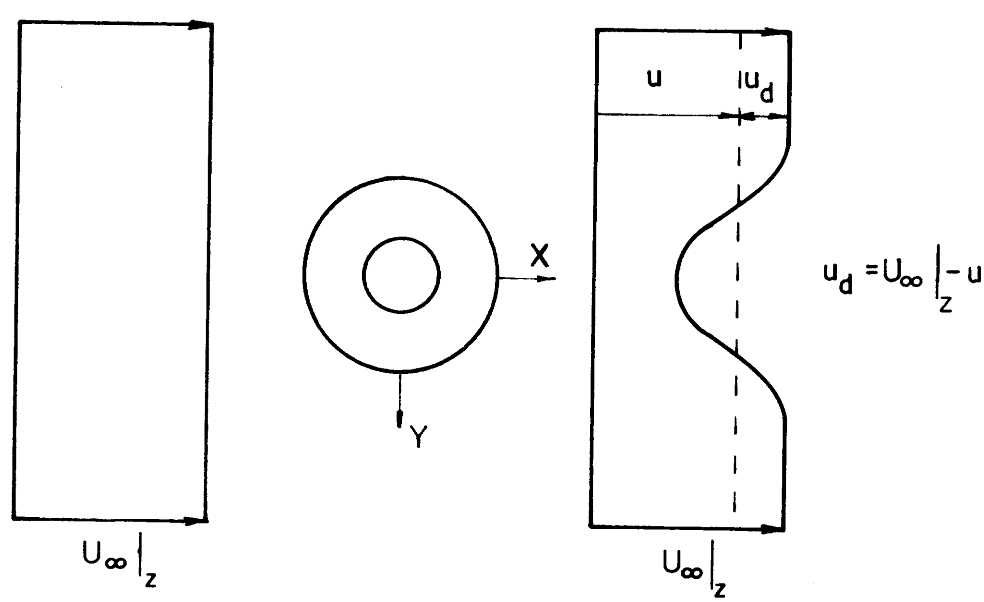

For each model and each wake profile position the ratio $u_d/U_\infty|_Z$ was calculated and graphed for Z/D = constant. Figures 90 to 92 show the curves for $Z/D = 1/3, 2/3, 1$. The $Z/D = 0$ graph is omitted because it was not possible to obtain any consistency in the $u_d/U_\infty|_Z$ parameter. This is because the large velocity gradient close to the floor make consistent vertical location of the probe critical. Although the probe was positioned to within 2 mm it is felt that close to the floor this was not sufficiently accurate.

$U_\infty|_Z$ increases and u_d decreases (due to the frustum taper) as Z/D increases implying an overall decrease in $u_d/U_\infty|_Z$ values for increasing Z/D. This trait is reflected in Figures 90, 91, 92. At a particular Z/D the parameter increases then decreases for increasing X/D. Assuming that $U_\infty|_Z$ is a constant this means that u_d at first increases then decreases downstream. Furthermore, as the frustum size decreases this maximum $u_d/U_\infty|_Z$ moves towards smaller X/D values.

This behavior is more easily understood by considering the changes in the velocity u. The trends of u_d follow directly from this. The velocity of the flow separating at the separation point is a maximum close to the model. When this high velocity component combines with the dead air region directly behind the model it decays quickly in a short distance downstream. The average velocity (u) behind the model thus decreases quickly from its maximum to its minimum in this region. At this point the tendency of the free stream to wash out upstream disturbances starts to bring the average velocity level up to the free stream values and this effect continues all the way downstream.

From Figures 90 and 91 the value of the defect parameter for the cylinder changes little with Z/D whereas for the frustums it decreases at each Z/D due to the decrease in projected area of the frustums. For the cylinder at $Z/D = 1$ the trailing vortices described by Roper in the following section produce a sharp increase in u corresponding to the sharp decrease in u_d in Figure 92.

The averaging process applied to the wake profiles to obtain $U_\infty|_Z$ and u was such that the maximum possible error (roughly three standard deviations) was 0.02. In Figures 90 and 91 where the defect parameter is higher for frustum 3 than for frustum 4 (contrary to expectation) the error does enclose these values. Even though this is the case it was felt that there was another reason for this behavior. It was not until after the diffusion analysis that the effect of frustum taper on the upstream horseshoe vortex suggested itself. As explained in the previous section it is quite probable that the horseshoe vortex system generated close to the ground by a cylinder in a shear flow was also present for the largest frustum (frustum 4) but that after a certain amount of taper the strength of this vortex and its downstream "legs" is diminished. This would explain how the average velocity behind frustum 4 could be higher than that behind frustum 3 (despite the larger projected area). This conclusion would lead to a "transition" concept where after a certain amount of taper one sees an increase in the defect velocity behind the frustums before it again starts dropping due to the decreasing projected area of the models.

3. Drag Calculations and Pressure Coefficients

The dynamic pressure data described in Chapter II was used to calculate the drag coefficients and pressure coefficients for each model. In the calculation of drag force the dynamic pressure was considered to act on an incremental area of the model surface projected normally to the streamwise direction.

The total force in the streamwise direction (the "drag force") was then obtained by integrating over this projected area of the model.

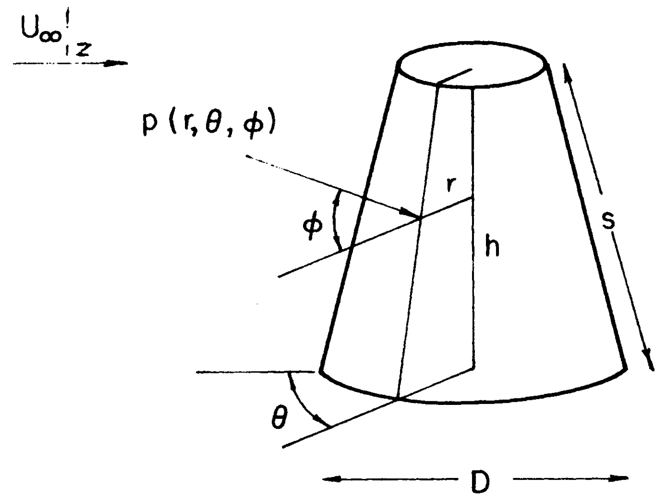

From the diagram, the drag force is given by

$$c \int\int p(r,\theta,\phi)\ r\ \cos\theta\ \cos\phi\ d\theta\ ds$$

where c is a constant, θ is the angular displacement of the line of pressure taps from the streamwise direction and ϕ is the angle between the normal to the surface (the pressure vector) and a plane parallel to the wind tunnel floor. Table I gives the algebraic streamwise component of force per Δh at each θ for a particular pressure tap. These are summed to give a drag force per Δh on the frustum at that pressure tap. By considering a frustum as being composed of a stack of frustum-shaped disks, each disk having one pressure tap in its side, a distribution of force per Δh on a model can be plotted. These curves were integrated graphically using a planimeter and the final value was half of the total drag force on the model.

The drag forces determined from the pressure distribution approach and the shear plate method are shown in Table I. Considering the symmetry approximation and the pressure measurement difficulty of the former method, the results are in good agreement (within 11%).

From the drag forces and angular pressure distributions the drag and pressure coefficients are easily computed. The drag coefficients for the cylinder and the four frustums are also listed in Table I.

For an infinite cylinder in a uniform flow at the test Reynolds number the drag coefficient is about 1.1. Table 15 of Goldstein (1965) gives 0.53 for the ratio of the drag coefficients of a unit aspect ratio cylinder to an infinite cylinder in a uniform flow. This implies that at the similar Reynolds number range the test cylinder in a uniform flow would have a drag coefficient of 0.58 (compared to 0.527 determined for the shear flow). Thus, it would seem that the velocity gradient in the test flow did not greatly effect the drag coefficient of the cylinder.

In the manner of Masch and Moore (1963) a local drag coefficient using the drag forces at each pressure tap of the cylinder was computed and plotted against Z (Figure 95). The local drag coefficient is evaluated using the streamwise drag force at each pressure tap in the expression for drag coefficient. This gives a distribution of drag coefficient down the side of a model. The velocity gradient parameter, $\frac{\Delta U}{\Delta Z}\frac{D}{U}$ of Masch and Moore was also evaluated for the present study. As with the results of the above paper the local drag coefficient is a maximum at the bottom of the cylinder and a minimum near the top. With reference to the velocity gradient this corresponds to a high coefficient at the low velocity end and a low coefficient at the high velocity end.

This variation is described by Masch and Moore in terms of the secondary flow, as follows:

"Along the upstream element of the cylinder (stagnation line), the stagnation pressure will be greater near the top of the cylinder, where the velocity is high, than at the bottom where the velocity is low. This will produce a pressure gradient along the axis of the cylinder and induce a flow along the stagnation line toward the base of the cylinder. In a similar way, the reduced pressure in the wake will be affected by the local approach velocity. At the top of the cylinder the pressure in the wake will be less than at the base of the cylinder, inducing a longitudinal flow towards the top of the cylinder, in the wake zone. The effect of these longitudinal flows on the local drag coefficient at various locations along the cylinder may be anticipated as follows. At the high-velocity end of the cylinder the longitudinal flow along the stagnation line would be diverting fluid away, thus reducing the pressure intensity on the upstream side of the cylinder. At the same time, the longitudinal flow in the wake region would be forcing fluid toward the top of the cylinder and thereby raising the pressure intensities on the downstream side of the cylinder. Both of these effects would act to reduce the drag force on the cylinder and, hence, to reduce the local drag coefficient near the top of the cylinder. It might be anticipated that the opposite effect would be true at the low-velocity end of the cylinder, and the local drag coefficient would be high. However, it is not necessarily true that this value will exceed that of the normal two-dimensional flow."

An alternative explanation is given by Roper (1965) in which he discusses the trailing vortex system which is a part of the overall vortex system generated by the presence of a finite cylinder in a boundary layer. This trailing vortex system is composed of two distinct vortices attached to the top side edges of the cylinder and which extend downstream. These trailing vortices feed high-energy fluid into the decreased pressure region of the wake near the top of the cylinder, thereby increasing the local pressure and smoothing the local pressure gradients. The effect of this smoothing is to delay the boundary layer separation near the top of the cylinder.

For an infinite cylinder of the same surface roughness (sand grain size to diameter ratio where $k/D = 2.5 \times 10^{-3}$), Figure 14 of Hoerner (1958) shows that the test Reynolds number was not sufficiently high to cause turbulent separation. From this figure it may be inferred that at this Reynolds number (considering an infinite cylinder) only a very exaggerated amount of surface roughness would have induced turbulent separation and that the surface roughness added may tend to increase the drag coefficient.

More tests were then carried out to look into this implication. The drag coefficient for the smooth cylinder (no sandpaper) was evaluated using the pressure distribution analysis and was indeed found to be less than that of the rough cylinder (Table I). The nature of the separation was resolved by running each sandpapered model at three Reynolds numbers. Firstly the test Reynolds numbers (around 3.7×10^4) and then at two higher ones. Figures 96 to 100 leave no doubt as to the separation that was occurring at the test Reynolds number. The flow was separating in a laminar fashion at θ approximately equal to 90^o. Figures 101 to 105 give the pressure coefficient distribution for three pressure taps down the side of a model. They show that laminar separation was occurring right down the side of each model. As Roper (1965) had mentioned, it appears that near the top of the cylinder the laminar separation may have been delayed a little by the shear flow. This effect was not noticed for the other models.

Unfortunately it is noted that while the test Reynolds number was not sufficiently high to achieve turbulent separation, a higher Reynolds number would have precluded the diffusion analysis using the Kr-85 tracer technique.

Figures 96 to 100 also show that as the frustum size decreased, the Reynolds number for transition to turbulent separation would have to increase.

The total drag coefficients were calculated using the drag forces derived from the shear plate since this was a much more sensitive method. Figure 94 shows the behavior for the five models and the interesting feature is the increase of the frustum 3 drag coefficient over that of frustum 4. This behavior reinforces the conclusions drawn from the diffusion and defect parameter analysis.

4. Turbulent Intensity

The turbulent intensity decay for the models is plotted for two downstream positions in Figures 106 and 107. It should be noted that the uncertainty in the longitudinal turbulent intensity (at high values) due to the three dimensional nature of the flow field was probably of the order of 20 to 30%. The hot wire output in this situation is also a function of the two other velocity components along and normal to the wire. The curves show that the turbulence level was always highest for the largest model (except for the dead air region behind the cylinder). The decay in the Y direction was very fast. By $X/D = 1/2$

nearly all the large scale turbulence had decayed to the background level. The decay in the X direction was much slower however, there being only a small decay between $X/D = 1/2$ and $X/D = 1$.

5. Flow Visualization

Figures 26 to 45 show the smoke photographs for the top and side middle hole releases. As the smoke was released from the side middle hole of all models it does not reveal the interesting region close to the ground. The pictures do show a marked upsweep in the smoke pattern for $\theta = 180^o$ which concurs with the increased plume rise growth noted from the isoconcentration lines for the side top and side bottom $\theta = 180^o$ releases. The decrease in cavity size with decreasing model size is shown in the top release sequence. The $\theta = 0^o$ release for all models shows the smoke being deflected higher up the models by increased frustum taper. This observation agrees with the increased plume rise rate for this release noted in the diffusion analysis.

Chapter IV

CONCLUSIONS

1. Model shape has very little effect on final plume height (i.e. plume height in the far wake) but causes marked changes in plume width growth. Final plume height was about twice the model height and total plume width was greater than five diameters by the time the near wake region was reached. Plume width growth decreased with decreasing model projected area.

2. Ground concentration decreases linearly with downstream distance (on log-log plot) at an almost constant slope in the near wake and far wake regions. The average slope was -0.95 for all models and all release configurations. For top and side top releases lofting of the plume due to frustum taper caused decreased ground concentrations for the frustums (cf. cylinder) for $X/D < 10$.

3. Releases from the side top and side bottom had little effect on the final plume height. Bottom releases caused the plumes to rise 1 1/2 to 2 times faster than top releases in the cavity and near wake regions. Releases directly into the cavity ($\theta = 180^{\circ}$) had the fastest plume rise rate.

4. Loss of the upstream part of the horseshoe vortex system due to increasing model taper was believed responsible for the changes in the diffusion character for the side bottom $\theta = 0^{\circ}$ release. The 1% increase in drag coefficient of frustum 3 over frustum 4 and the higher defect parameter values of frustum 3 are also attributed to this effect.

5. At the test Reynolds number the flow was separating in a laminar manner right down the side of all models.

6. The secondary flows generated by the velocity gradient appear to have a compensating effect with the result that there is little change (about a 7% decrease) in the drag coefficient of a unit aspect ratio cylinder in a shear flow compared to that for a similar cylinder in a uniform flow.

7. For decreasing model size the Reynolds number to cause turbulent separation must increase.

8. The turbulent field caused by the model presence decays very quickly in the transverse direction (the background level is reached within one diameter) whereas there is much slower decay in the downstream direction (virtually no decay until after one diameter downstream).

REFERENCES

Barry, P. J., "Estimation of Downwind Concentration of Airborne Effluents Discharged in the Neighborhood of Buildings," talk presented to Advisory Committee on the Safety of Particle Accelerators of the Atomic Energy Control Board, Atomic Energy of Canada Limited, Chalk River, Ontario, July, 1964.

Cermak, J. E., V. A. Sandborn, E. J. Plate, G. H. Binder, H. Chuang, R. N. Meroney and S. Ito, "Simulation of Atmospheric Motion by Wind Tunnel Flows," FDDL Report CER66JEC-VAS-EJP-GJB-HC-RNM-SI17, Colorado State University, May 1966.

Chaudry, F. H., and R. N. Meroney, "Turbulent Diffusion in a Stably Stratified Shear Layer," Technical Report C-0423-5, Colorado State University, 1969.

Cowdrey, C. F., and P. G. G. O'Neill, Report of Tests on a Model Cooling Tower for the C.E.A. Pressure Measurements at High Reynolds Numbers," NPL/Aero/316a, December 1956.

D'Amato, R. and W. R. Fanning, "Pressure Distributions on Sphere-Cone Radomes in Uniform and Gradient Flows," Tech. Note 1968-17, MIT Lincoln Lab, May 1968.

Dickson, C. R., G. E. Start, and E. H. Markee, Jr., "Aerodynamic Effects of the EBR-II Containment Vessed Complex on Effluent Concentration," USAEC Meteorological Information Meeting, September, 1967.

Gardner, N. J., "Response of Cooling Tower to Turbulent Wind," Proc. ASCE, J. of Struct. Div., Vol. 95, No. ST 10, October 1969.

Goldstein, S., "Modern Developments in Fluid Dynamics," Vol. II, Dover, New York, 1965.

Halitsky, J., J. Golden, P. Halpern, and P. Wu, "Wind Tunnel Tests of Gas Diffusion from a Leak in the Shell of a Nuclear Power Reactor and from a Nearby Stack," Geophys. Sciences Lab. Report No. 63-2, New York University, 1963.

Hinds, W. T., "On the Variation of Concentration in Plumes and Building Wakes," USAEC Meteorological Information Meeting, September, 1967.

Hoerner, S., "Fluid-Dynamic Drag," published by author, Midland Park, New Jersey, 1958.

Love, R. H., "An Investigation of the Effect of the Wall Boundary Layer on the Wake of an Obstacle Protruding from the Wall," TN BN-370, University of Maryland, 1963.

Masch, F. and W. Moore, "Drag Forces in Velocity Gradient Flow," Trans. ASCE, Vol. 128, Part I, 1963.

Pasquill, F., "The Estimation of the Dispersion of Wind-borne Material," Meteor. Mag., 90, 1963.

Purdy, D. M., F. J. Maher, D. Frederick, "Model Studies of Wind Loads on Flat-Top Cylinders," Proc. ASCE, J. of Struct. Div., Paper No. 5209, ST2, 1967.

Roper, A. T., "The Wake Region of a Circular Cylinder in a Turbulent Boundary Layer," M.S. Thesis, College of Eng., Colorado State University, Colorado, 1965.

Sutton, O. G., "Micrometeorology," McGraw Hill, New York, 1953.

Yang, B. T., "Gaseous Dispersion into Stratified Building Wakes," M.S. Thesis, College of Engineering, Colorado State University, 1970.

APPENDIX I

TABLES

TABLE I

RADIAL DISPLACEMENT (INCHES) OF PRESSURE TAPS FROM AXIS OF A MODEL

		Cylinder	Frustum 4	Frustum 3	Frustum 2	Frustum 1
Pressure tap number	2	1.0	1.0	0.5	0.5	0.692
	3	1.5	1.5	1.0	1.158	0.981
	4	2	2.082	1.621	1.395	1.269
	5	3	2.204	1.803	1.632	1.654
	6	3	2.326	1.085	1.949	2.423
	7	3	2.489	2.228	2.581	
	8	3	2.815	2.713		
	9	3				

DIFFERENCE IN TOTAL PRESSURE AT THE MODEL SURFACE AND STATIC PRESSURE AT THE REFERENCE HEIGHT (IN MILLIMETERS OF MERCURY) AT EACH PRESSURE TAP FOR EACH θ.

SMOOTH CYLINDER

	Pressure Tap Number								
θ	1	2	3	4	5	6	7	8	9
0	-0.021	-0.041	-0.049	-0.048	+0.034	+0.040	+0.041	+0.039	+0.029
15	-0.021	-0.041	-0.049	-0.047	+0.031	+0.037	+0.034	+0.032	+0.025
30	-0.021	-0.040	-0.049	-0.047	+0.015	+0.018	+0.019	+0.017	+0.011
45	-0.020	-0.035	-0.049	-0.047	-0.005	-0.005	-0.004	-0.005	-0.005
60	-0.020	-0.031	0.042	-0.047	-0.023	-0.024	-0.023	-0.023	-0.019
75	-0.021	-0.025	-0.033	-0.040	-0.029	-0.027	-0.025	-0.025	-0.025
90	-0.020	-0.020	-0.023	-0.026	-0.020	-0.019	-0.019	-0.019	-0.020
105	-0.020	-0.016	-0.015	-0.018	-0.021	-0.020	-0.020	-0.019	-0.019
120	-0.020	-0.014	-0.013	-0.014	-0.018	-0.019	-0.019	-0.019	-0.019
135	-0.020	-0.013	-0.011	-0.013	-0.018	-0.018	-0.020	-0.019	-0.017
150	-0.020	-0.011	-0.011	-0.012	-0.018	-0.018	-0.020	-0.020	-0.017
165	-0.020	-0.011	-0.011	-0.013	-0.018	-0.020	-0.020	-0.019	-0.015
180	-0.020	-0.011	-0.011	-0.014	-0.019	-0.020	-0.020	-0.019	-0.014

ROUGH CYLINDER

	Pressure Tap Number								
θ	1	2	3	4	5	6	7	8	9
0	-0.025	-0.044	-0.052	-0.050	+0.033	+0.037	+0.040	+0.035	+0.028
15	-0.025	-0.044	-0.054	-0.051	+0.028	+0.032	+0.033	+0.030	+0.024
30	-0.025	-0.041	-0.055	-0.053	+0.012	+0.012	+0.014	+0.013	+0.009
45	-0.025	-0.041	-0.052	-0.054	-0.008	-0.010	-0.010	-0.009	-0.007
60	-0.025	-0.035	-0.050	-0.054	-0.022	-0.027	-0.025	-0.023	-0.018
75	-0.025	-0.031	-0.039	-0.044	-0.036	-0.034	-0.034	-0.031	-0.032
90	-0.025	-0.026	-0.028	-0.032	-0.028	-0.026	-0.028	-0.028	-0.030
105	-0.025	-0.024	-0.020	-0.023	-0.026	-0.024	-0.024	-0.024	-0.026
120	-0.025	-0.019	-0.016	-0.018	-0.022	-0.023	-0.022	-0.023	-0.025
135	-0.025	-0.017	-0.015	-0.016	-0.023	-0.023	-0.023	-0.024	-0.025
150	-0.025	-0.015	-0.015	-0.016	-0.023	-0.024	-0.025	-0.025	-0.021
165	-0.025	-0.013	-0.014	-0.016	-0.024	-0.023	-0.024	-0.023	-0.021
180	-0.025	-0.013	-0.014	-0.016	-0.022	-0.023	-0.024	-0.021	-0.018

FRUSTUM 4

Pressure Tap Number

θ	1	2	3	4	5	6	7	8
0	-0.037	-0.061	-0.062	+0.024	+0.034	+0.037	+0.036	+0.029
15	-0.037	-0.059	-0.057	+0.020	+0.031	+0.030	+0.030	+0.025
30	-0.037	-0.056	-0.055	+0.002	+0.009	+0.013	+0.010	+0.008
45	-0.037	-0.055	-0.057	-0.020	-0.018	-0.014	-0.016	-0.010
60	-0.037	-0.051	-0.056	-0.038	-0.038	-0.035	-0.037	-0.029
75	-0.037	-0.045	-0.051	-0.037	-0.035	-0.033	-0.033	-0.035
90	-0.037	-0.037	-0.040	-0.029	-0.027	-0.027	-0.025	-0.030
105	-0.037	-0.033	-0.029	-0.029	-0.028	-0.027	-0.028	-0.029
120	-0.037	-0.030	-0.027	-0.029	-0.029	-0.030	-0.031	-0.023
135	-0.037	-0.025	-0.023	-0.028	-0.026	-0.026	-0.026	-0.019
150	-0.037	-0.024	-0.020	-0.025	-0.027	-0.027	-0.027	-0.023
165	-0.037	-0.023	-0.020	-0.026	-0.027	-0.029	-0.027	-0.023
180	-0.037	-0.020	-0.019	-0.025	-0.027	-0.026	-0.025	-0.021

FRUSTUM 3

Pressure Tap Number

θ	1	2	3	4	5	6	7	8
0	-0.043	-0.056	-0.056	+0.025	+0.032	+0.035	+0.035	+0.027
15	-0.043	-0.053	-0.052	+0.021	+0.028	+0.030	+0.029	+0.024
30	-0.043	-0.054	-0.055	+0.006	+0.013	+0.015	+0.013	+0.010
45	-0.043	-0.053	-0.053	-0.018	-0.014	-0.013	-0.013	-0.012
60	-0.043	-0.051	-0.055	-0.034	-0.031	-0.030	-0.031	-0.029
75	-0.043	-0.049	-0.053	-0.037	-0.035	-0.034	-0.032	-0.036
90	-0.043	-0.045	-0.045	-0.030	-0.029	-0.028	-0.027	-0.029
105	-0.043	-0.041	-0.039	-0.029	-0.029	-0.029	-0.027	-0.030
120	-0.043	-0.039	-0.031	-0.029	-0.028	-0.028	-0.028	-0.029
135	-0.043	-0.034	-0.027	-0.028	-0.028	-0.029	-0.029	-0.027
150	-0.043	-0.031	-0.026	-0.028	-0.028	-0.029	-0.030	-0.026
165	-0.043	-0.030	-0.025	-0.029	-0.029	-0.030	-0.029	-0.025
180	-0.043	-0.031	-0.024	-0.028	-0.028	-0.029	-0.027	-0.022

FRUSTUM 2

Pressure Tap Number

θ	1	2	3	4	5	6	7
0	-0.045	-0.048	+0.023	+0.031	+0.031	+0.031	+0.029
15	-0.045	-0.049	+0.019	+0.026	+0.027	+0.028	+0.025
30	-0.045	-0.049	+0.002	+0.008	+0.008	+0.010	+0.014
45	-0.045	-0.046	-0.021	-0.017	-0.015	-0.011	-0.004
60	-0.045	-0.046	-0.043	-0.039	-0.036	-0.034	-0.022
75	-0.045	-0.046	-0.036	-0.034	-0.036	-0.036	-0.034
90	-0.045	-0.047	-0.031	-0.029	-0.028	-0.027	-0.030
105	-0.045	-0.045	-0.029	-0.029	-0.028	-0.029	-0.030
120	-0.045	-0.041	-0.030	-0.029	-0.029	-0.029	-0.030
135	-0.045	-0.037	-0.029	-0.029	-0.029	-0.029	-0.029
150	-0.045	-0.034	-0.030	-0.029	-0.029	-0.029	-0.026
165	-0.045	-0.034	-0.029	-0.029	-0.029	-0.029	-0.026
180	-0.045	-0.033	-0.028	-0.028	-0.029	-0.029	-0.026

FRUSTUM 1

Pressure Tap Number

θ	1	2	3	4	5	6
0	-0.029	+0.031	+0.036	+0.037	+0.037	+0.037
15	-0.030	+0.030	+0.029	+0.034	+0.037	+0.036
30	-0.030	+0.017	+0.015	+0.015	+0.017	+0.019
45	-0.030	-0.003	-0.004	-0.002	-0.003	-0.000
60	-0.030	-0.024	-0.023	-0.018	-0.016	-0.013
75	-0.030	-0.028	-0.031	-0.031	-0.026	-0.020
90	-0.030	-0.024	-0.023	-0.023	-0.023	-0.024
105	-0.030	-0.023	-0.023	-0.023	-0.023	-0.023
120	-0.030	-0.022	-0.023	-0.023	-0.023	-0.025
135	-0.030	-0.022	-0.023	-0.023	-0.023	-0.025
150	-0.030	-0.021	-0.023	-0.023	-0.023	-0.025
165	-0.030	-0.022	-0.023	-0.024	-0.023	-0.022
180	-0.030	-0.022	-0.023	-0.023	-0.023	-0.021

STREAMWISE COMPONENT OF FORCE, (lbf/Δh) (x 10^{-4}) AT EACH SIDE PRESSURE TAP FOR EACH θ , GIVEN BY $cp(r,\theta,\phi)\cos\theta\cos\phi$. SINCE $\cos\phi$ IS A CONSTANT FOR A PARTICULAR MODEL IT IS NOT INCLUDED UNTIL THE ALGEBRAIC SUM OF THE FORCES IS TAKEN.

SMOOTH CYLINDER

θ	5	6	7	8	9
0	+5.2	+6.1	+6.2	+5.9	+4.4
15	+4.6	+5.4	+5.0	+4.7	+3.7
30	+2.0	+2.4	+2.5	+2.2	+1.5
45	-0.5	-0.5	-0.4	-0.5	-0.5
60	-1.7	-1.8	-1.7	-1.7	-1.4
75	-1.1	-1.1	-1.0	-1.0	-1.0
90	0	0	0	0	0
105	+0.8	+0.8	+0.8	+0.7	+0.7
120	+1.4	+1.4	+1.4	+1.4	+1.4
135	+1.9	+1.9	+2.1	+2.0	+1.8
150	+2.4	+2.4	+2.6	+2.6	+2.2
165	+2.6	+2.9	+2.9	+2.8	+2.2
180	+2.9	+3.0	+3.0	+2.9	+2.1

ROUGH CYLINDER

θ	5	6	7	8	9
0	+5.0	+5.1	+6.1	+5.3	+4.3
15	+4.1	+4.7	+4.9	+4.4	+3.5
30	+1.6	+1.6	+1.9	+1.7	+1.2
45	-0.9	-1.1	-1.1	-0.9	-0.8
60	-1.7	-2.1	-1.9	-1.8	-1.4
75	-1.4	-1.4	-1.4	-1.2	-1.3
90	0	0	0	0	0
105	+1.0	+0.9	+0.9	+0.9	+1.0
120	+1.4	+1.8	+1.7	+1.8	+1.9
135	+2.5	+2.5	+2.5	+2.6	+2.7
150	+3.1	+3.2	+3.3	+3.3	+2.8
165	+3.5	+3.4	+3.5	+3.4	+3.1
180	+3.4	+3.5	+3.7	+3.2	+2.8

FRUSTUM 4

θ	4	5	6	7	8
0	+3.4	+3.8	+4.4	+4.5	+4.1
15	+2.0	+3.3	+3.4	+3.7	+3.4
30	+0.2	+0.9	+1.3	+1.1	+1.0
45	-1.5	-1.4	-1.2	-1.4	-1.0
60	-2.0	-2.1	-2.1	-2.3	-2.1
75	-1.0	-1.0	-1.0	-1.1	-1.3
90	0	0	0	0	0
105	+0.8	+0.8	+0.8	+0.9	+1.1
120	+1.5	+1.6	+1.8	+2.0	+1.6
135	+2.1	+2.1	+2.2	+2.3	+1.9
150	+2.3	+2.6	+2.8	+2.9	+2.8
165	+2.6	+2.9	+3.3	+3.3	+3.2
180	+2.6	+3.0	+3.1	+3.1	+3.0

FRUSTUM 3

θ	4	5	6	7	8
0	+2.1	+2.9	+3.5	+3.9	+3.7
15	+1.7	+2.5	+2.9	+3.2	+3.2
30	+0.4	+1.0	+1.3	+1.3	+1.2
45	-1.0	-0.9	-0.9	-1.9	-1.2
60	-1.4	-1.4	-1.5	-1.7	-2.0
75	-0.8	-0.8	-0.9	-0.9	-1.3
90	0	0	0	0	0
105	+0.6	+0.7	+0.8	+0.8	+1.1
120	+1.2	+1.3	+1.4	+1.6	+2.0
135	+1.6	+1.8	+2.0	+2.3	+2.6
150	+2.0	+2.2	+2.5	+2.9	+3.1
165	+2.3	+2.6	+2.9	+3.2	+3.3
180	+1.8	+2.6	+2.9	+3.0	+3.0

FRUSTUM 2

θ	3	4	5	6	7
0	+1.3	+2.2	+2.6	+3.1	+3.8
15	+1.1	+1.8	+2.2	+2.7	+3.2
30	+0.1	+0.5	+0.6	+0.9	+1.6
45	-0.9	-0.8	-0.9	-0.8	-0.4
60	-1.3	-1.4	-1.5	-1.7	-1.4
75	-0.5	-0.6	-0.8	-0.9	-0.4
90	0	0	0	0	0
105	+0.4	+0.5	+0.6	+0.7	+1.0
120	+0.9	+1.0	+1.2	+1.4	+2.0
135	+1.2	+1.4	+1.7	+2.0	+2.7
150	+1.5	+1.8	+2.1	+2.6	+3.3
165	+1.6	+2.0	+2.3	+2.8	+3.3
180	+1.6	+2.0	+2.4	+2.9	+3.4

FRUSTUM 1

θ	2	3	4	5	6
0	+1.1	+1.8	+2.4	+3.1	+4.5
15	+1.0	+1.4	+2.1	+3.0	+4.3
30	+0.5	+0.6	+0.8	+1.2	+2.0
45	-0.1	-0.1	-0.1	-0.2	0
60	-0.4	-0.6	-0.6	-0.7	-0.8
75	-0.3	-0.4	-0.5	-0.6	-0.6
90	0	0	0	0	0
150	+0.2	+0.3	+0.4	+0.5	+0.7
120	+0.4	+0.6	+0.7	+1.0	+1.5
135	+0.5	+0.8	+1.0	+1.4	+2.2
150	+0.6	+1.0	+1.3	+1.7	+2.7
165	+0.7	+1.1	+1.5	+1.9	+2.6
180	+0.8	+1.1	+1.5	+1.9	+2.6

ALGEBRAIC SUM OF STREAMWISE COMPONENT OF FORCE PER Δh AT EACH SIDE PRESSURE TAP ($x\ 10^{-4}$ lbf/Δh).

SMOOTH CYLINDER ($x\ 10^{-4}$)

5	6	7	8	9
20.5	22.9	23.4	22.0	17.1

ROUGH CYLINDER ($x\ 10^{-4}$)

5	6	7	8	9
21.6	22.7	24.0	22.7	19.8

FRUSTUM 4 ($x\ 10^{-4}$)

4	5	6	7	8
12.8	16.3	18.6	18.8	17.5

FRUSTUM 3 ($x\ 10^{-4}$)

4	5	6	7	8
10.2	14.3	16.7	18.4	18.5

FRUSTUM 2 ($x\ 10^{-4}$)

3	4	5	6	7
6.6	9.9	11.9	14.9	21.0

FRUSTUM 1 ($x\ 10^{-4}$)

2	3	4	5	6
4.6	7.0	9.7	13.1	20.0

TOTAL DRAG FORCE (lbf) ON MODELS DETERMINED FROM THE PRESSURE DISTRIBUTION ANALYSIS

SMOOTH CYLINDER	0.0234
ROUGH CYLINDER	0.0250
FRUSTUM 4	0.0192
FRUSTUM 3	0.0189
FRUSTUM 2	0.0175
FRUSTUM 1	0.0159

TOTAL DRAG FORCE (lbf) ON MODELS DETERMINED FROM THE SHEAR PLATE ANALYSIS

ROUGH CYLINDER	0.0275
FRUSTUM 4	0.0212
FRUSTUM 3	0.0192
FRUSTUM 2	0.0165
FRUSTUM 1	0.0142

DRAG COEFFICIENTS

(from shear plate drag force values)

$$U_\infty\Big|_{\text{ref. ht.}} = 4.7 \text{ Meters/sec.}$$

$$C_d = \frac{\text{drag force}}{1/2\ \rho\ U_\infty\Big|^2_{\text{ref. ht.}}\ A_x}$$

CYLINDER	0.527
FRUSTUM 4	0.487
FRUSTUM 3	0.490
FRUSTUM 2	0.473
FRUSTUM 1	0.466

PRESSURE COEFFICIENT DISTRIBUTIONS AROUND THE MODELS AT THE SIDE TOP, SIDE MIDDLE AND SIDE BOTTOM PRESSURE TAPS

$$R = \frac{U_\infty|_{\text{ref. ht.}} D}{\nu} = 3.7 \times 10^4$$

$$C_p = \frac{P_{\text{total}}|_{r,\theta,\phi} - P_{\text{static}}|_{\text{ref. ht.}}}{1/2\ \rho U_\infty|^2_{\text{ref. ht.}}}$$

ROUGH CYLINDER

θ	5	7	9
0	+0.439	+0.532	+0.373
15	+0.373	+0.439	319
30	+0.160	+0.186	+0.120
45	-0.106	-0.133	-0.093
60	293	333	240
75	479	453	426
90	373	373	399
105	346	319	346
120	293	293	333
135	306	306	333
150	306	333	280
165	319	319	280
180	-0.293	-0.319	-0.240

FRUSTUM 4

θ	4	6	8
0	+0.319	+0.492	+0.386
15	+0.266	399	+0.333
30	+0.027	+0.173	+0.106
45	-0.266	-0.186	-0.133
60	506	466	386
75	492	439	466
90	386	359	399
105	386	359	386
120	386	399	306
135	373	346	253
150	333	359	306
165	346	386	306
180	-0.333	-0.346	-0.280

FRUSTUM 3

θ	3	5	7
0	+0.333	+0.466	+0.359
15	+0.280	+0.399	319
30	+0.080	+0.200	+0.133
45	-0.240	-0.173	-0.160
60	453	399	386
75	492	453	479
90	399	373	386
105	386	386	399
120	386	373	386
135	373	373	359
150	373	386	346
165	386	399	333
180	-0.373	-0.386	-0.293

FRUSTUM 2

θ	3	5	7
0	+0.306	+0.413	+0.386
15	+0.253	359	+0.333
30	+0.027	+0.106	+0.186
45	-0.280	-0.200	-0.053
60	572	479	293
75	479	479	453
90	413	373	399
105	386	373	399
120	399	386	399
135	388	386	386
150	399	386	386
165	386	386	346
180	-0.373	-0.386	-0.346

FRUSTUM 1

θ	2	4	6
0	+0.413	+0.492	+0.492
15	399	0.453	+0.479
30	+0.226	+0.200	+0.253
45	-0.040	-0.027	0
60	319	340	-0.173
75	373	413	266
90	319	306	319
105	306	306	306
120	293	306	333
135	293	306	333
150	280	306	333
165	293	319	293
180	-0.293	-0.306	-0.280

TABLE II

TABLE . TURBULENCE INTENSITY PROFILES $\left.\frac{u_{rms}}{U_\infty}\right|_z$

All measurements were taken in a plane parallel to the tunnel floor at Z/D=0.66. The freestream velocity was 4.7 meters/second.

X/D = 0.5

	Y/D			
	0	0.5	1.0	1.5
CYLINDER	0.447	0.667	0.077	0.079
FRUSTUM 4	0.658	0.434	0.075	0.078
FRUSTUM 3	0.704	0.289	0.077	0.082
FRUSTUM 2	0.711	0.143	0.079	0.082
FRUSTUM 1	0.671	0.103	0.077	0.082

X/D = 1.0

	Y/D			
	0	0.5	1.0	1.5
CYLINDER	0.625	0.552	0.083	0.081
FRUSTUM 4	0.657	0.437	0.080	0.081
FRUSTUM 3	0.609	0.329	0.080	0.081
FRUSTUM 2	0.580	0.233	0.077	0.081
FRUSTUM 1	0.590	0.144	0.081	0.082

APPENDIX II

FIGURES

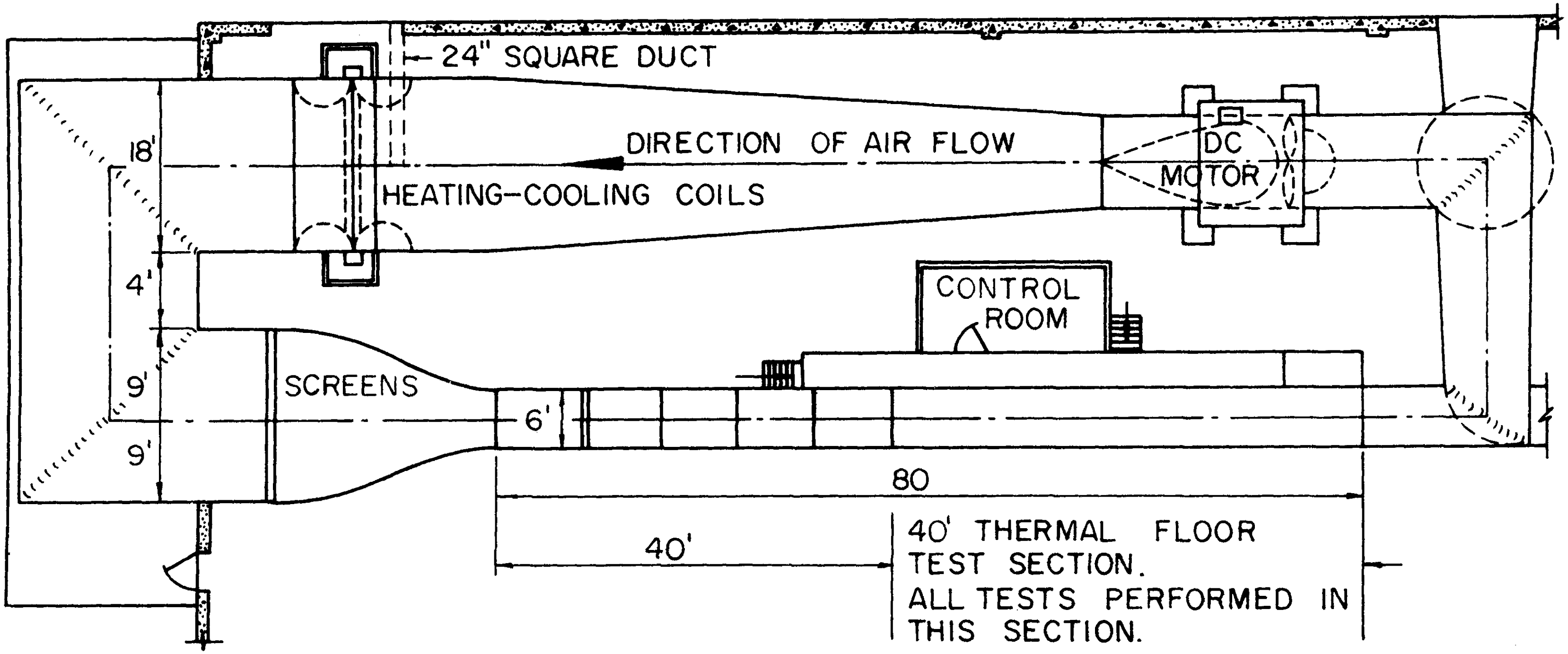

Fig. 1. Wind Tunnel.

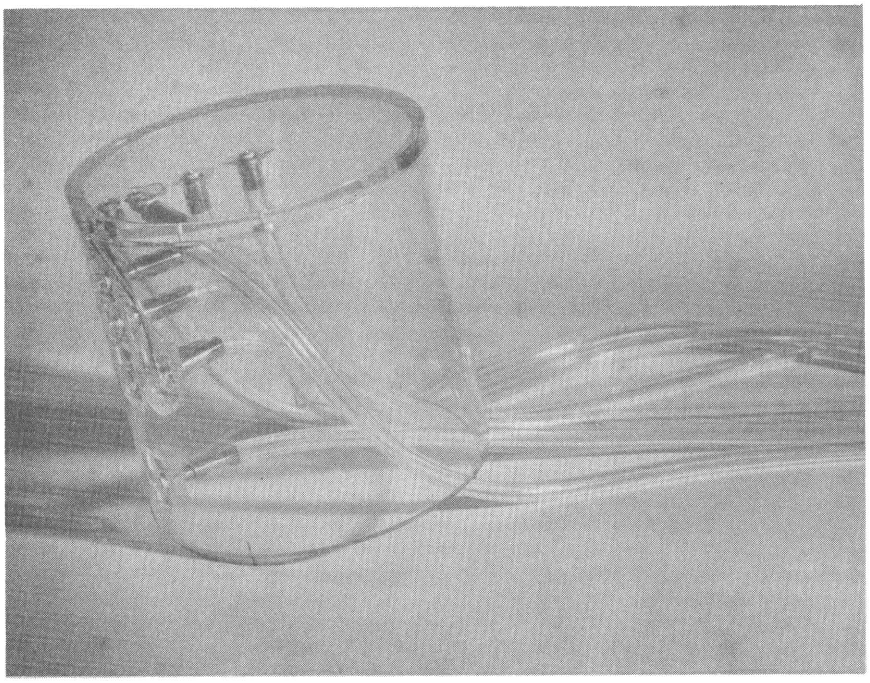

Figure 2. Cylinder with pressure taps.

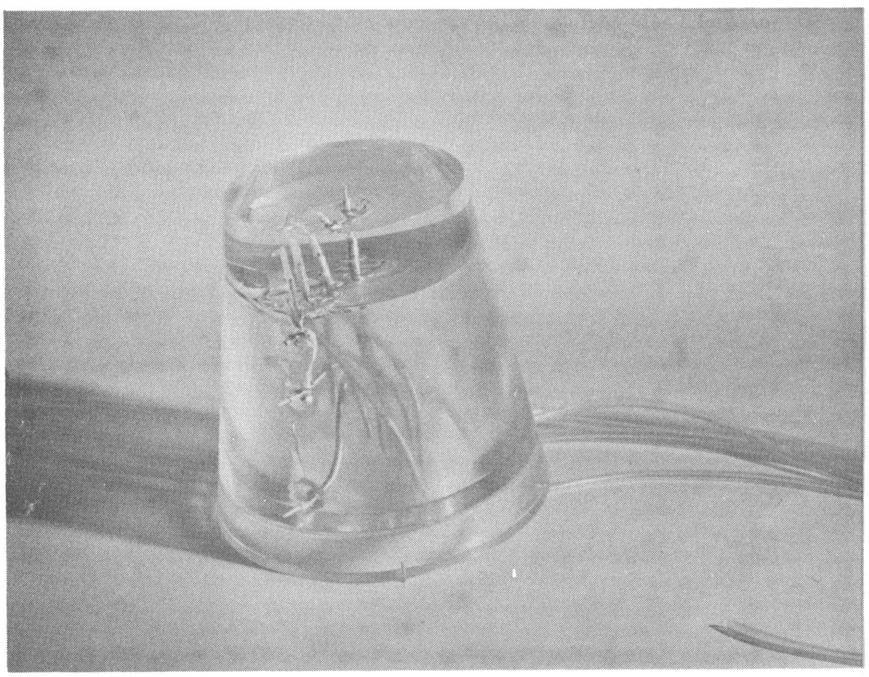

Figure 3. Frustum 4 with pressure taps.

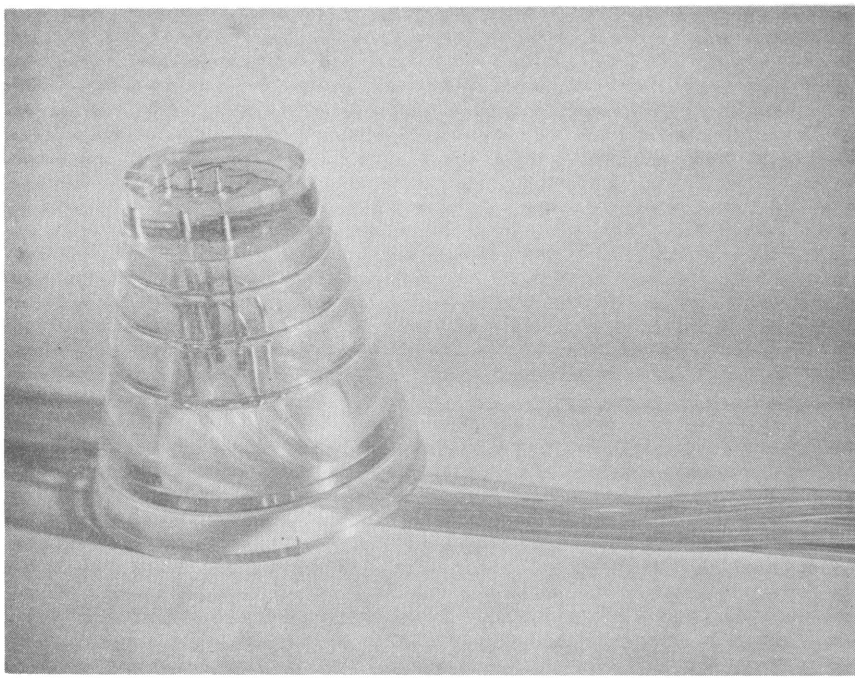

Figure 4. Frustum 3 with pressure taps.

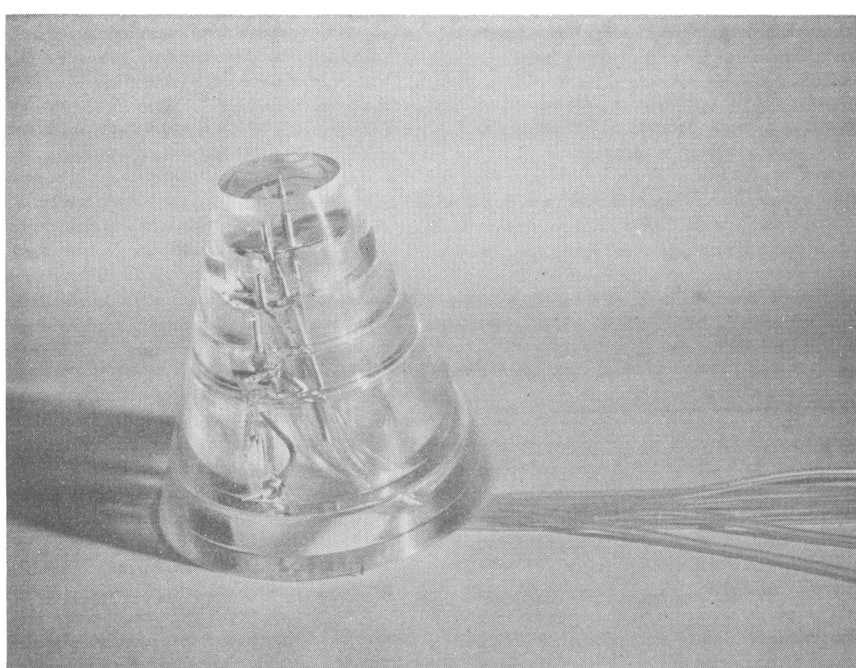

Figure 5. Frustum 2 with pressure taps.

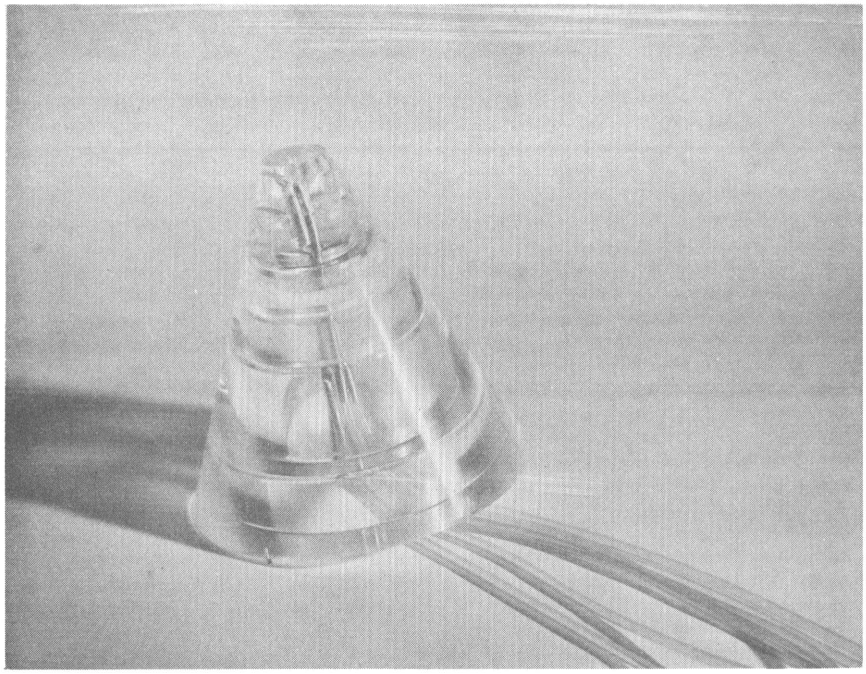

Figure 6. Frustum 1 with pressure taps.

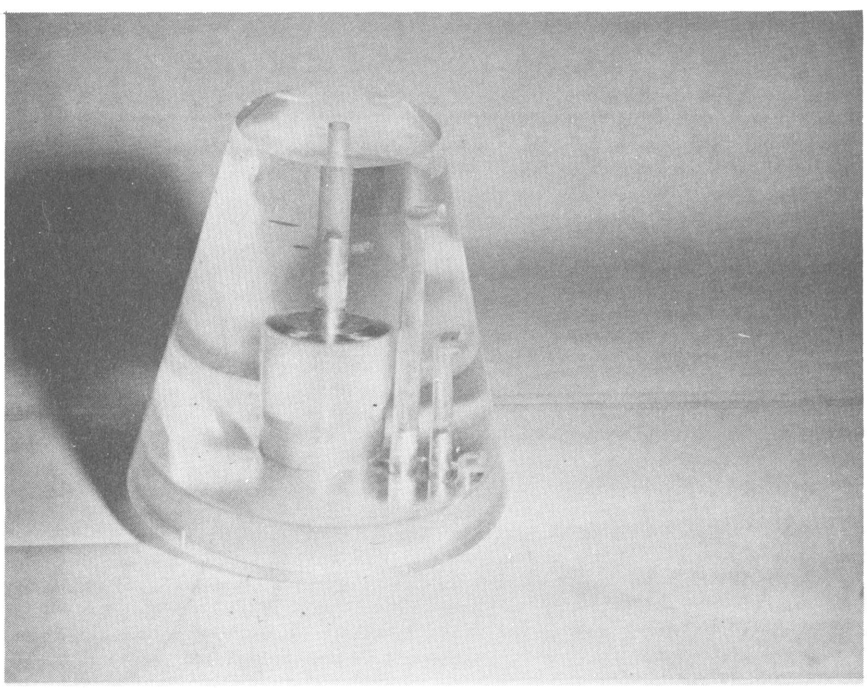

Figure 7. Frustum 3 with gas outlet holes.

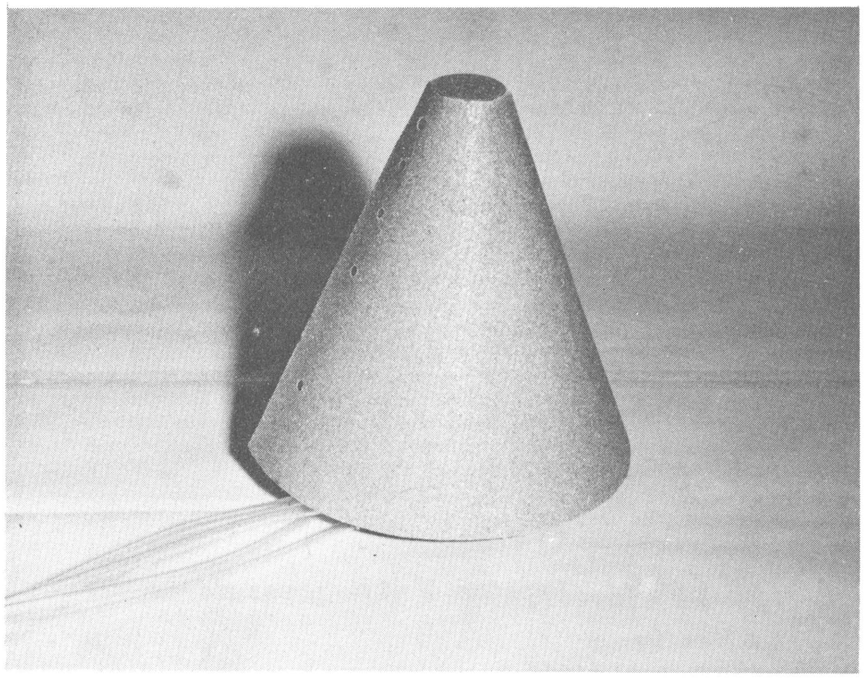

Figure 8. Frustum 1 covered with sandpaper.

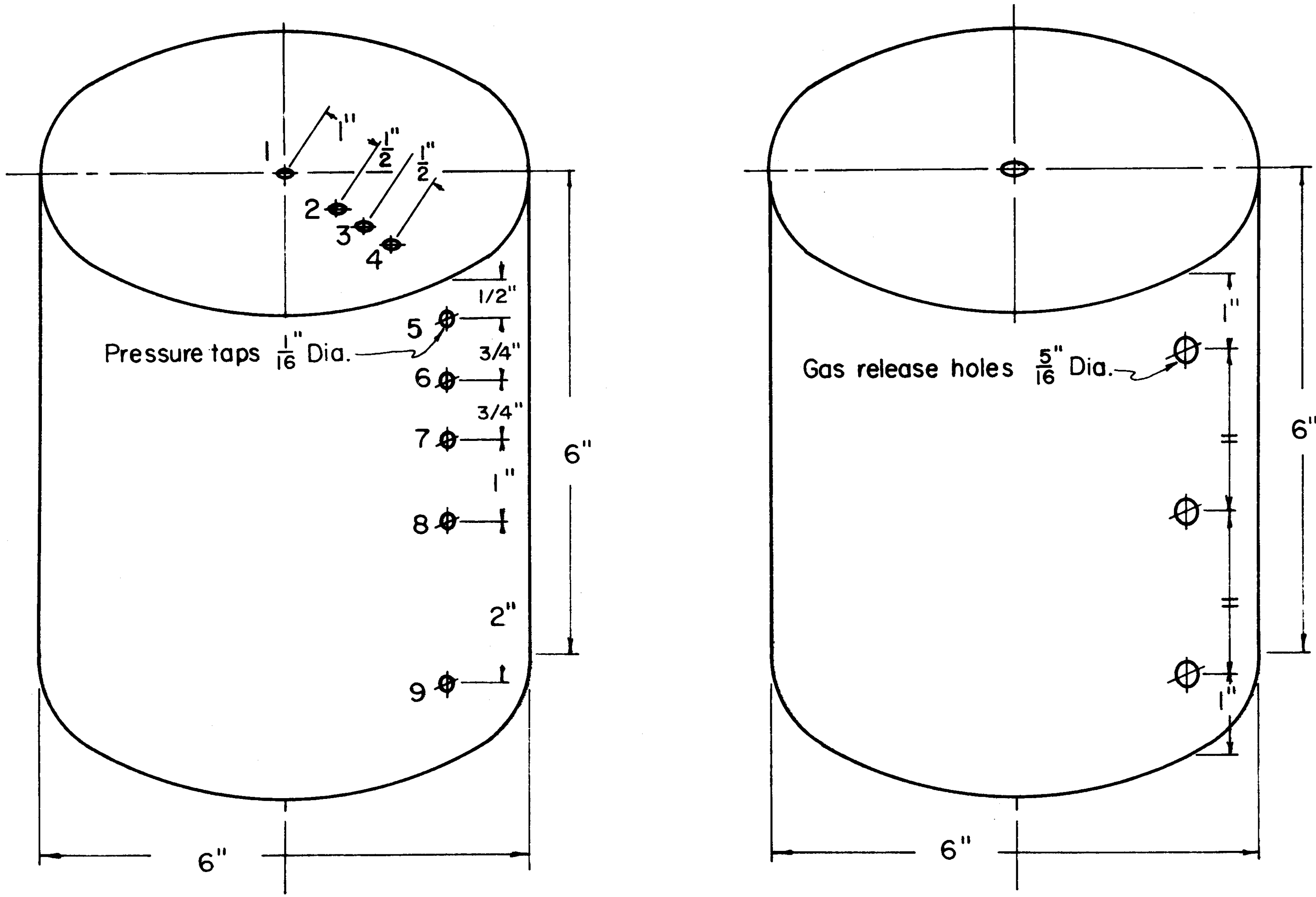

Fig. 9. Cylinder, pressure tap and gas outlet hole detail.

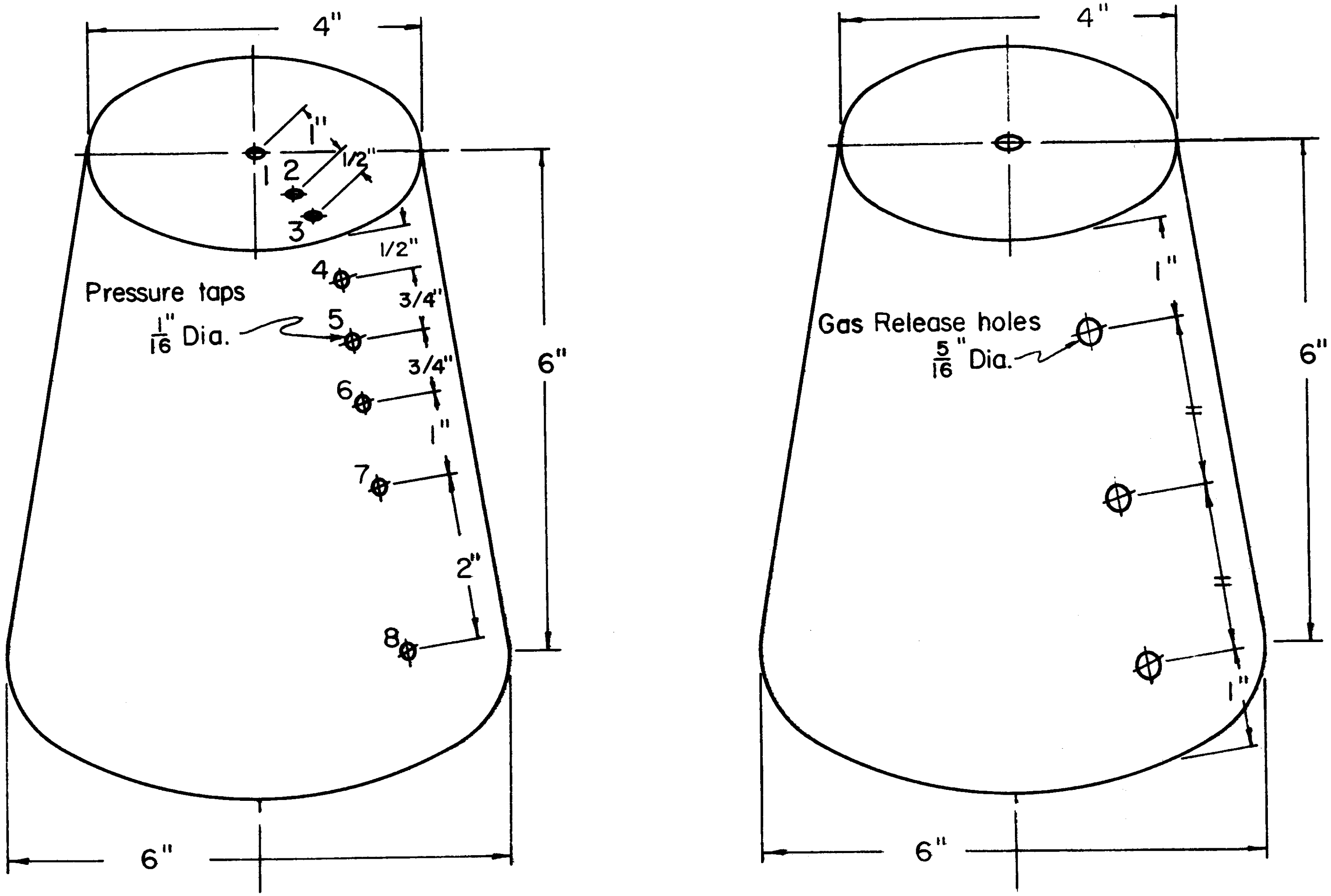

Fig. 10. Frustum 4, pressure tap and gas outlet hole detail.

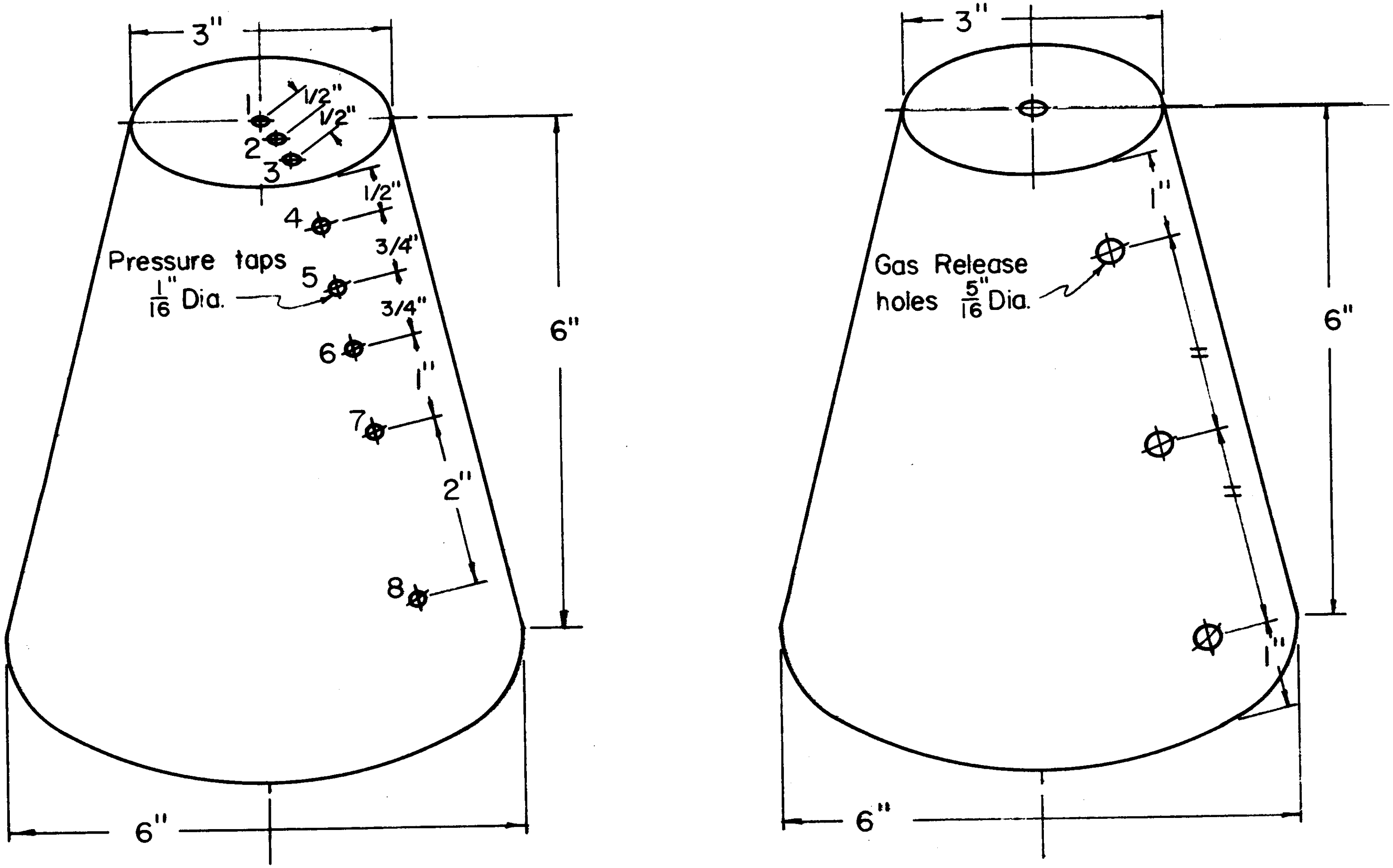

Fig. 11. Frustum 3, pressure tap and gas outlet hole detail.

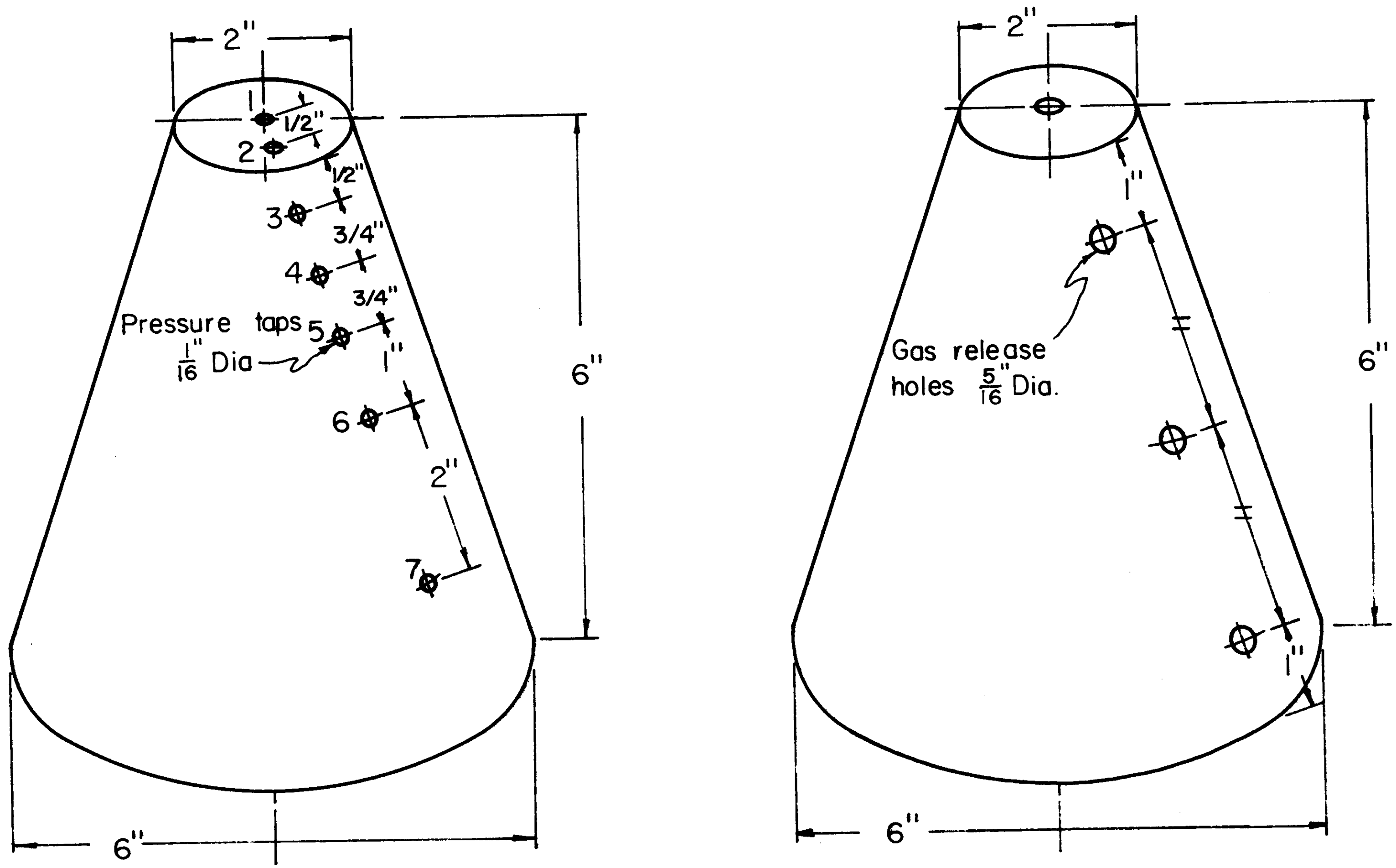

Fig. 12. Frustum 2, pressure tap and gas outlet hole detail.

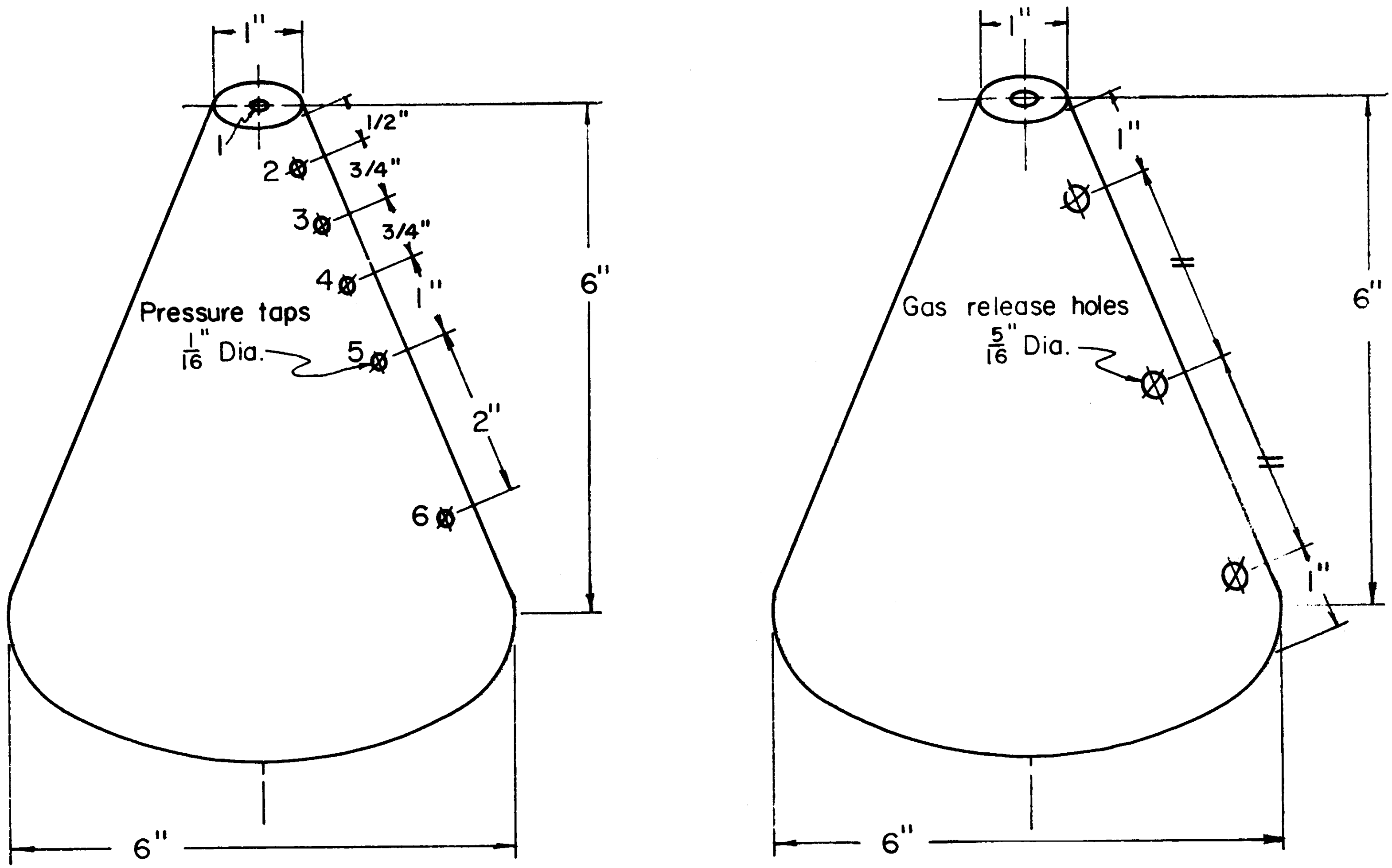

Fig. 13. Frustum 1, pressure tap and gas outlet hole detail.

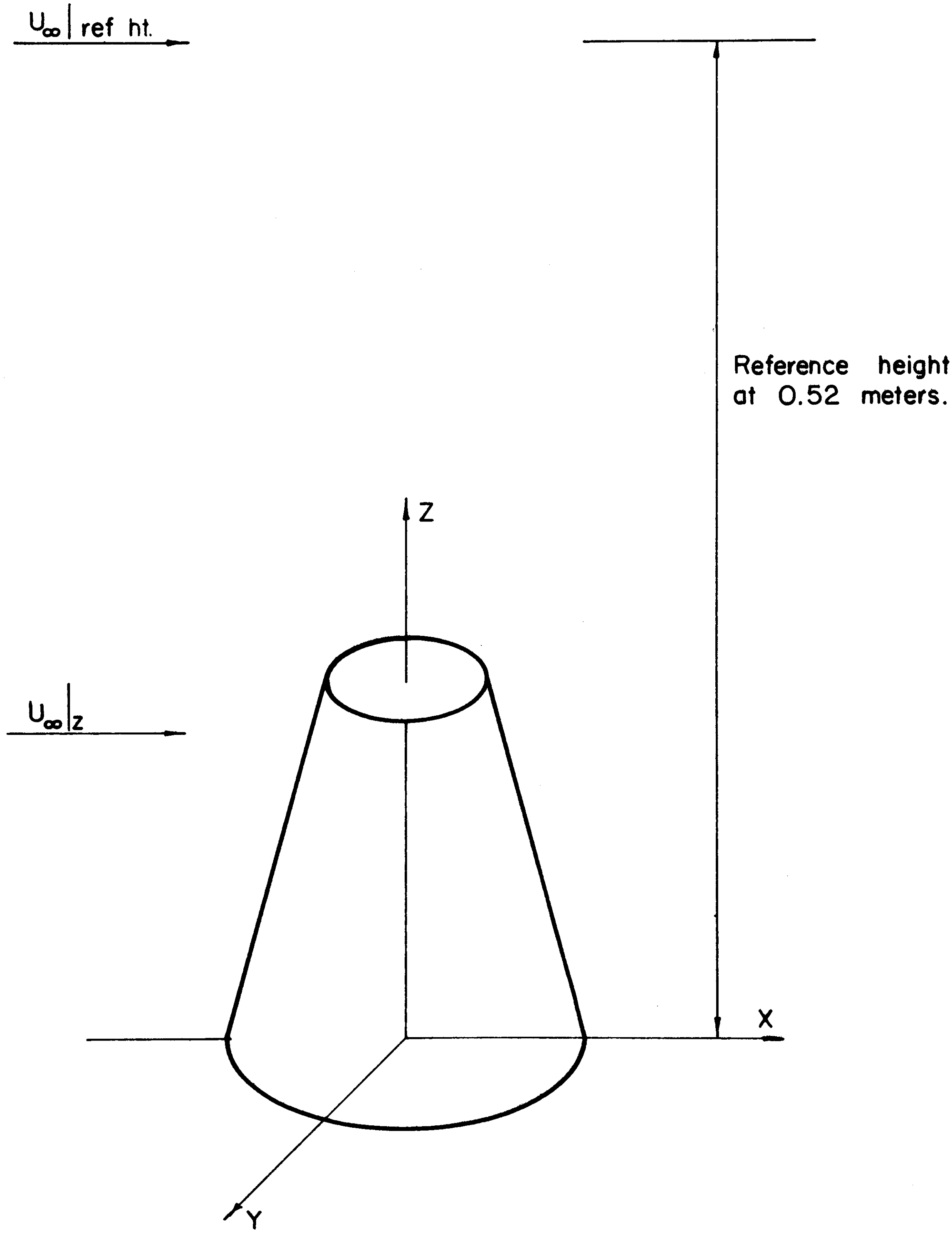

Fig. 14. Co-ordinate system.

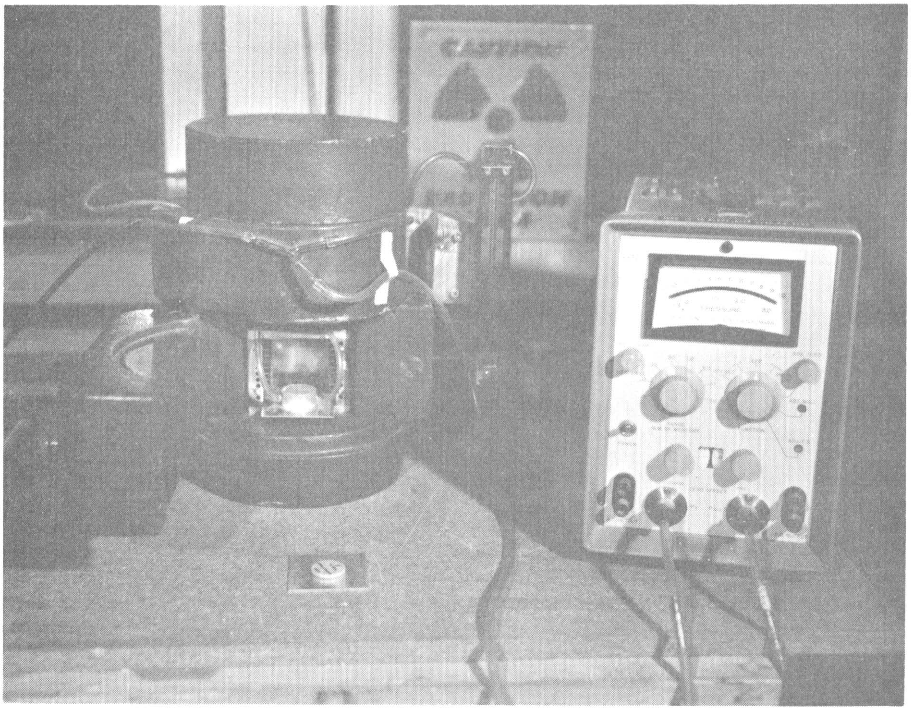

Figure 15. Krypton-85 calibration arrangement.

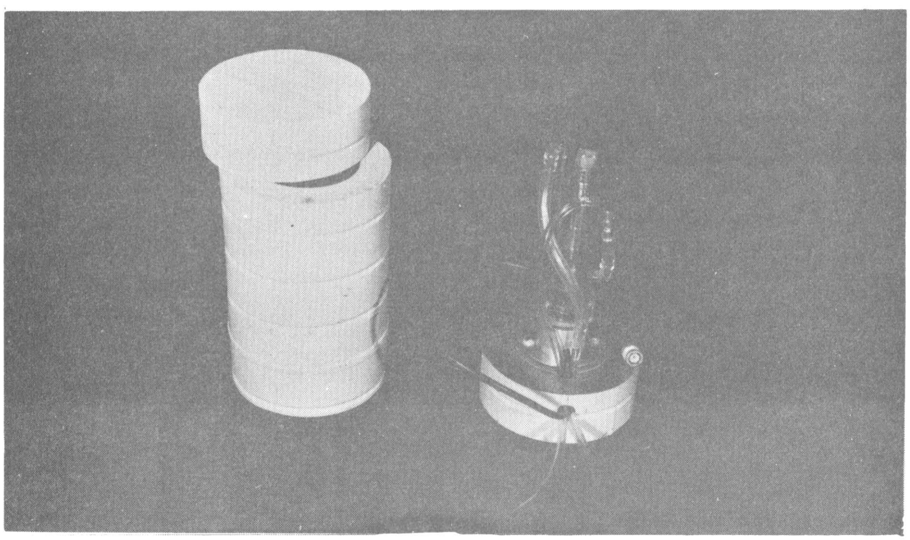

Figure 16. The G.M. tube holder and shield.

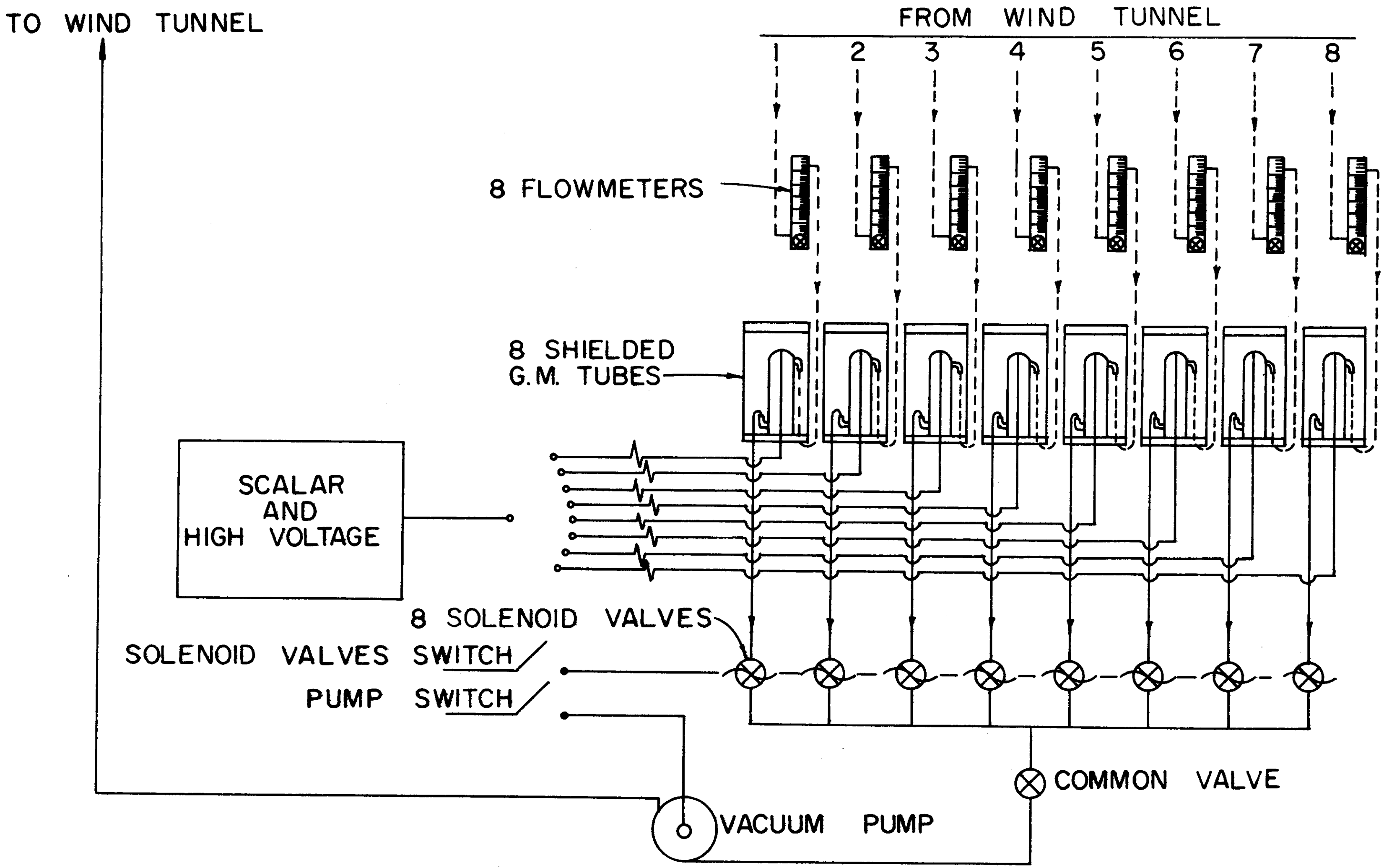

Fig. 17. The sampling and counting system.

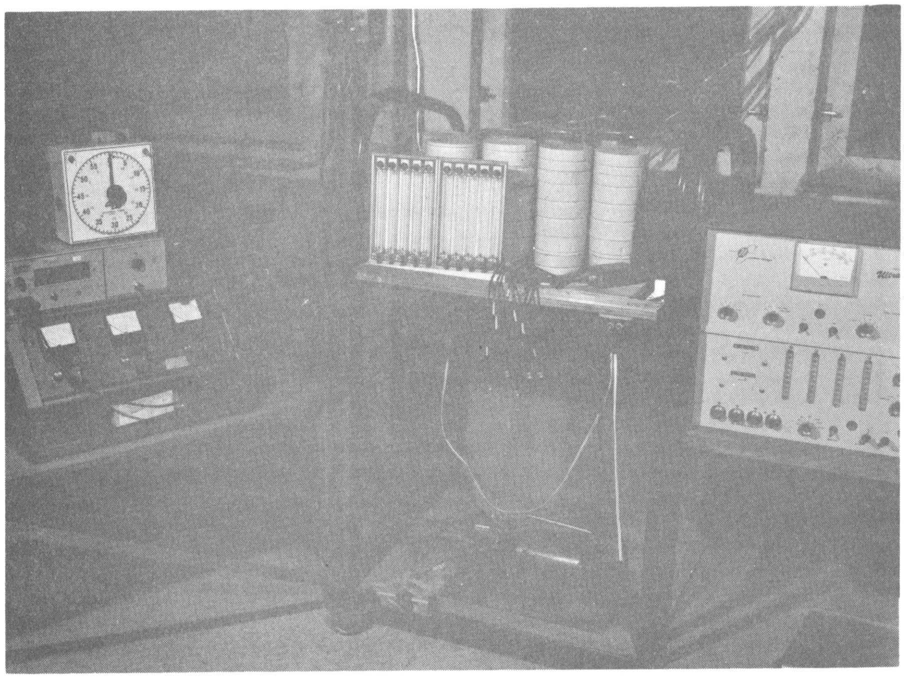

Figure 18. The sampling and counting equipment.

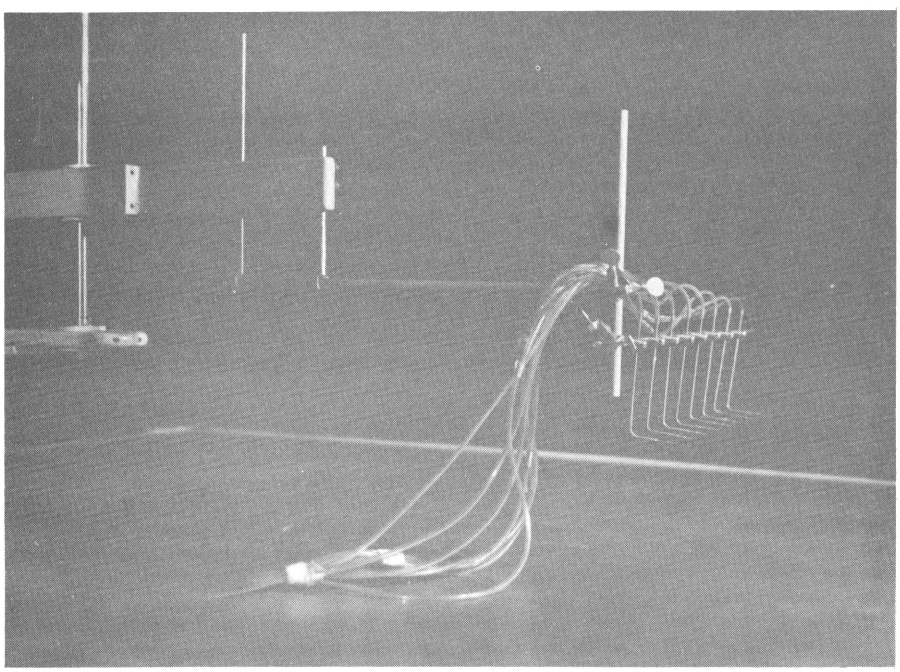

Figure 19. The sampling rake in the horizontal position.

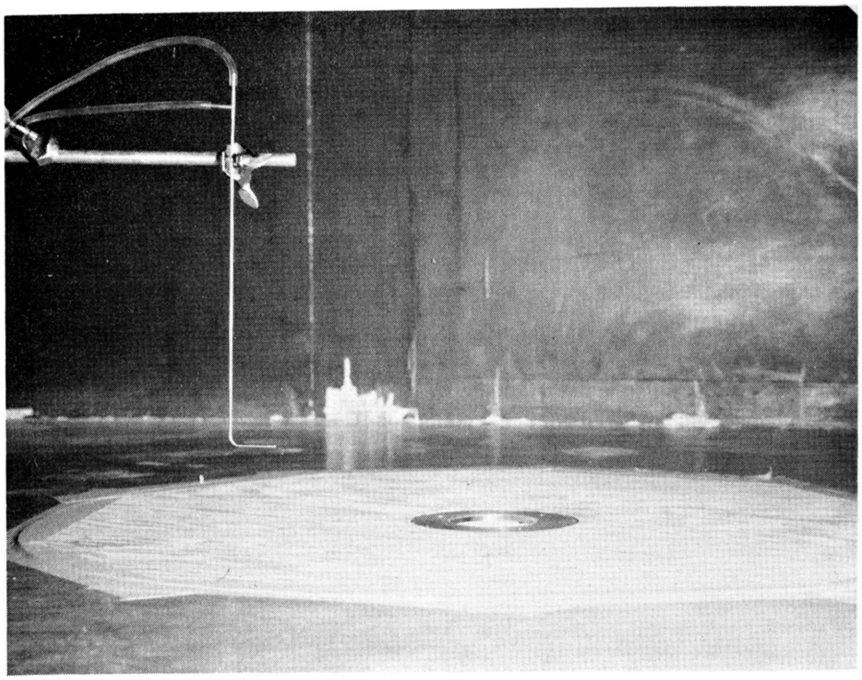

Figure 20. The rotating table mounting plate set in the wind tunnel floor.

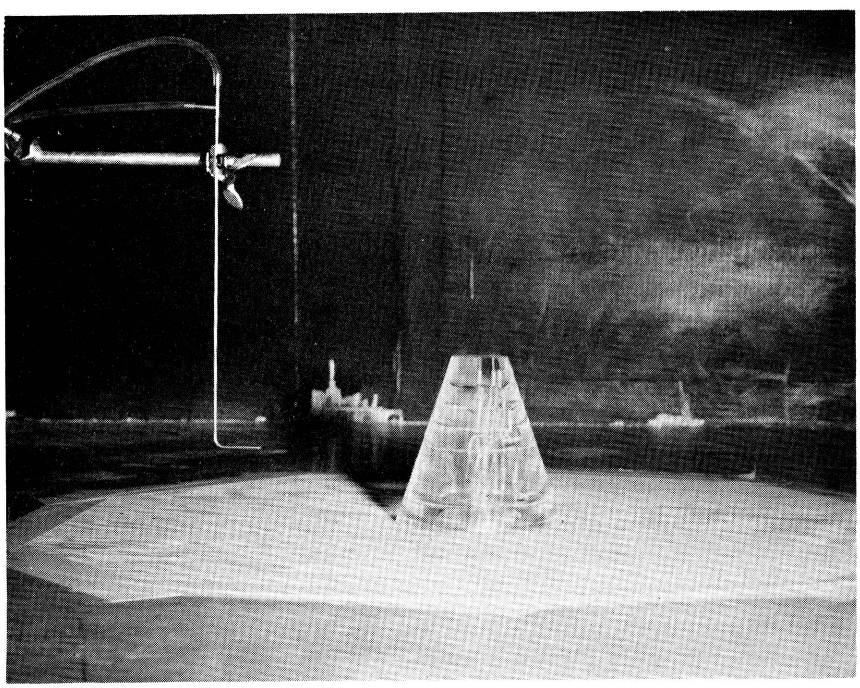

Figure 21. Frustum 2 on the mounting plate.

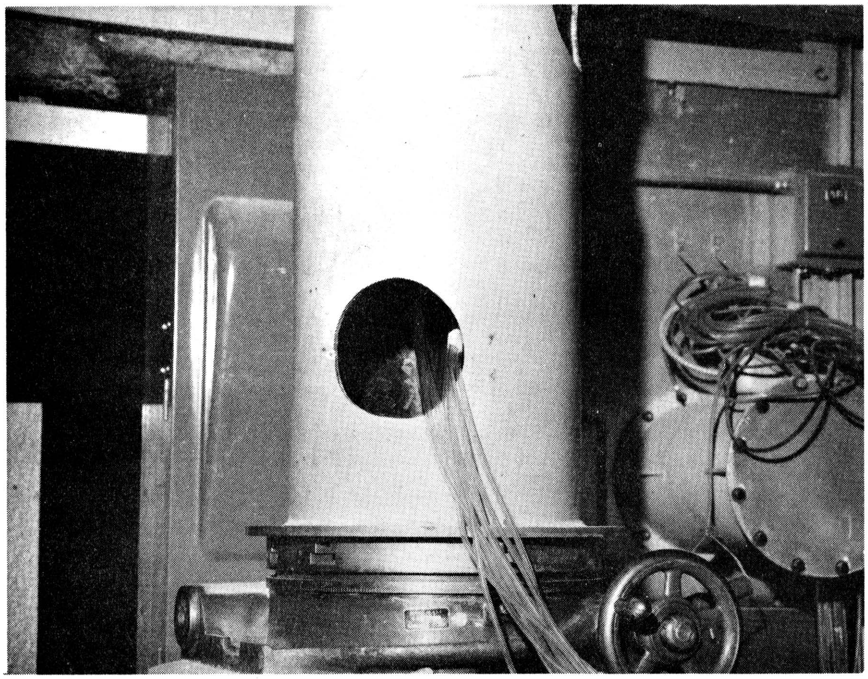

Figure 22. The rotating table drive below the wind tunnel floor.

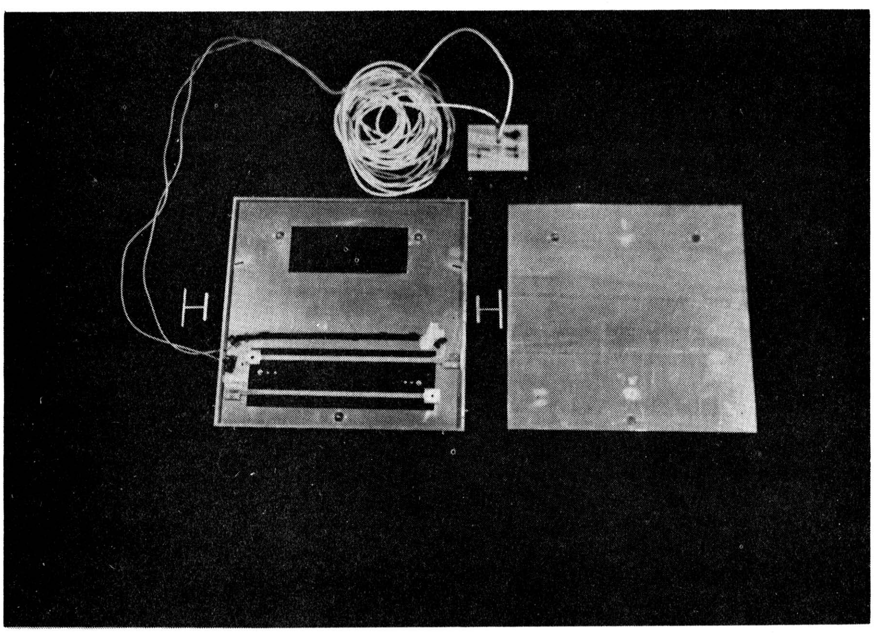

Figure 23. The shear plate components.

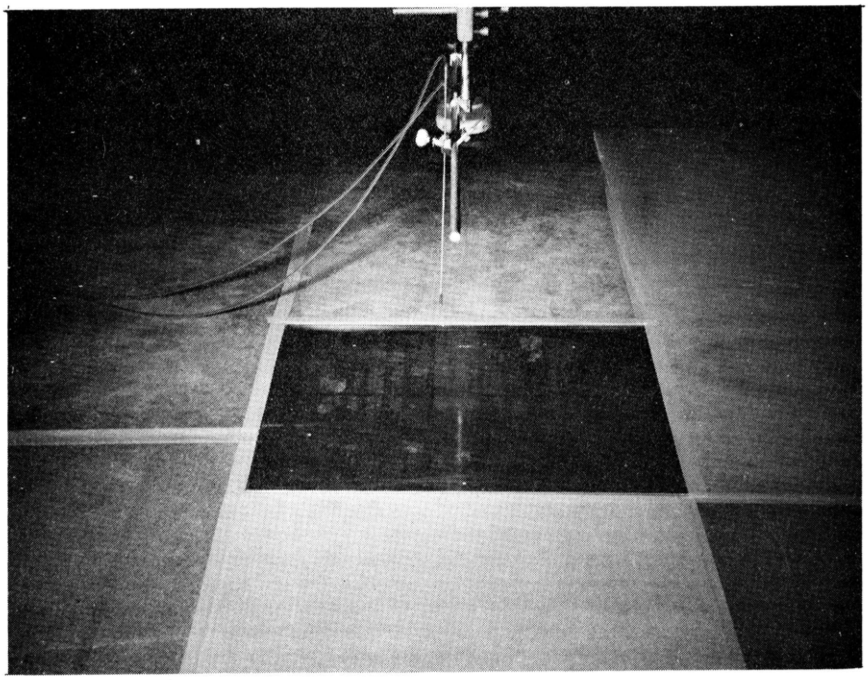

Figure 24. The shear plate with pitot tube mounted on the carriage.

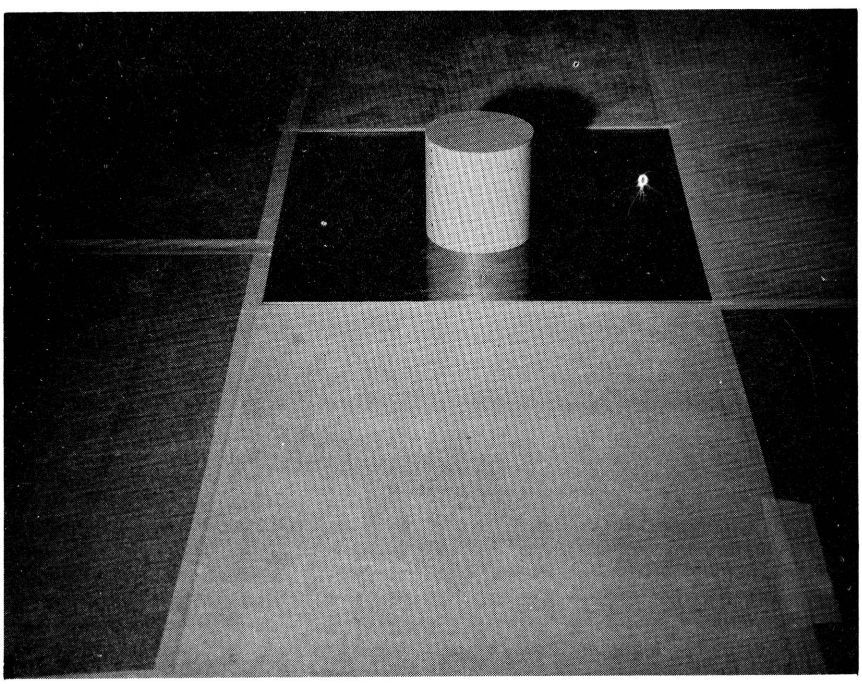

Figure 25. The shear plate with the cylinder in position.

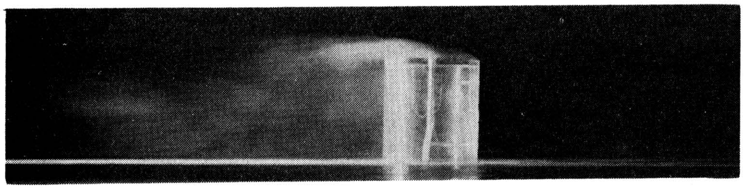

Figure 26. Cylinder, Top.

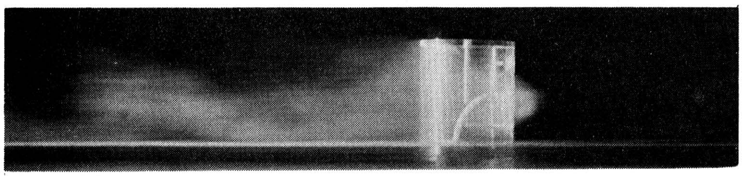

Figure 27. Cylinder, Side Middle, $\theta = 0$.

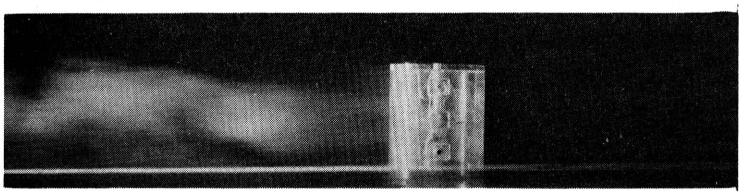

Figure 28. Cylinder, Side Middle, $\theta = 90$.

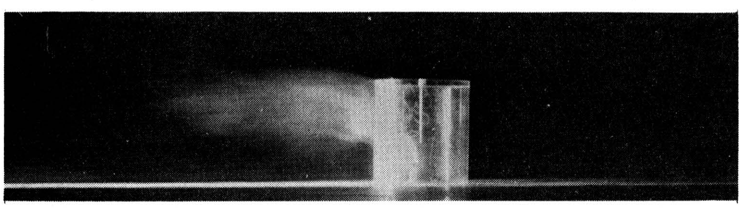

Figure 29. Cylinder, Side Middle, $\theta = 180$.

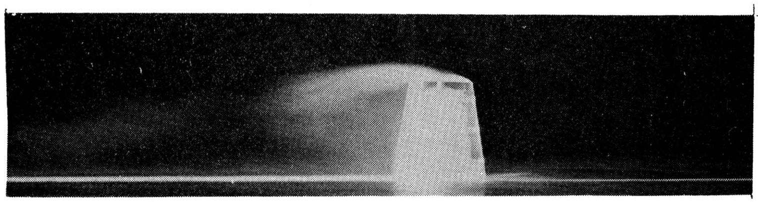

Figure 30. Frustum 4, Top.

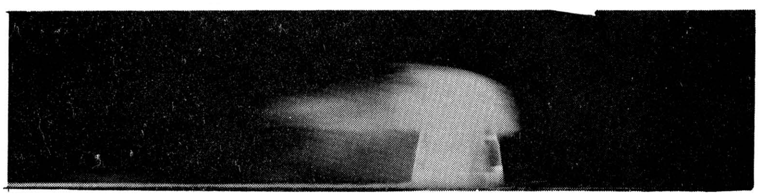

Figure 31. Frustum 4, Side Middle, θ = 0.

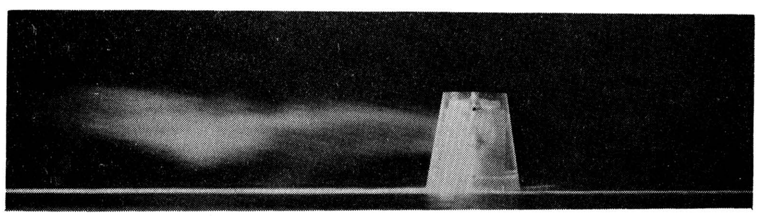

Figure 32. Frustum 4, Side Middle, θ = 90.

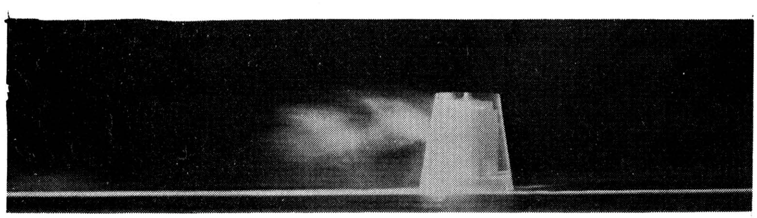

Figure 33. Frustum 4, Side Middle θ = 180.

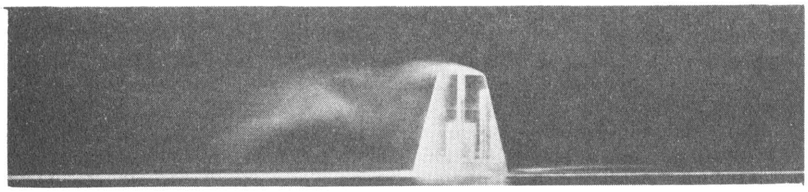

Figure 34. Frustum 3, Top.

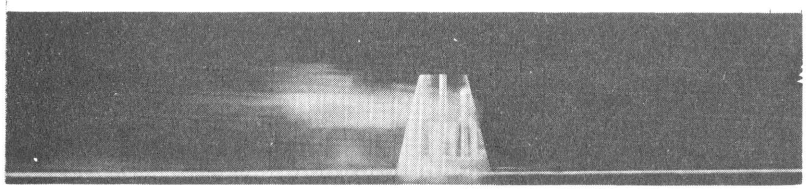

Figure 35. Frustum 3, Side Middle, θ = 0.

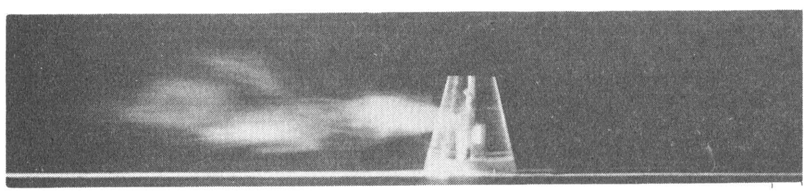

Figure 36. Frustum 3, Side Middle, θ = 90.

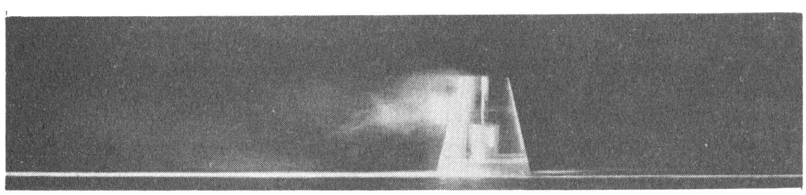

Figure 37. Frustum 3, Side Middle, θ = 180.

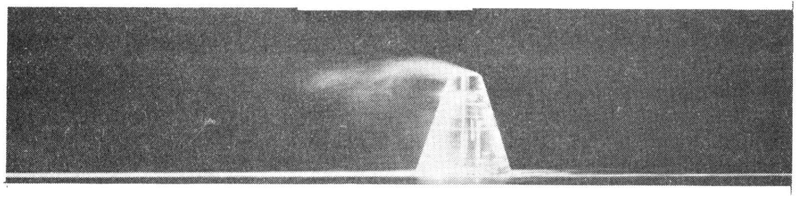

Figure 38. Frustum 2, Top.

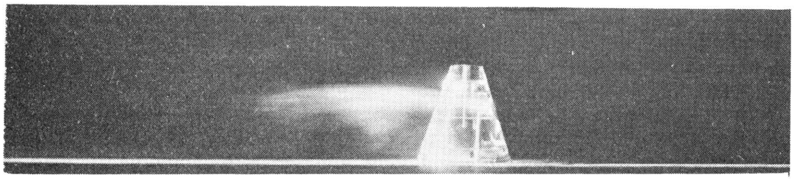

Figure 39. Frustum 2, Side Middle, θ = 0.

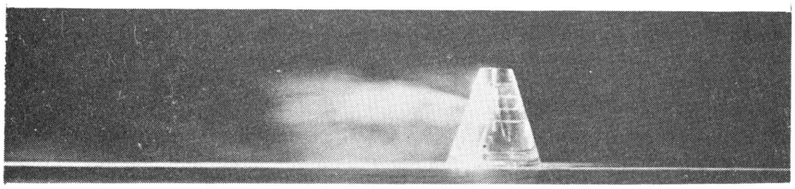

Figure 40. Frustum 2, Side Middle, θ = 90.

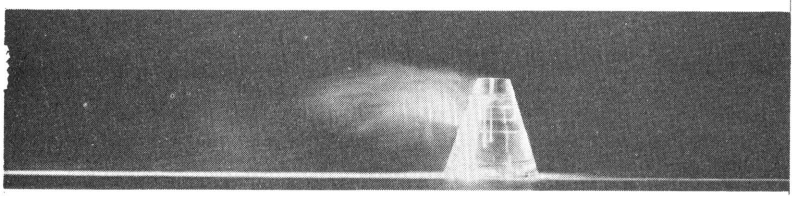

Figure 41. Frustum 2, Side Middle, θ = 180.

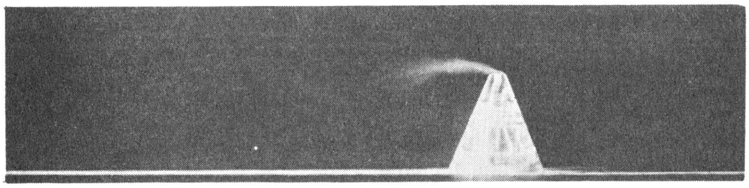

Figure 42. Frustum 1, Top.

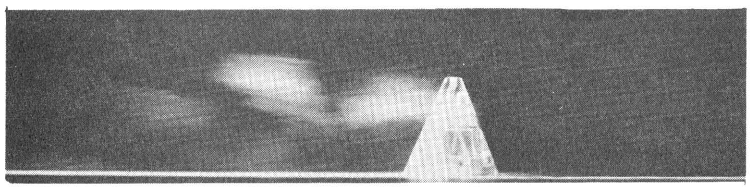

Figure 43. Frustum 1, Side Middle, θ = 0.

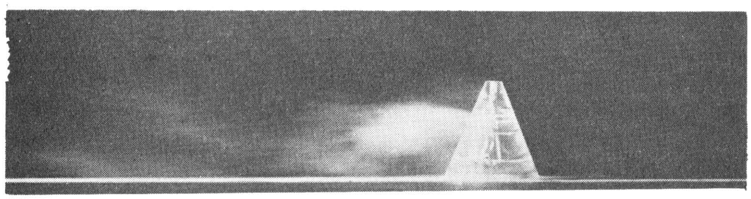

Figure 44. Frustum 1, Side Middle, θ = 90.

Figure 45. Frustum 1, Side Middle, θ = 180.

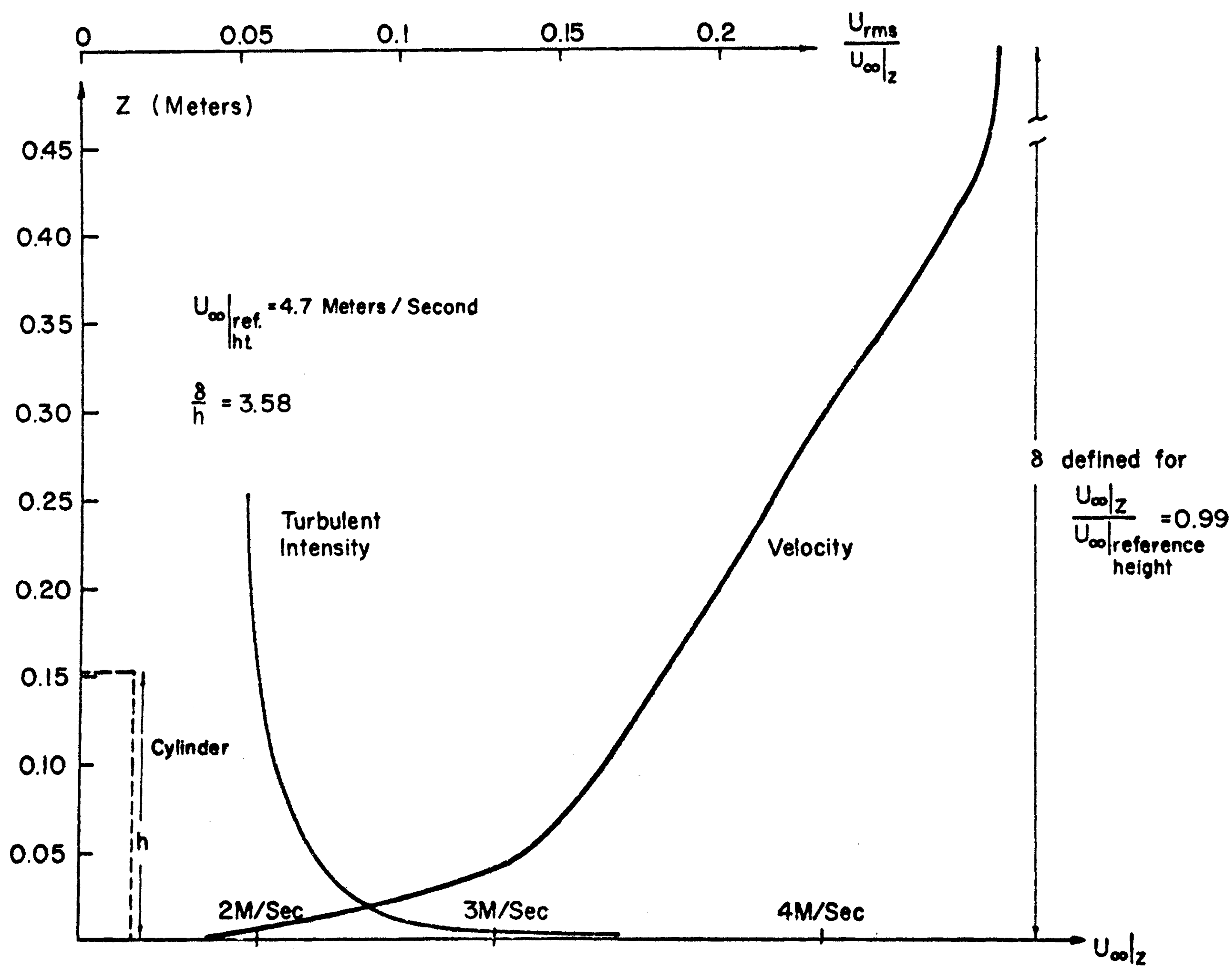

Fig. 46. Velocity profile and turbulent intensity profile at X=Y=0 (no model).

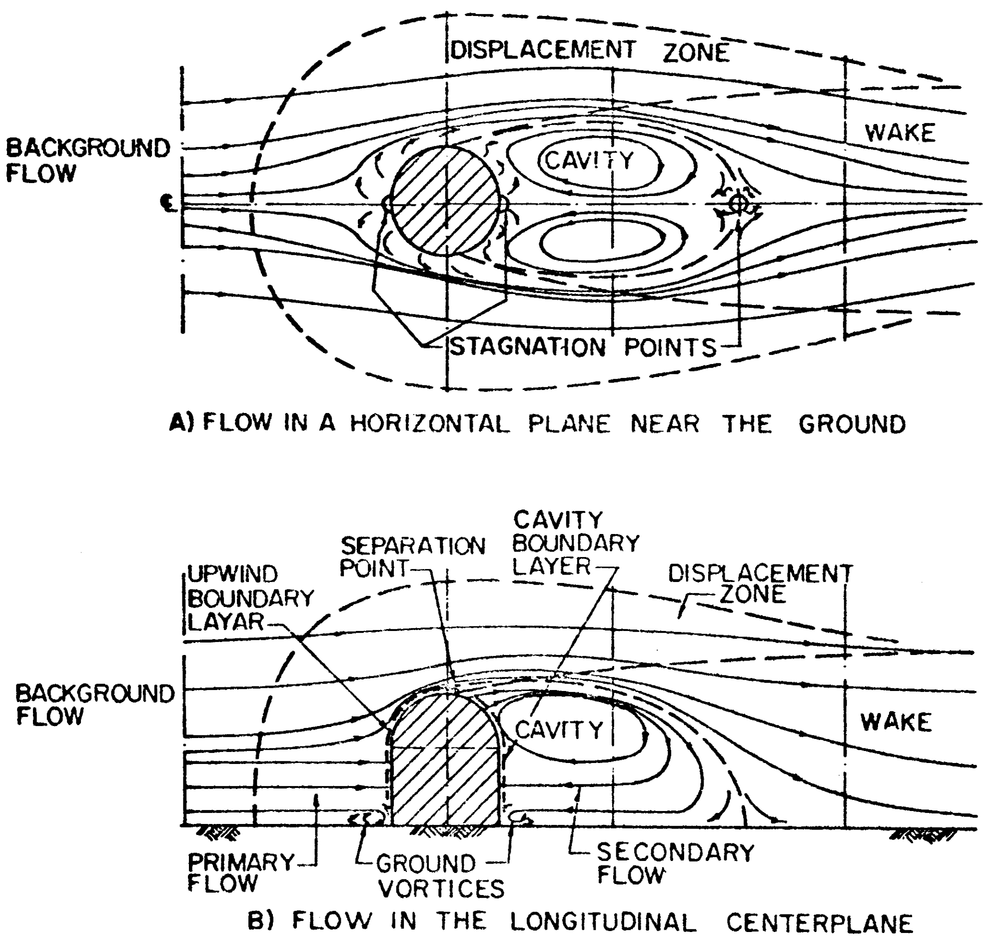

Fig. 47. Flow fields about a reactor shell model (Halitsky).

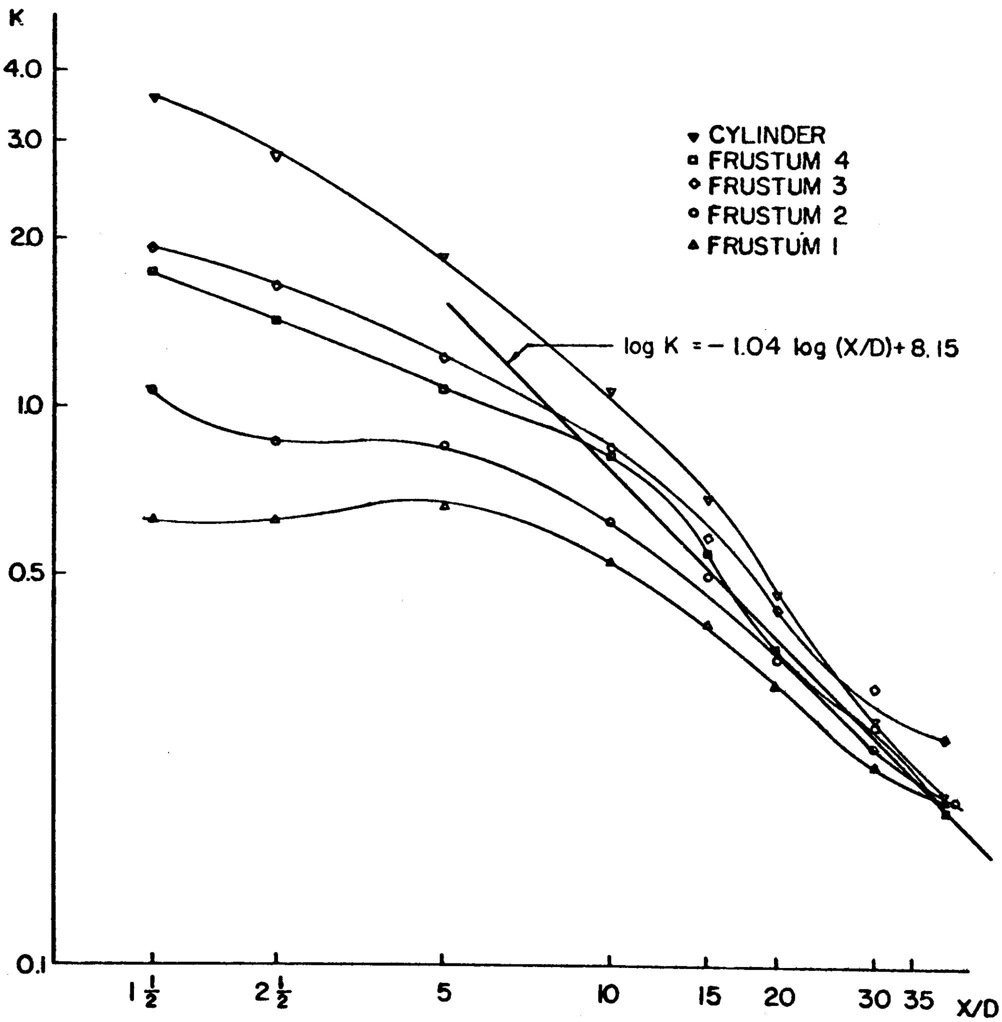

Fig. 48. All models top release.

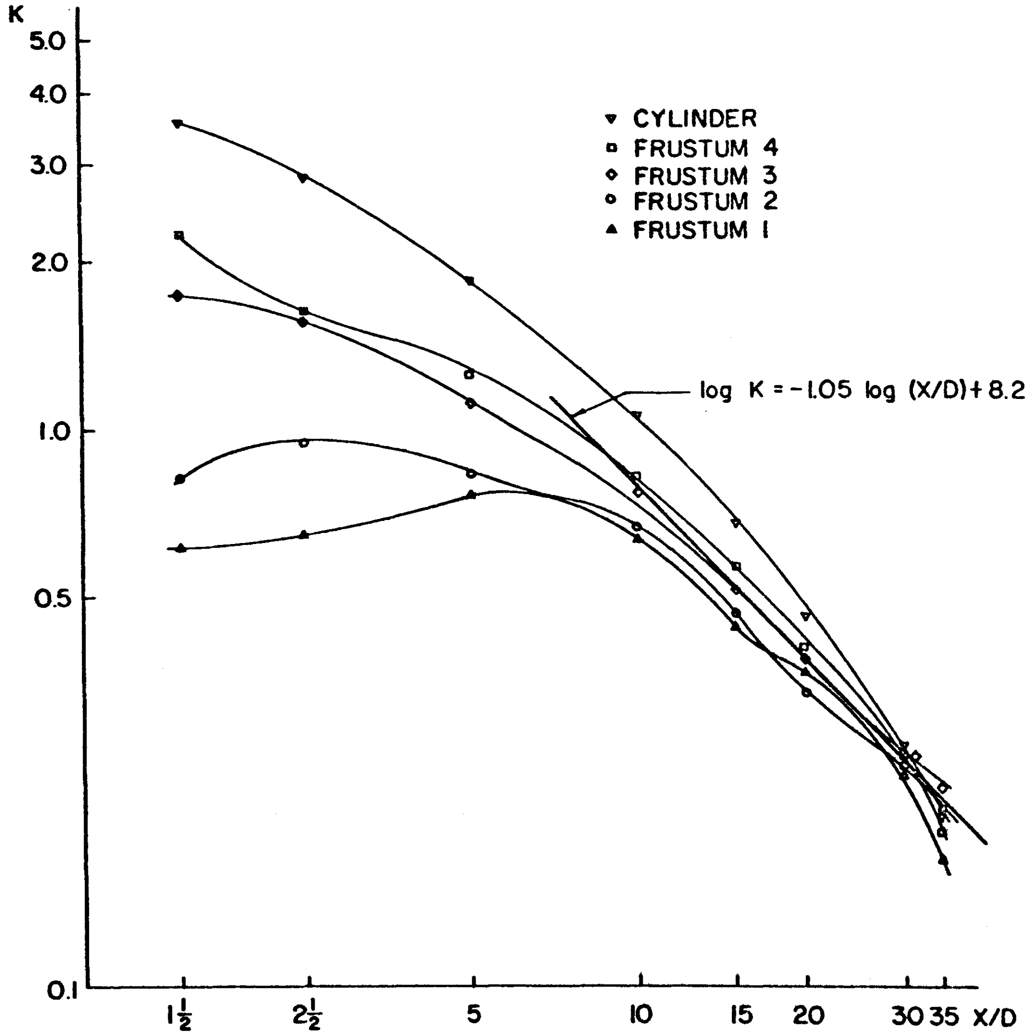

Fig. 49. All models side top θ= 0° release.

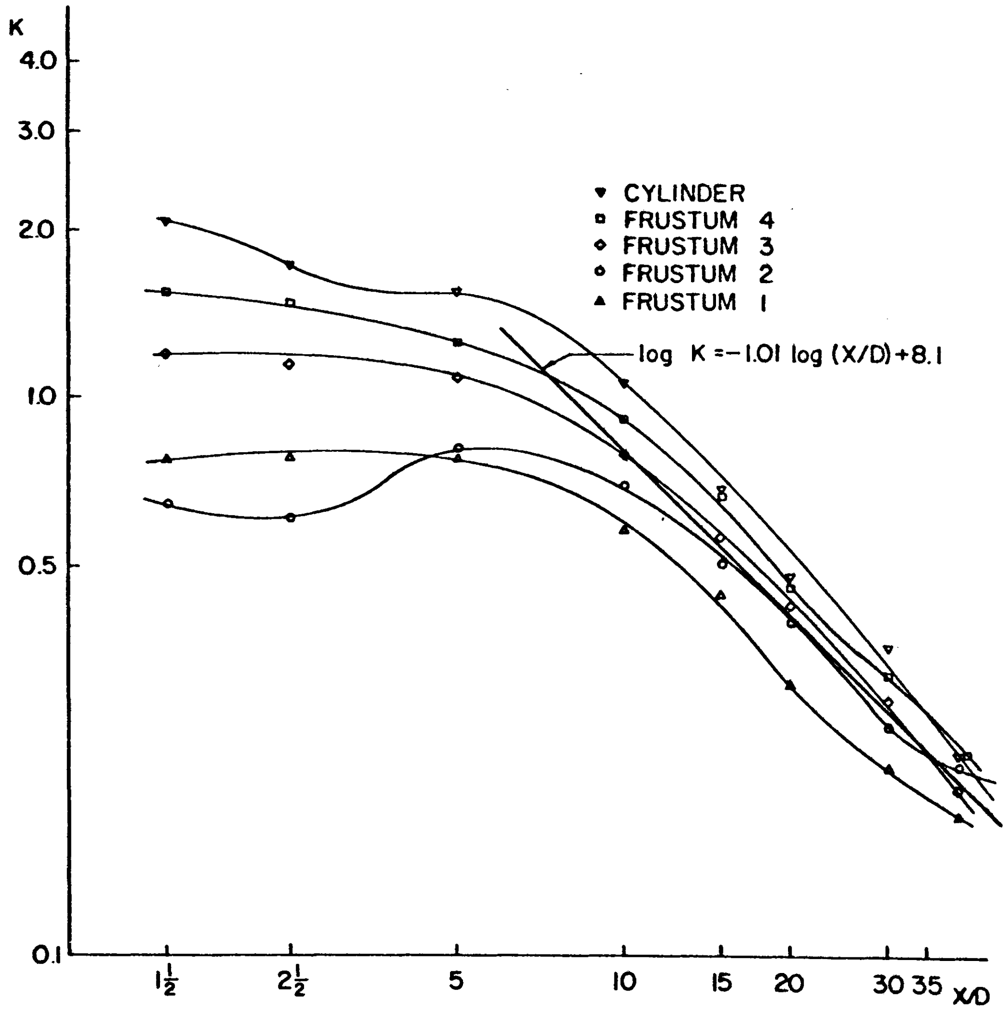

Fig. 50. All models side top θ = 90° release.

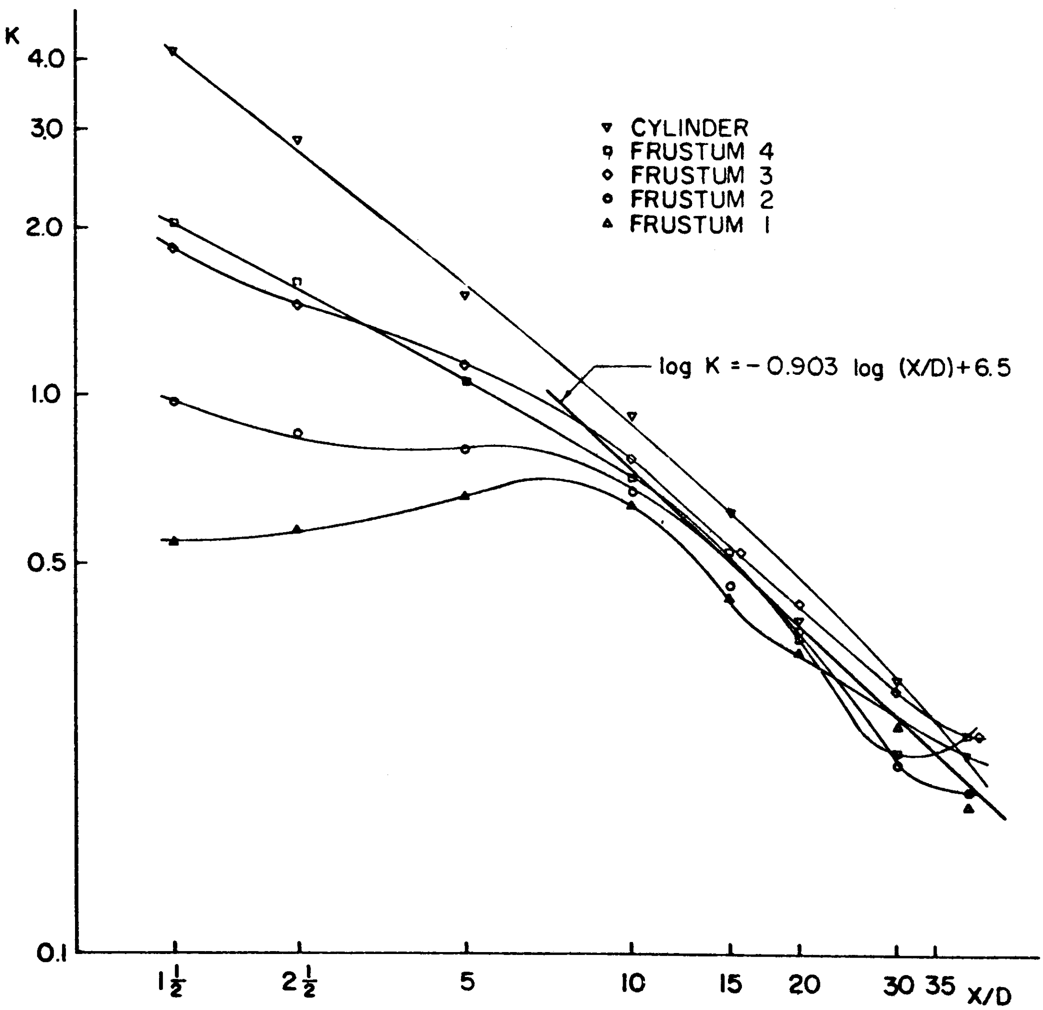

Fig. 51. All models side top $\theta = 180°$ release.

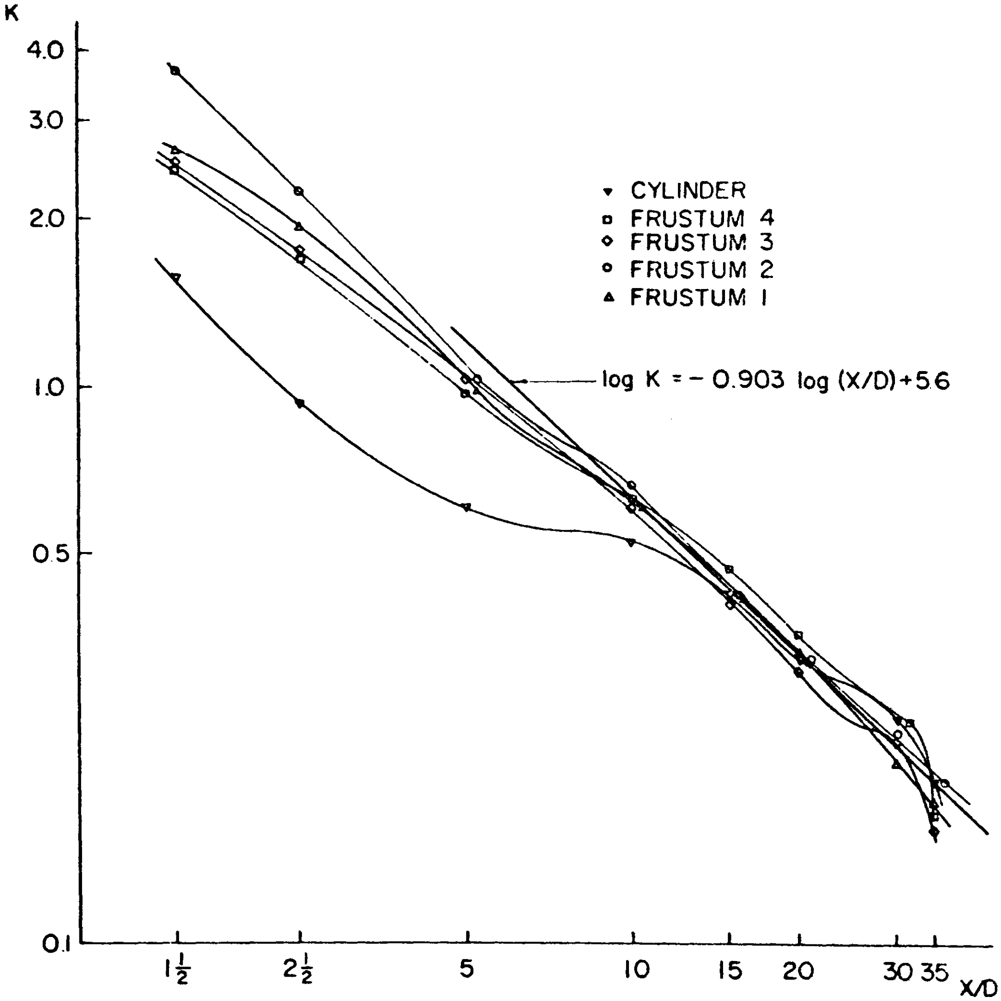

Fig. 52. All models side bottom θ = 0° release.

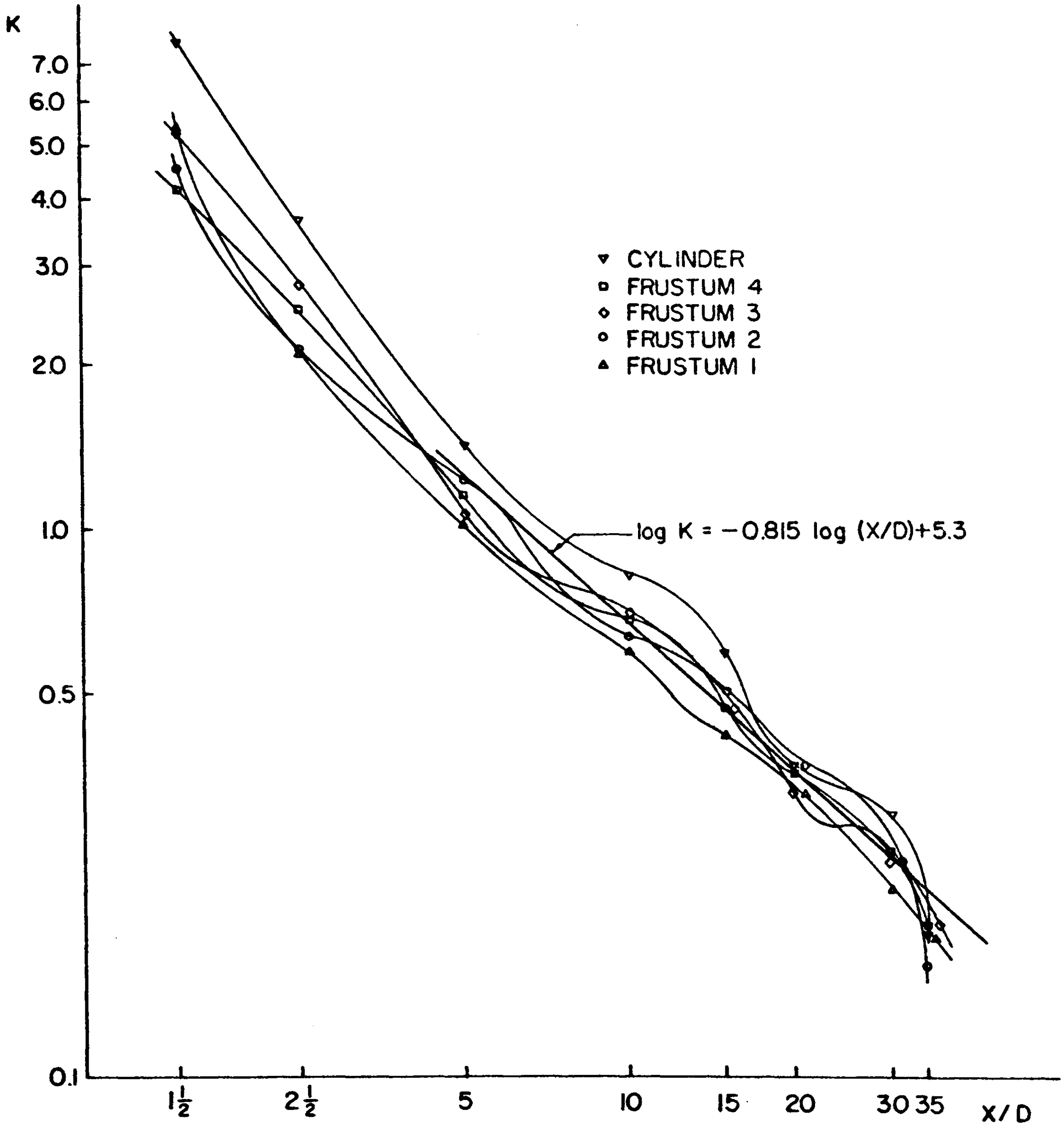

Fig. 53. All models side bottom θ = 90° release.

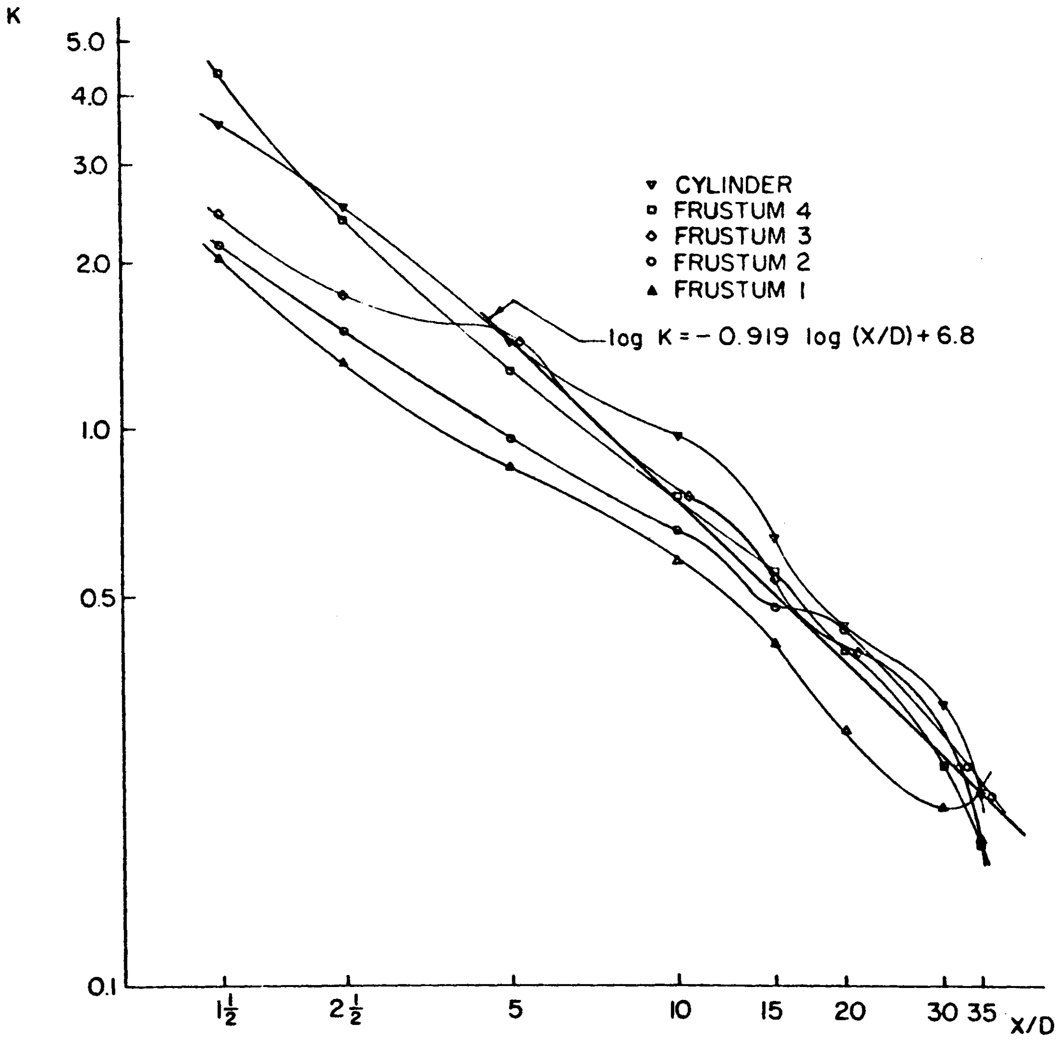

Fig. 54. All models side bottom θ = 180° release.

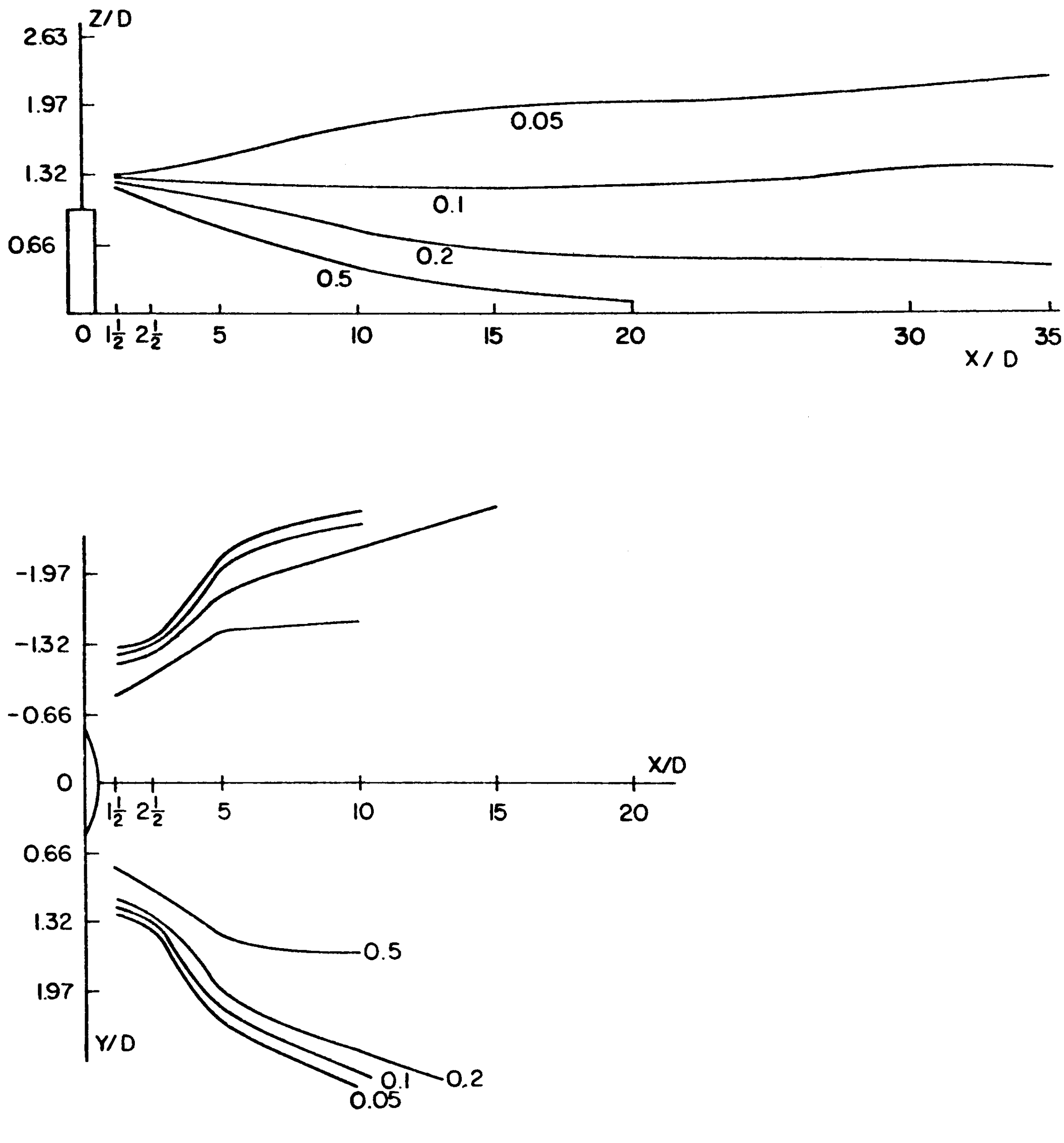

Fig. 55. Cylinder top release.

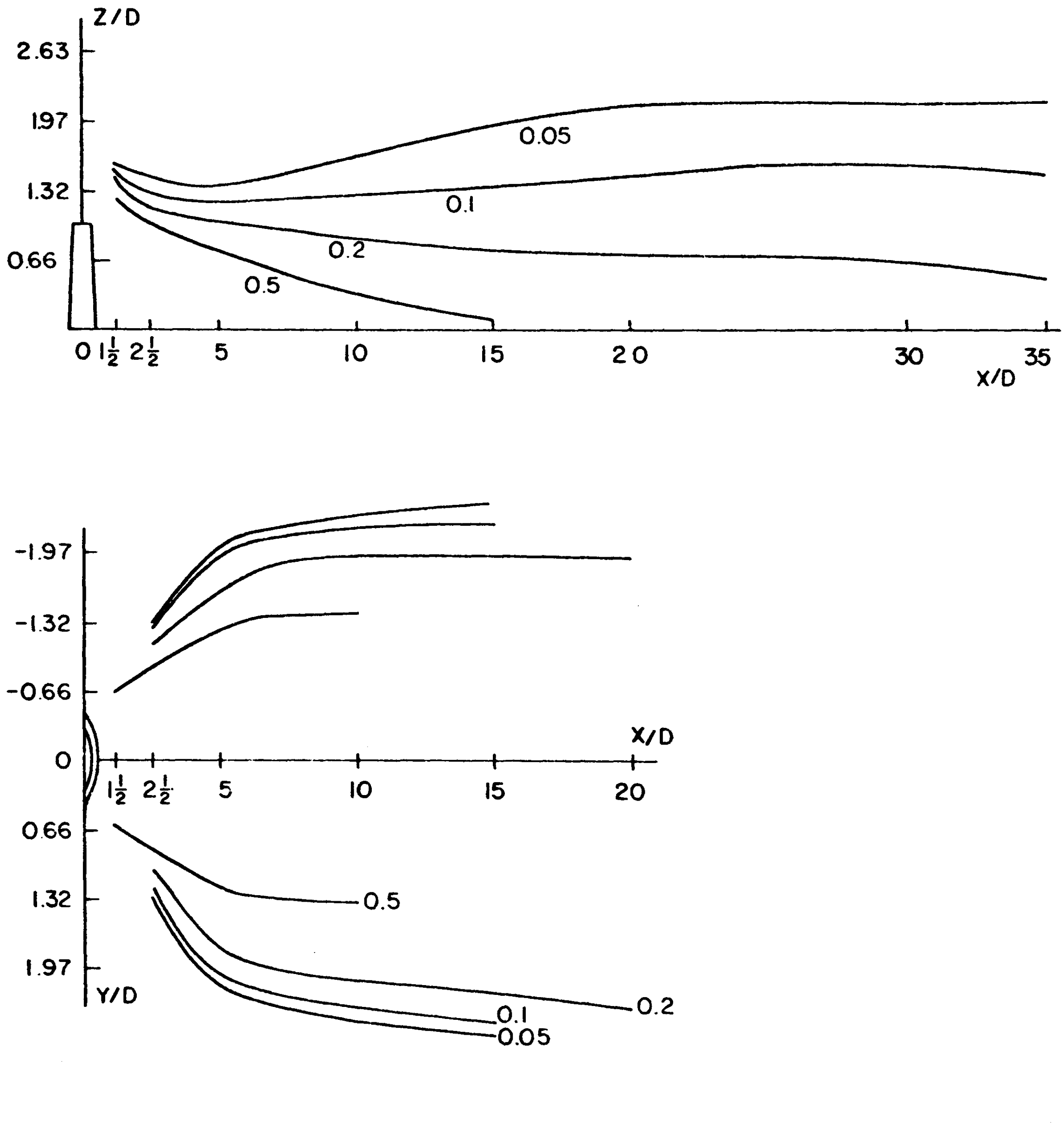

Fig. 56. Frustum 4 top release.

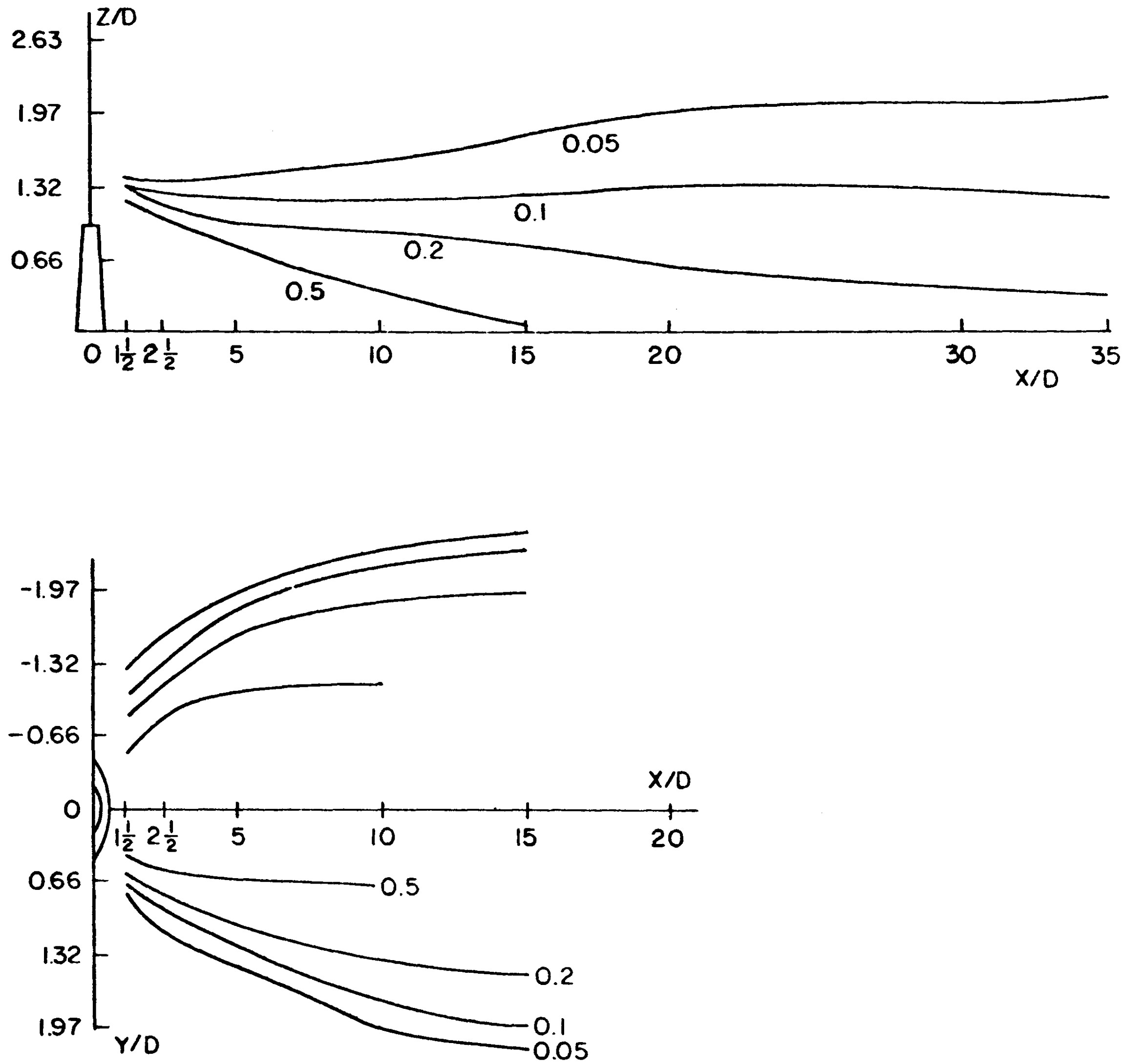

Fig. 57. Frustum 3 top release.

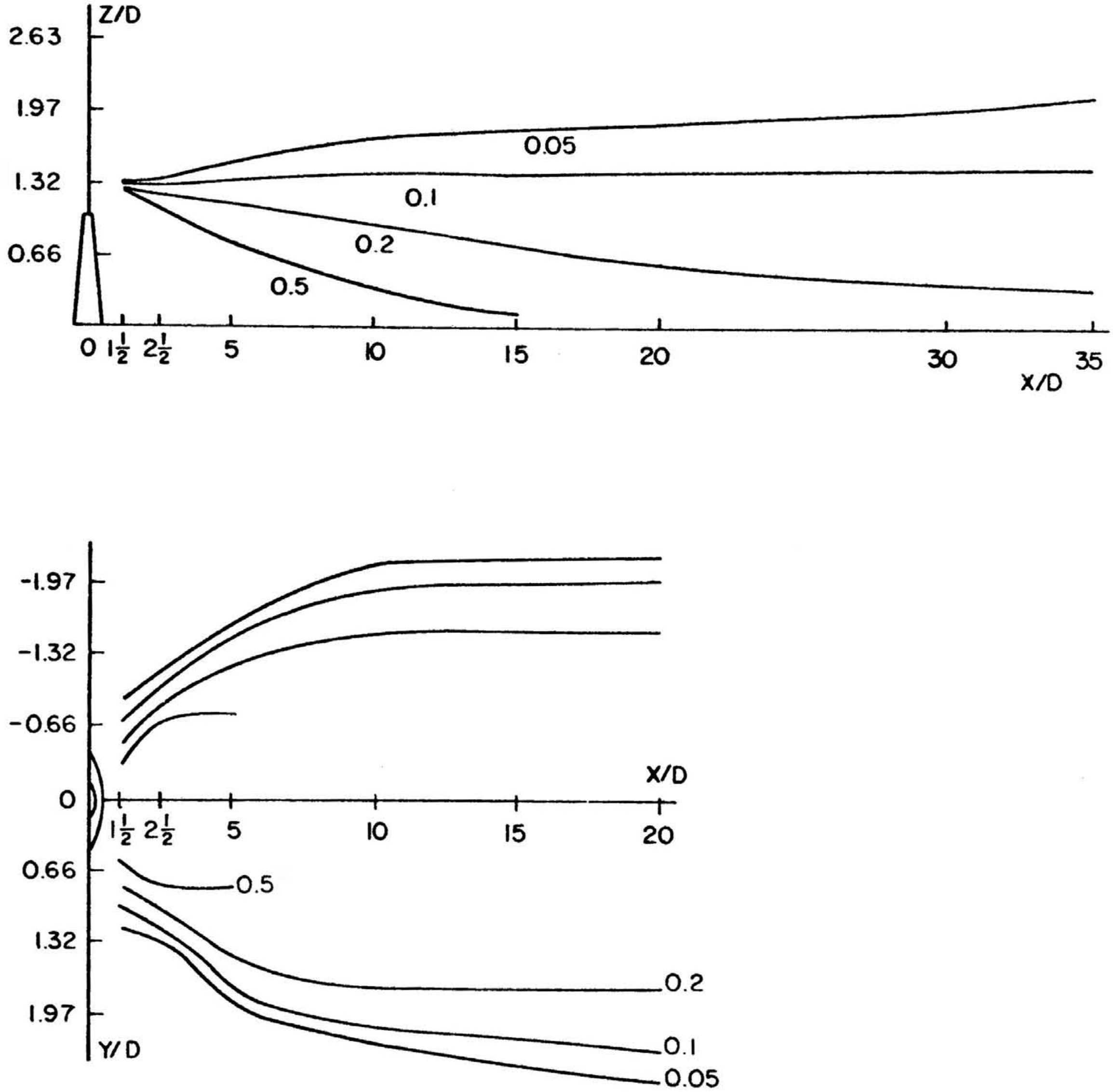

Fig. 58. Frustum 2 top release.

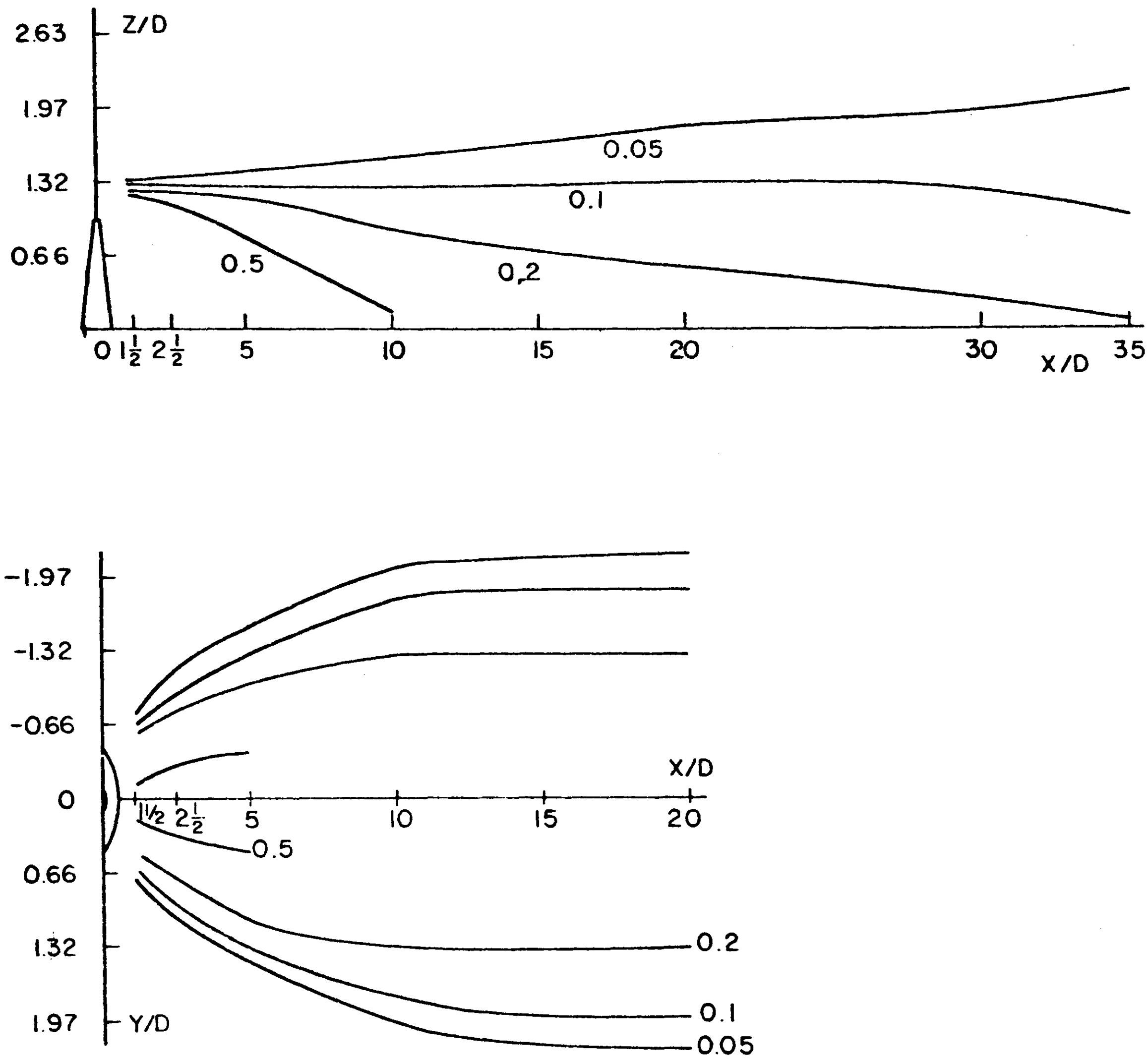

Fig. 59. Frustum 1 top release.

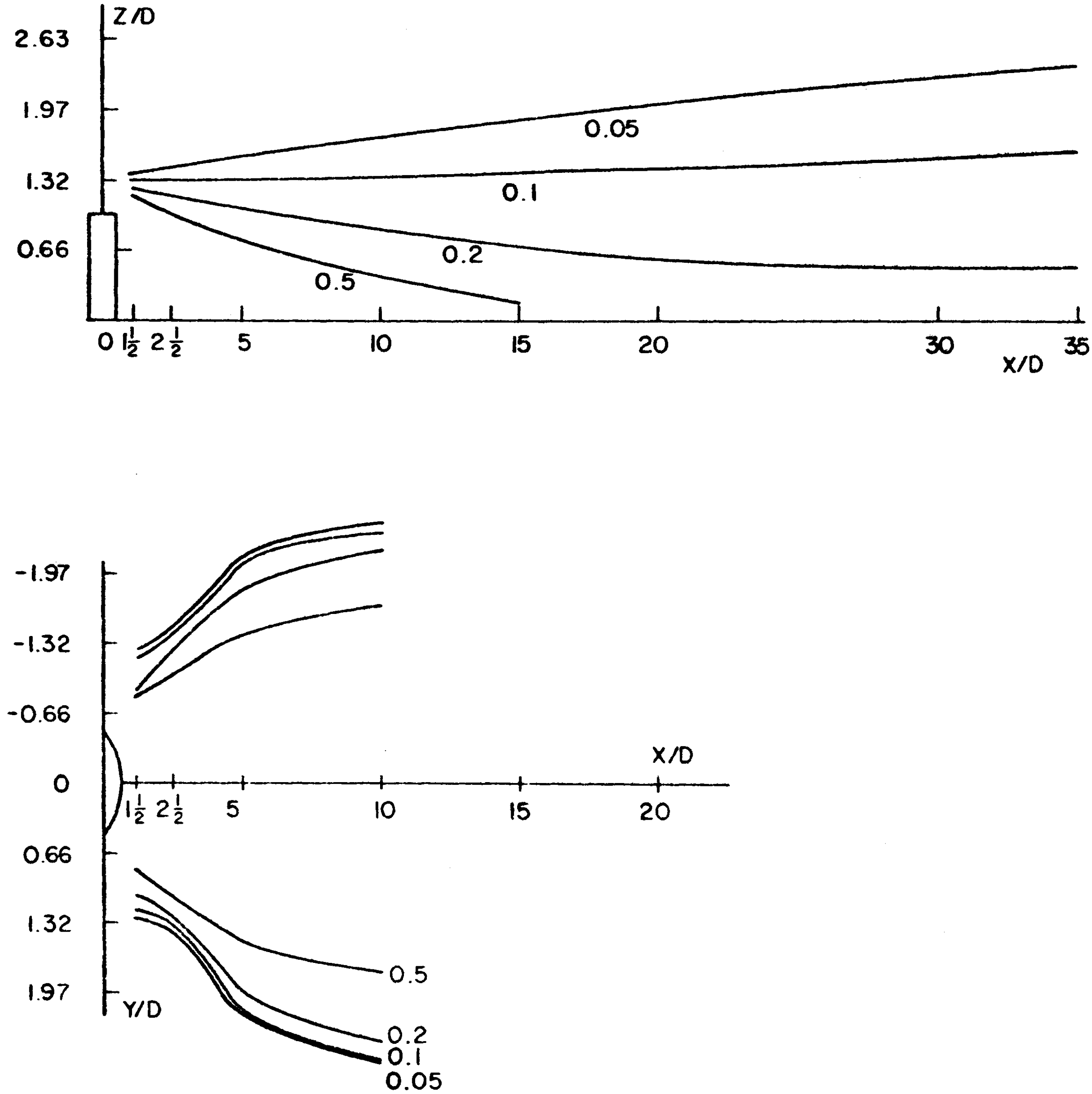

Fig. 60. Cylinder side top θ = 0° release.

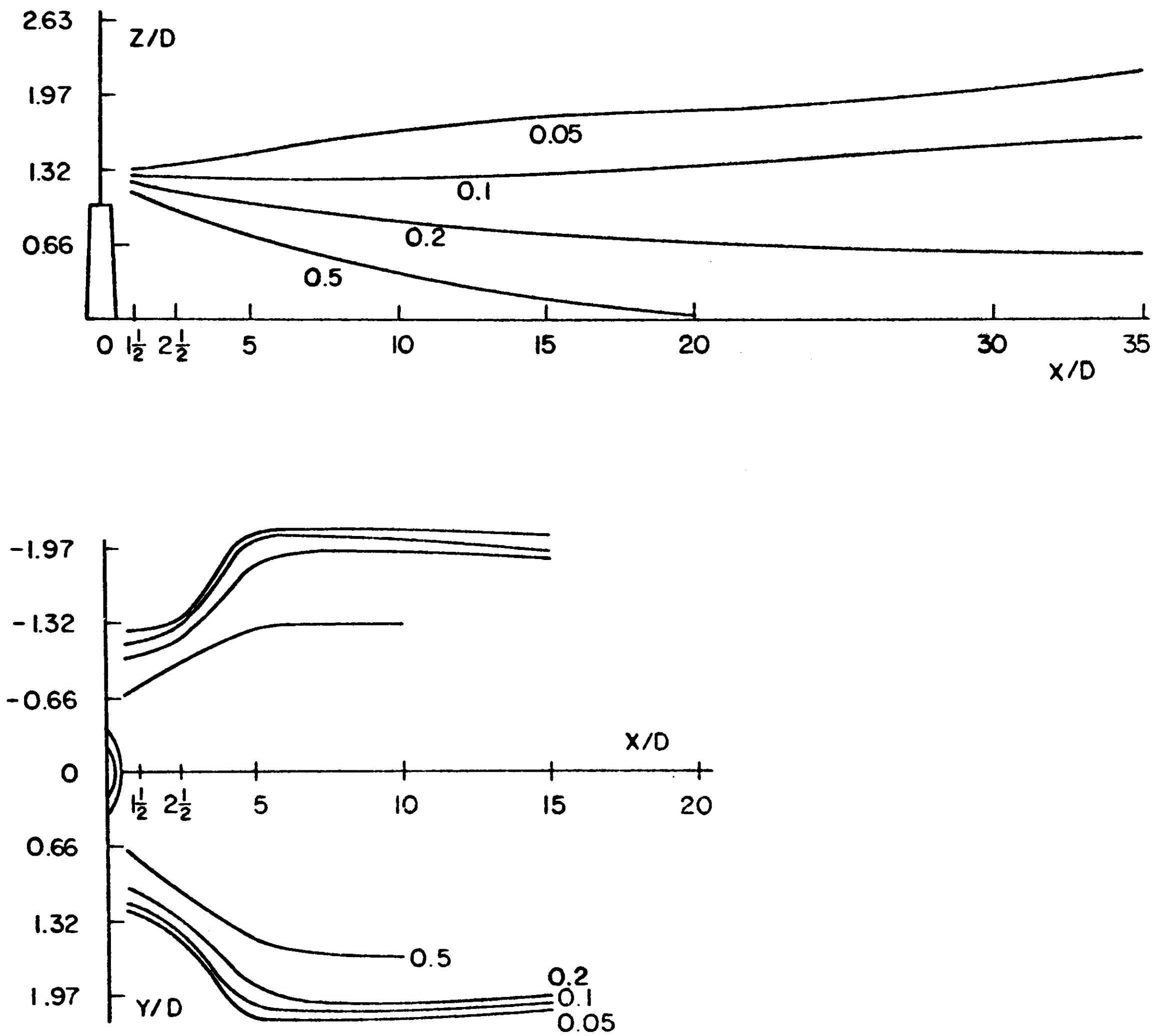

Fig. 61. Frustum 4 side top $\theta = 0°$ release.

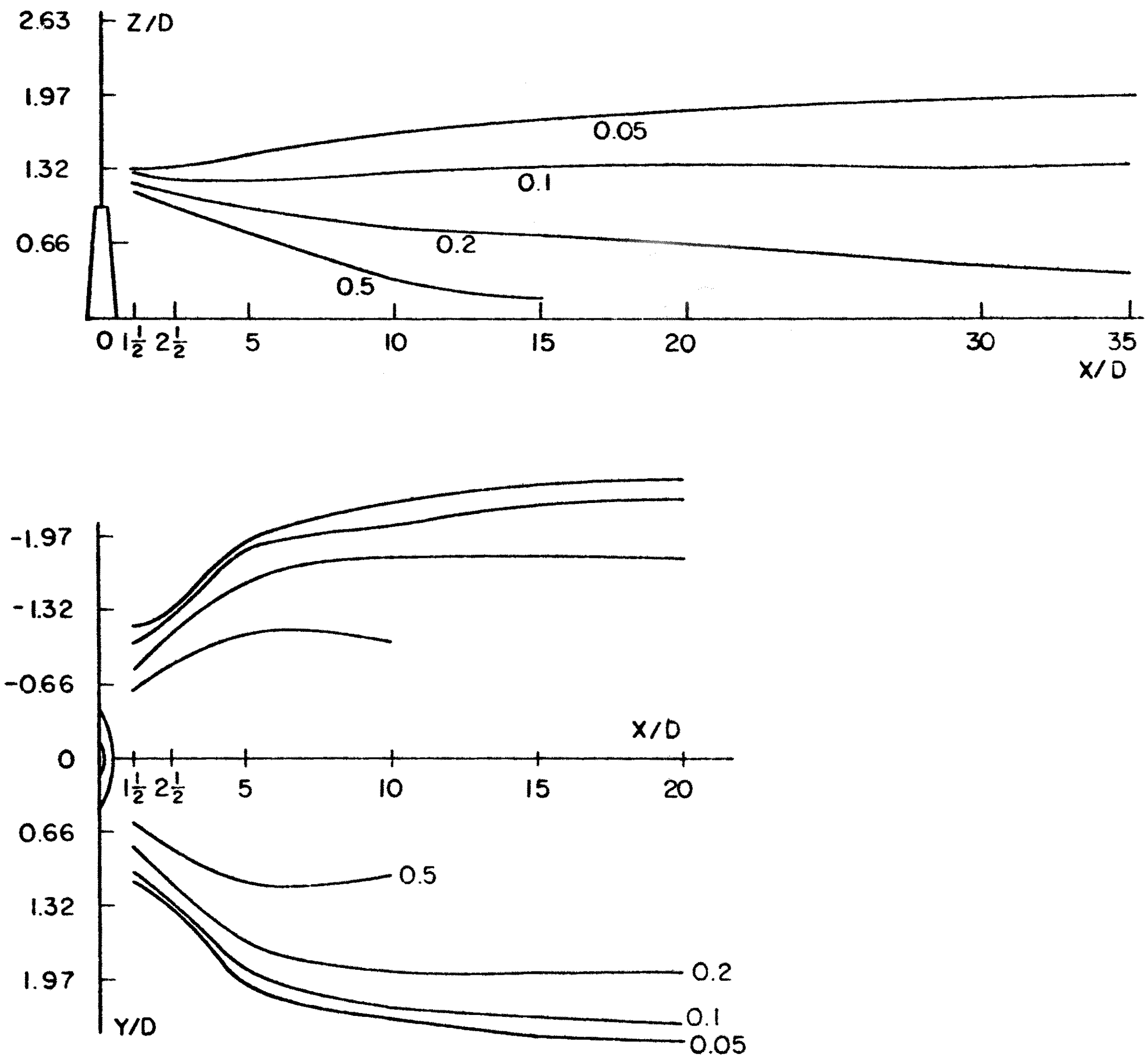

Fig. 62. Frustum 3 side top $\theta = 0°$ release.

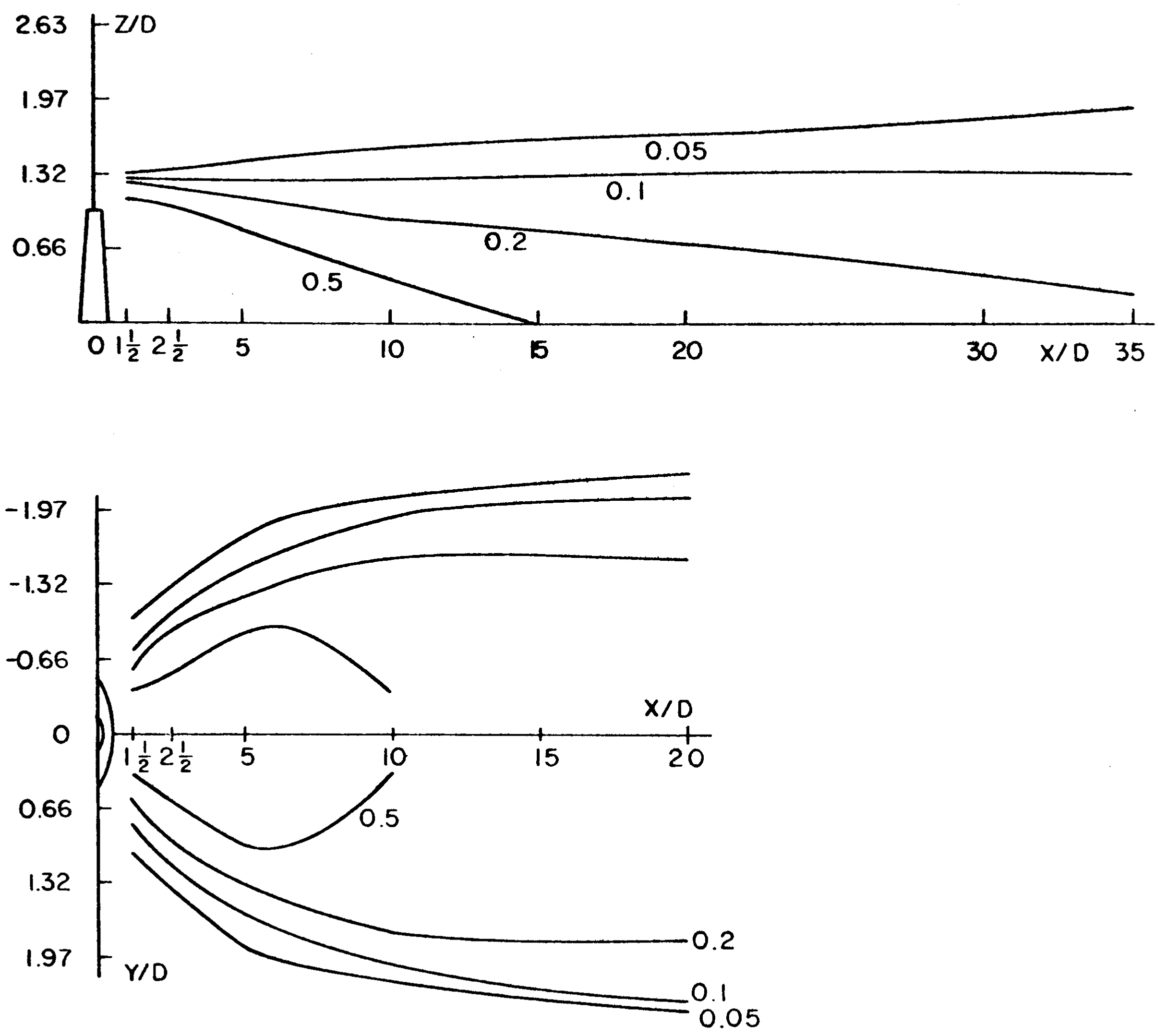

Fig. 63. Frustum 2 side top θ = 0° release.

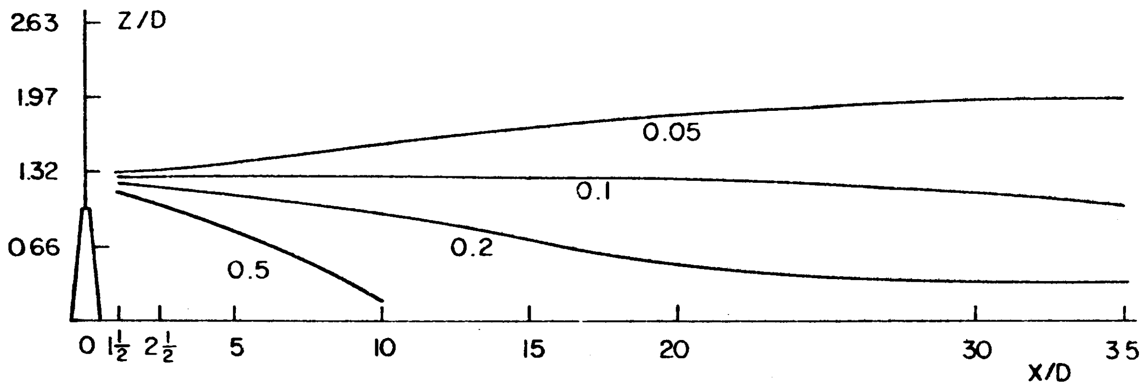

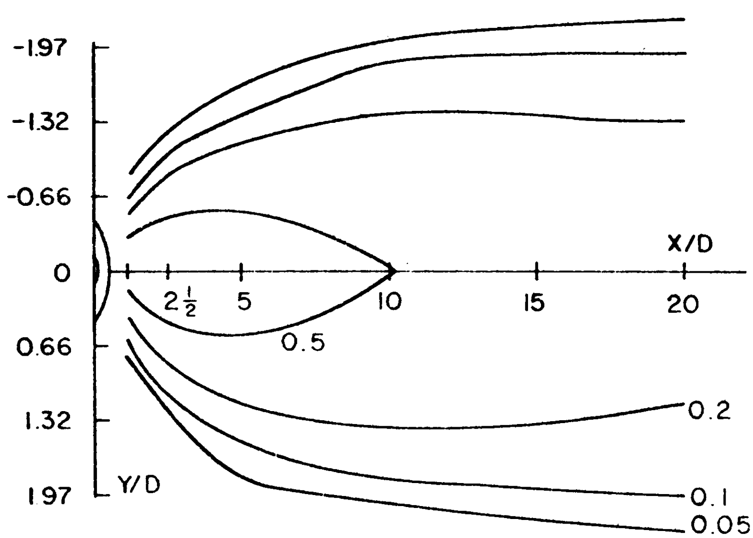

Fig. 64. Frustum 1 side top θ = 0° release.

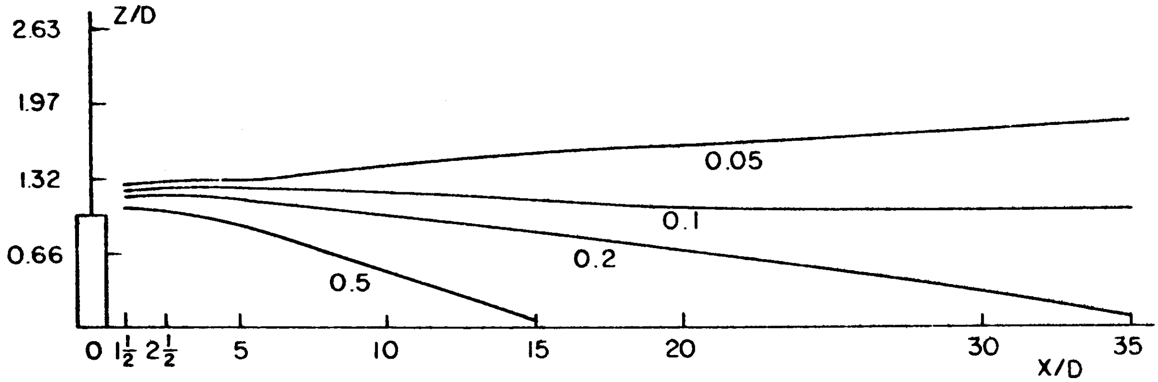

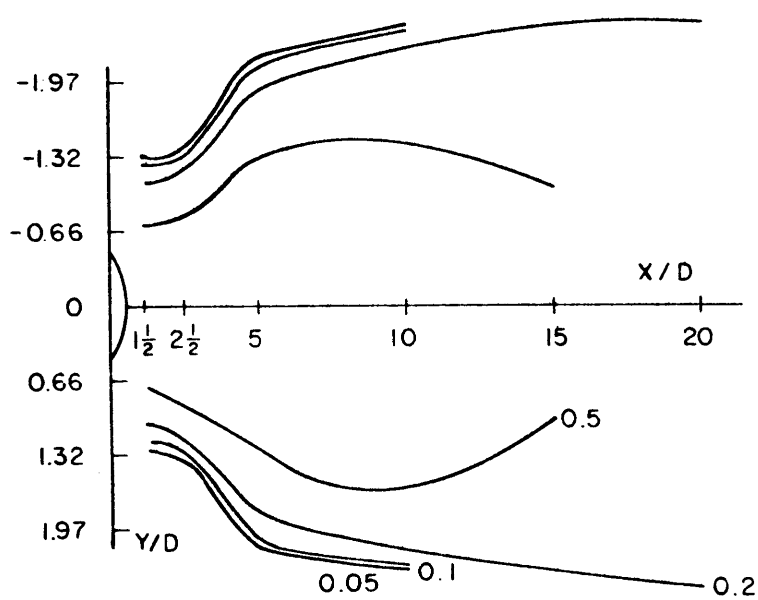

Fig. 65. Cylinder side top θ = 90° release.

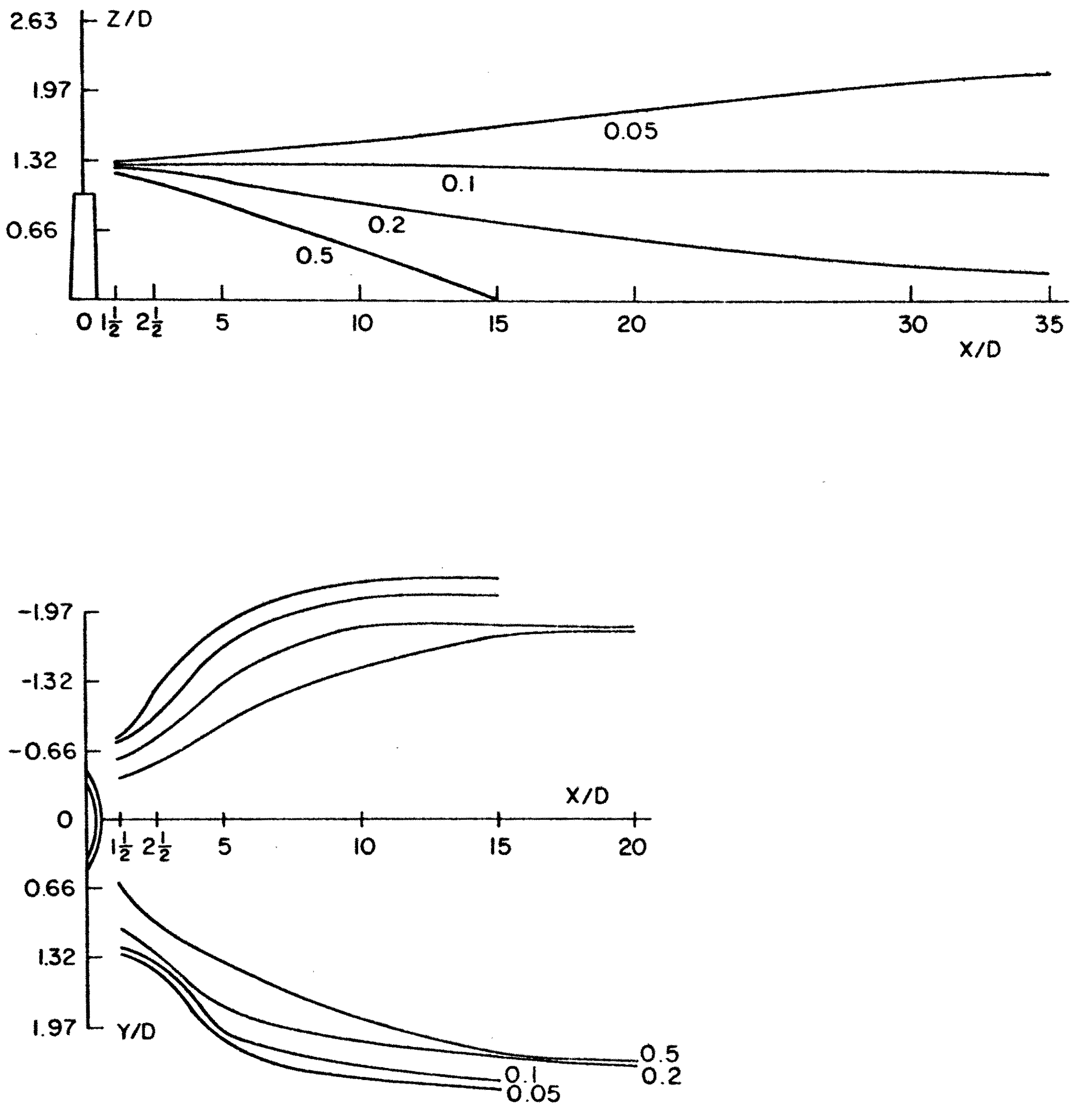

Fig. 66. Frustum 4 side top $\theta = 90°$ release.

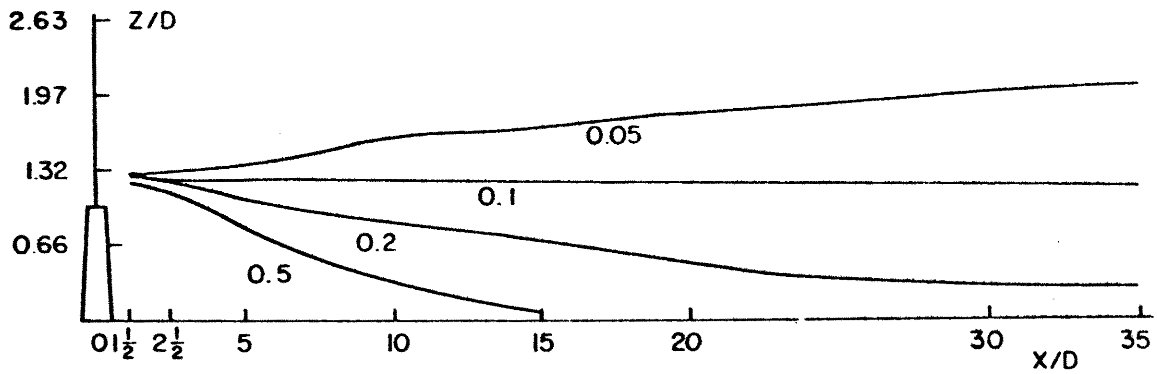

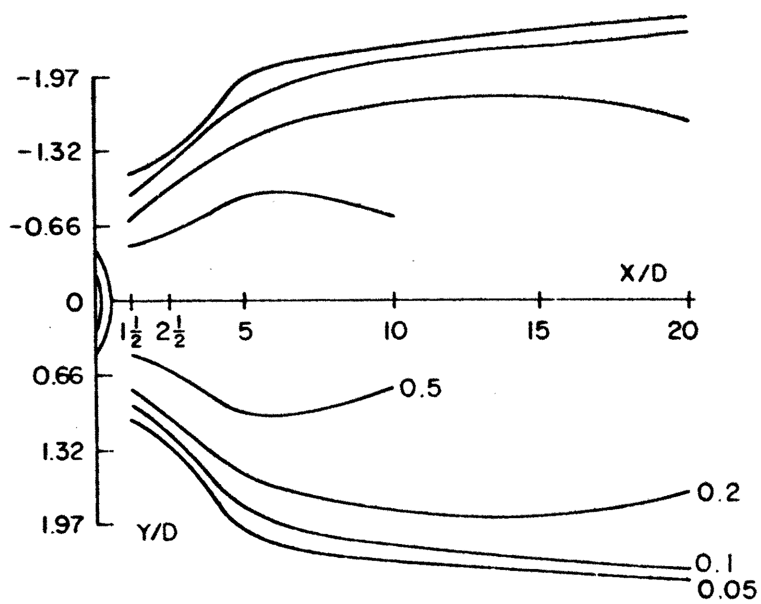

Fig. 67. Frustum 3 side top θ = 90° release.

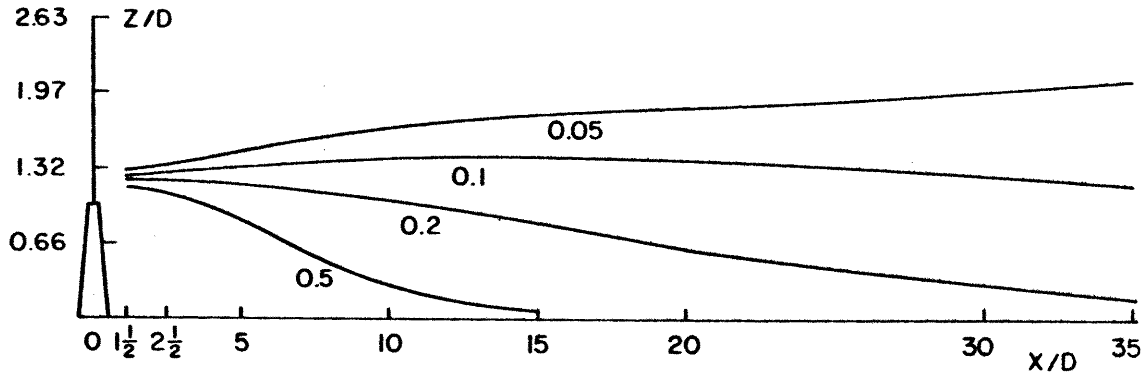

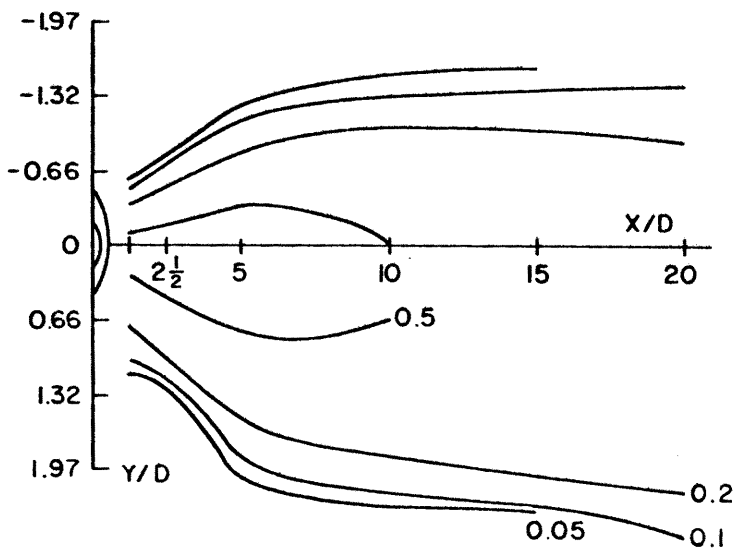

Fig. 68. Frustum 2 side top $\theta = 90°$ release.

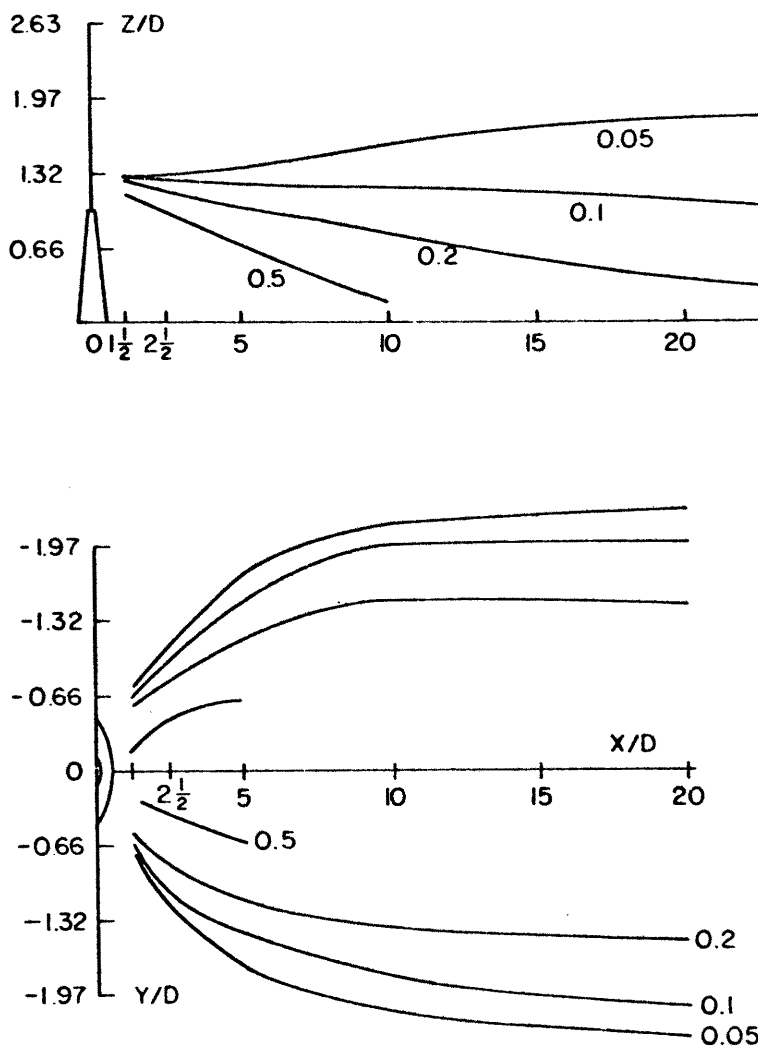

Fig. 69. Frustum 1 side top θ = 90° release.

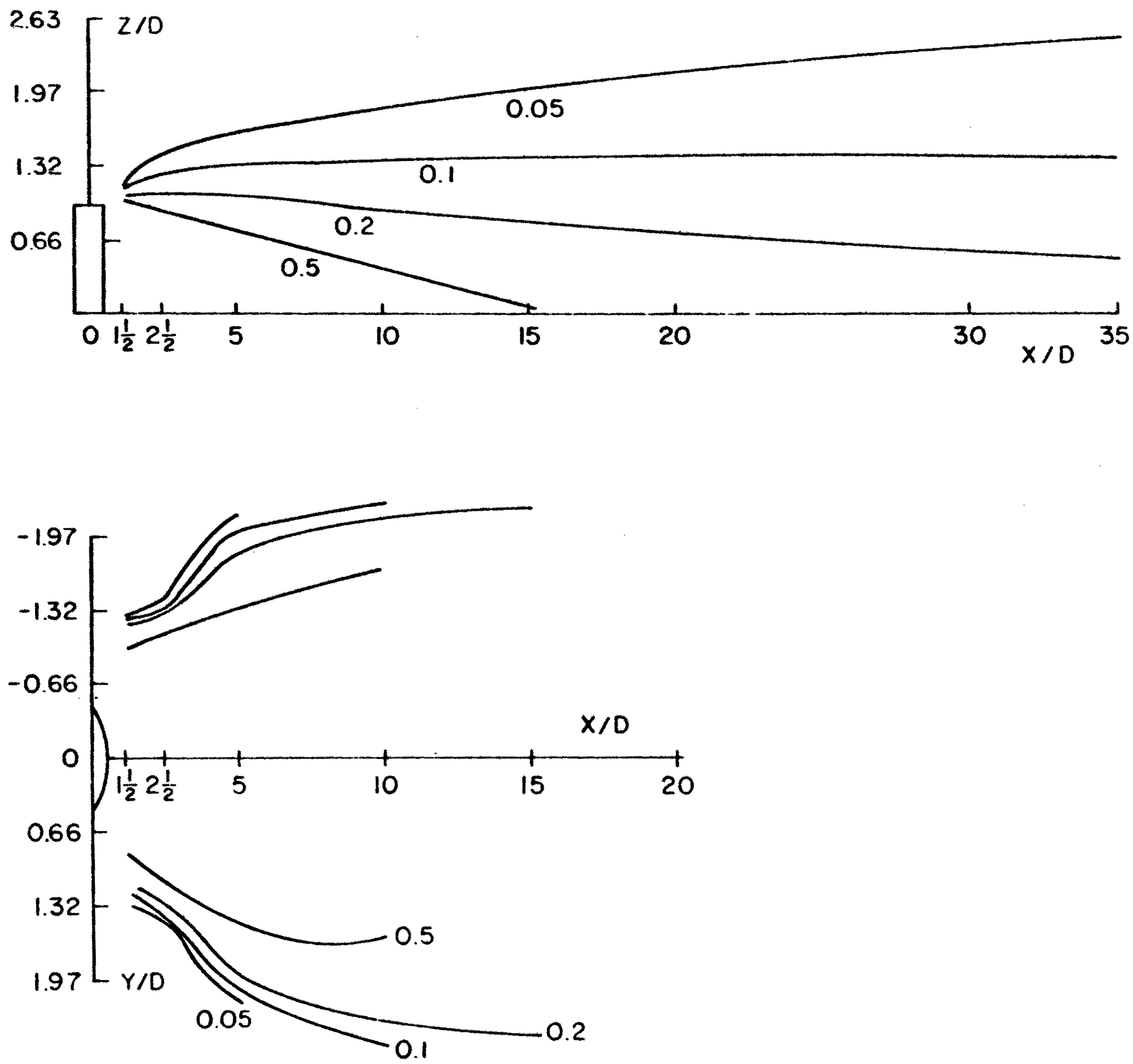

Fig. 70. Cylinder side top $\theta = 180°$ release.

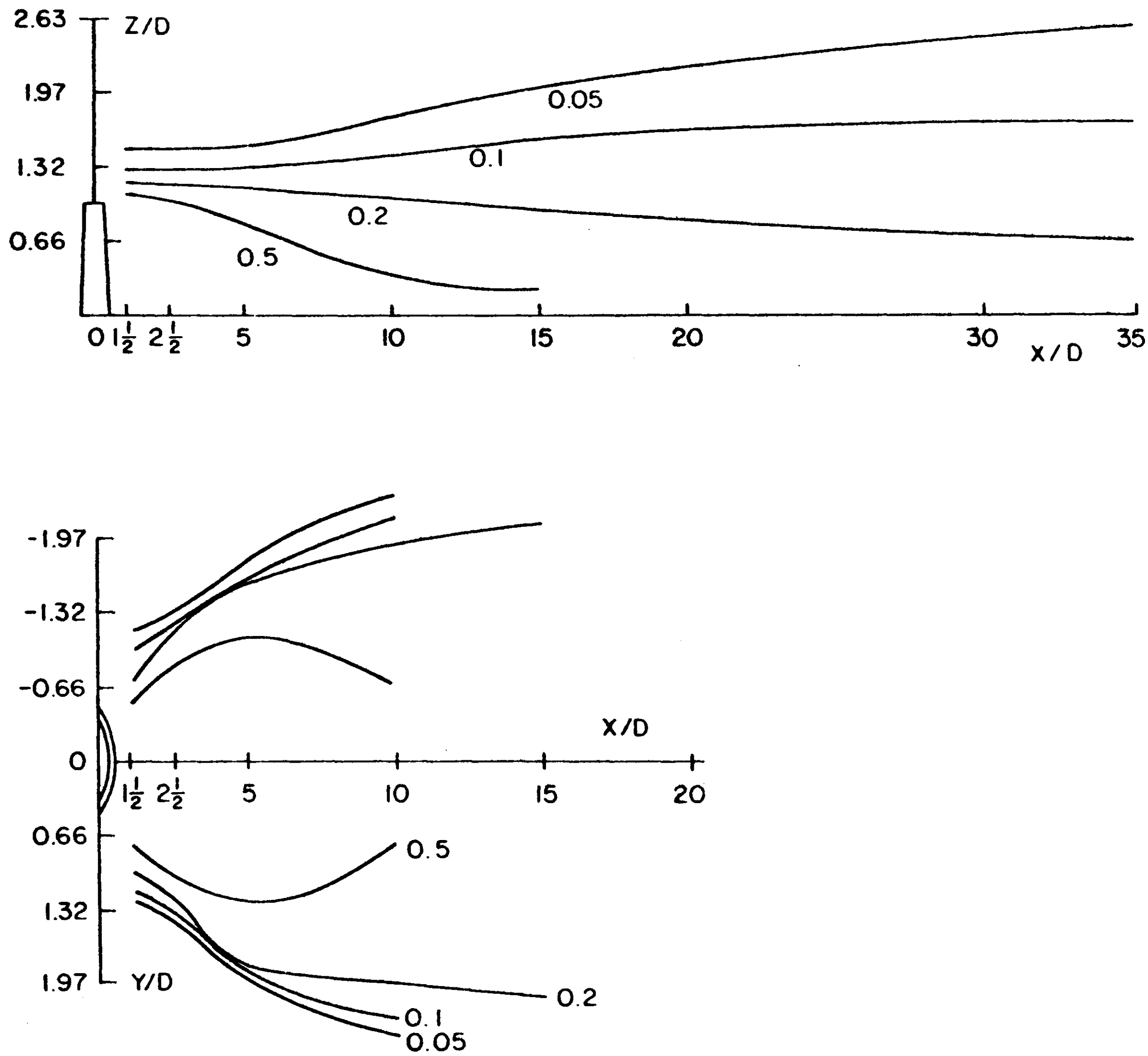

Fig. 71. Frustum 4 side top $\theta = 180°$ release.

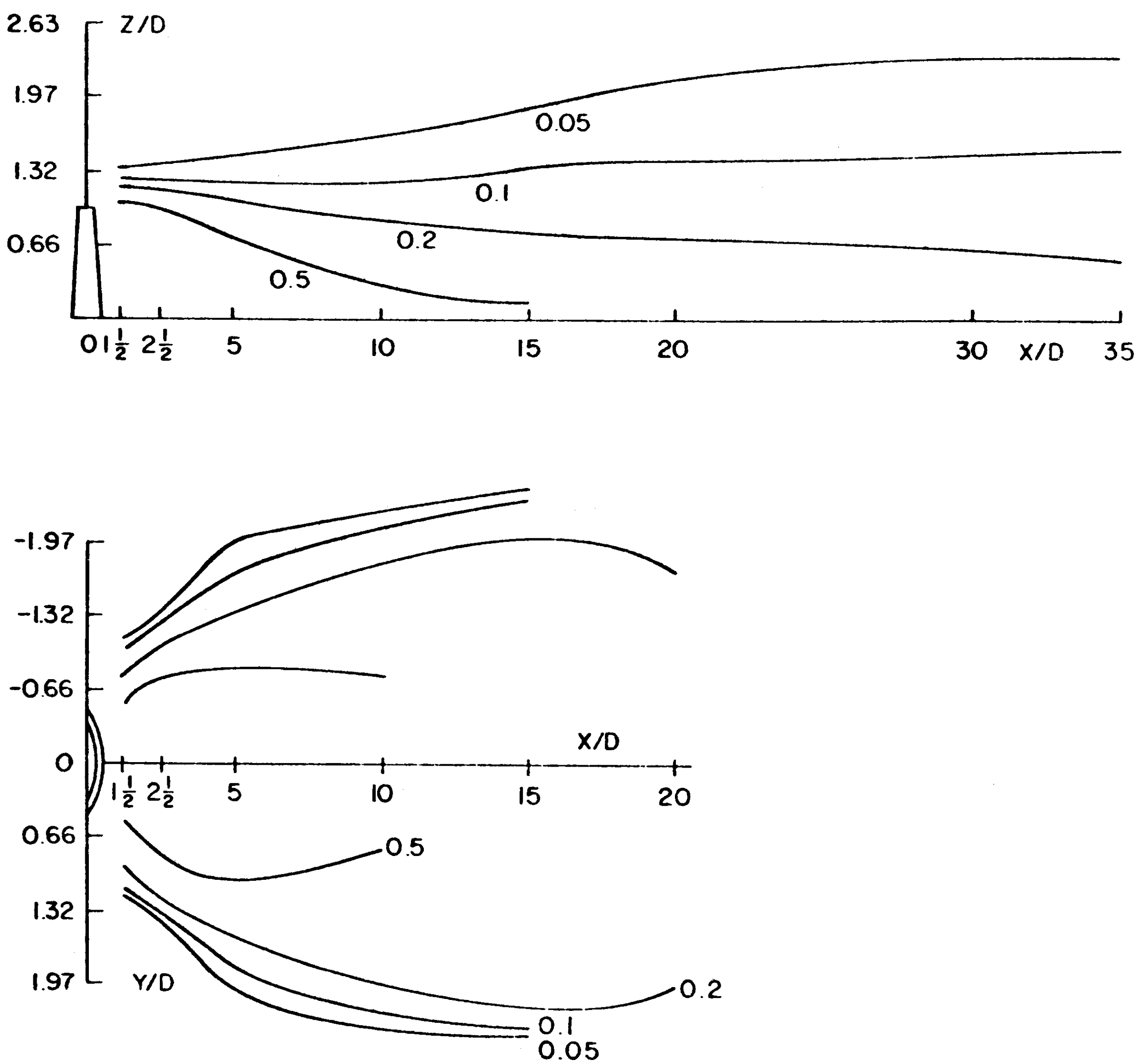

Fig. 72. Frustum 3 side top θ = 180° release.

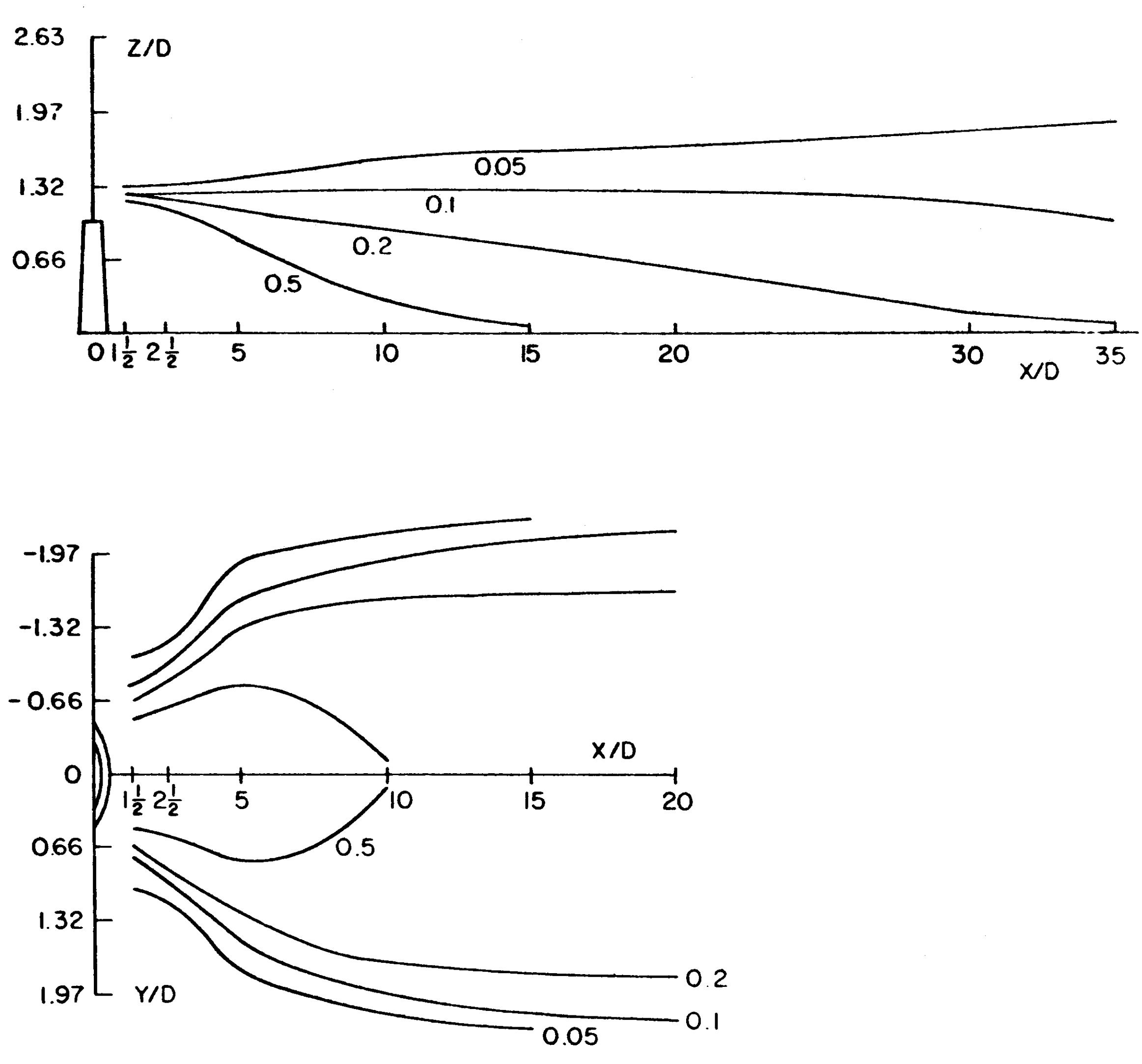

Fig. 73. Frustum 2 side top $\theta = 180°$ release.

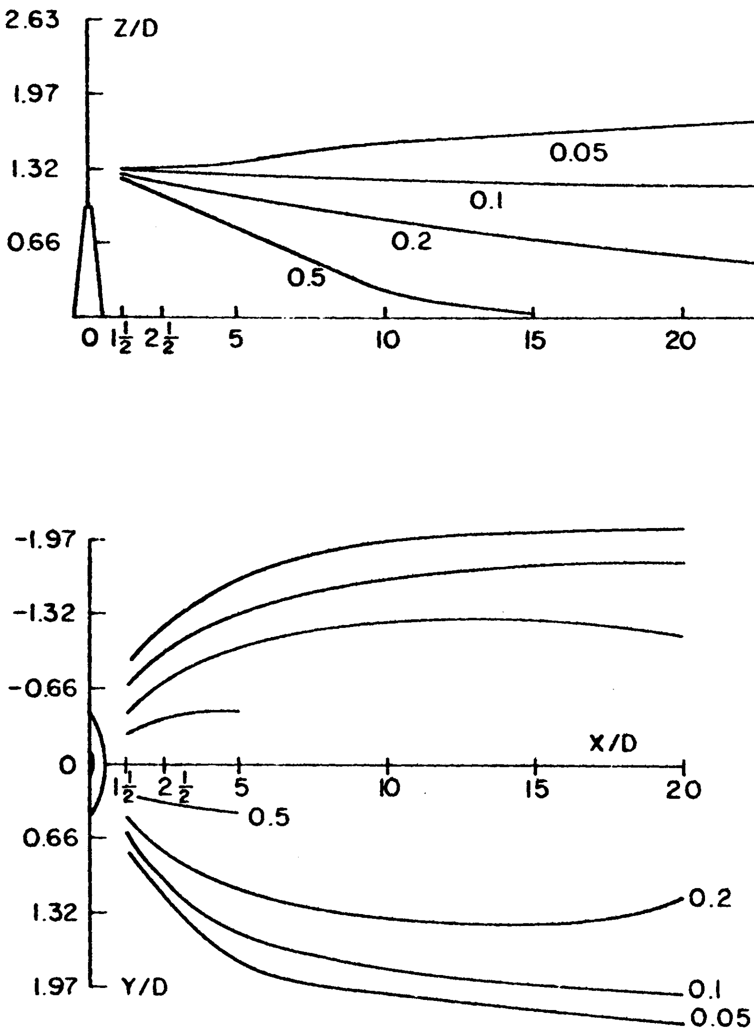

Fig. 74. Frustum 1 side top θ = 180° release.

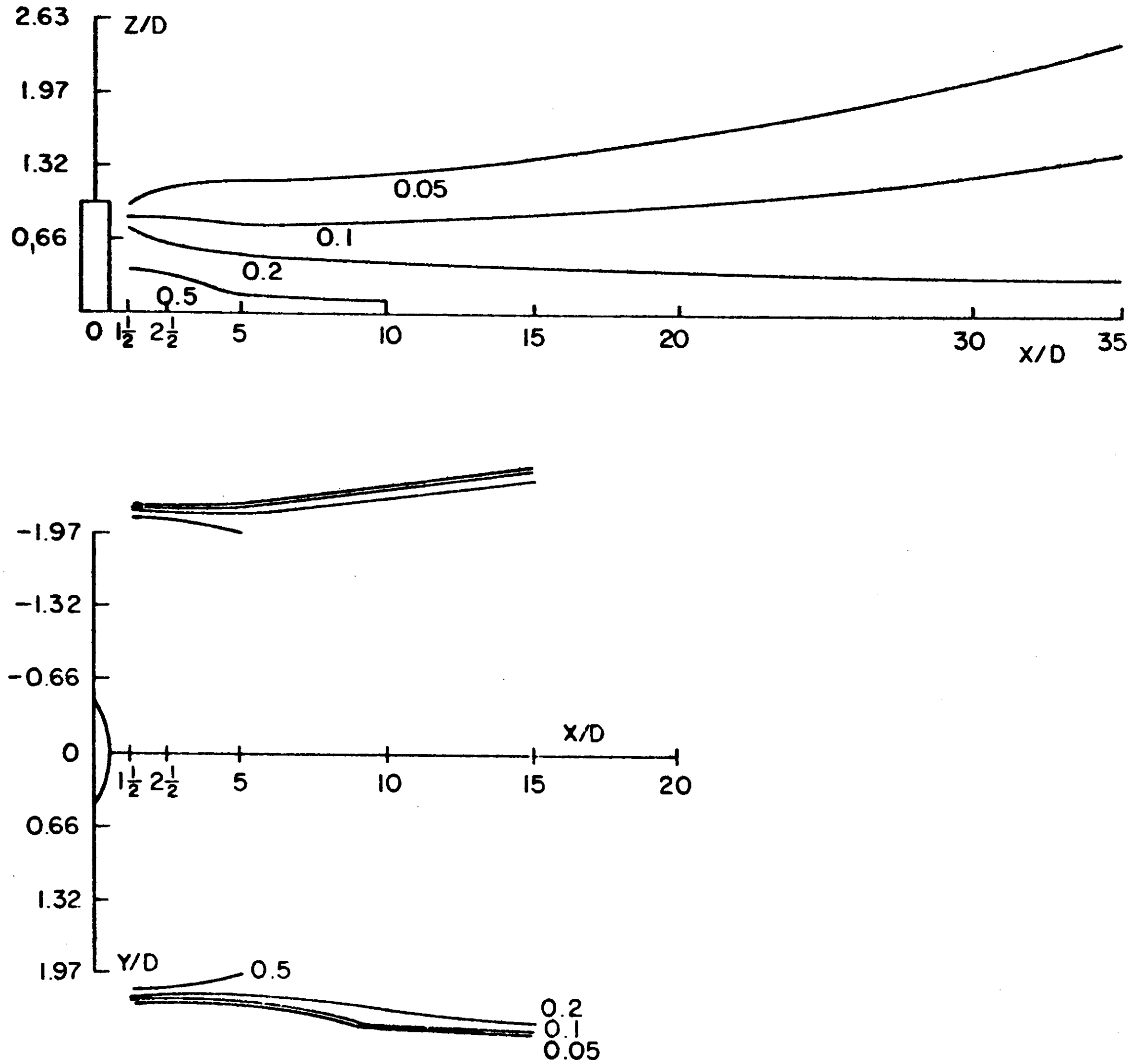

Fig. 75. Cylinder side bottom $\theta = 0°$ release.

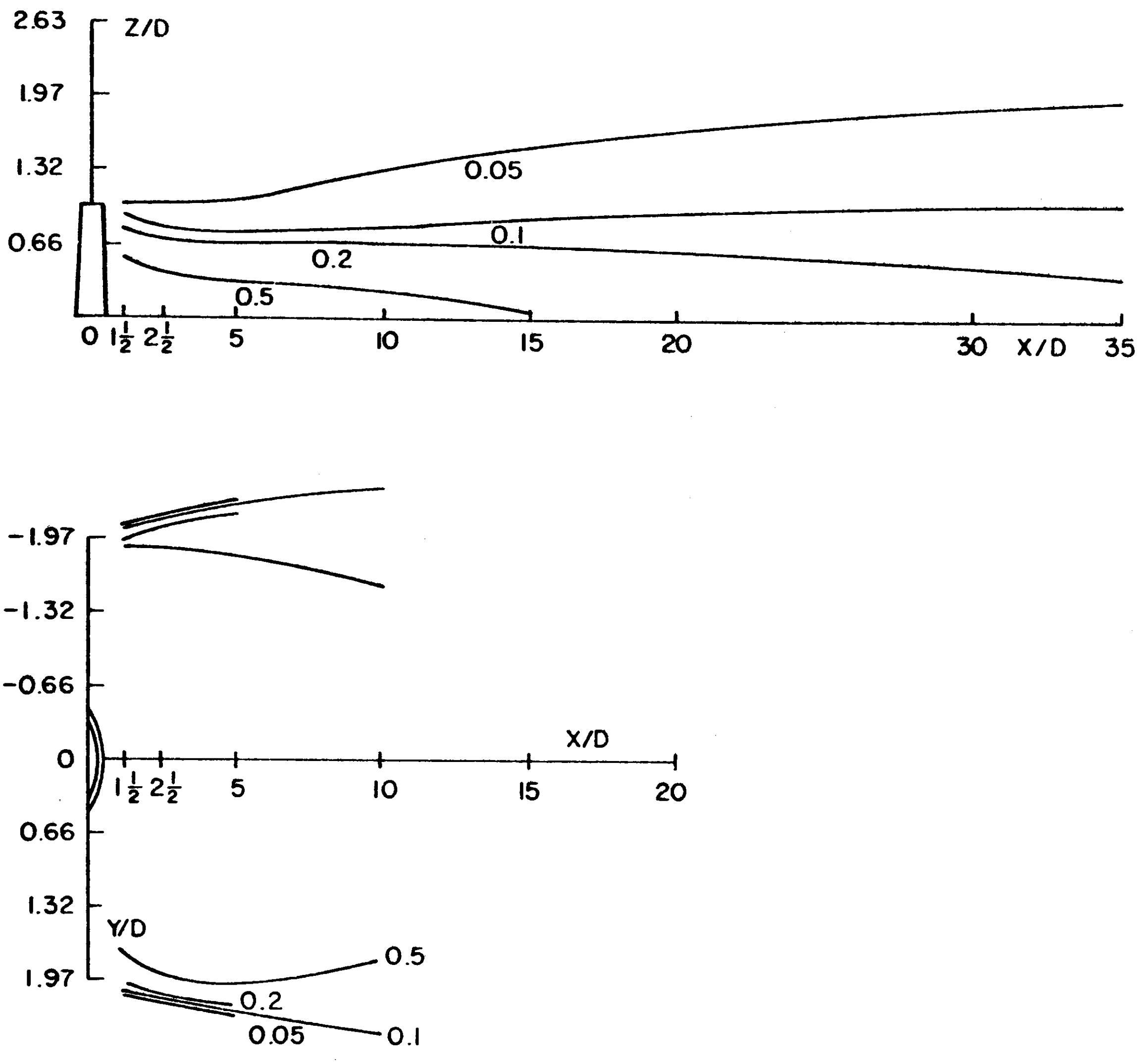

Fig. 76. Frustum 4 side bottom $\theta = 0°$ release.

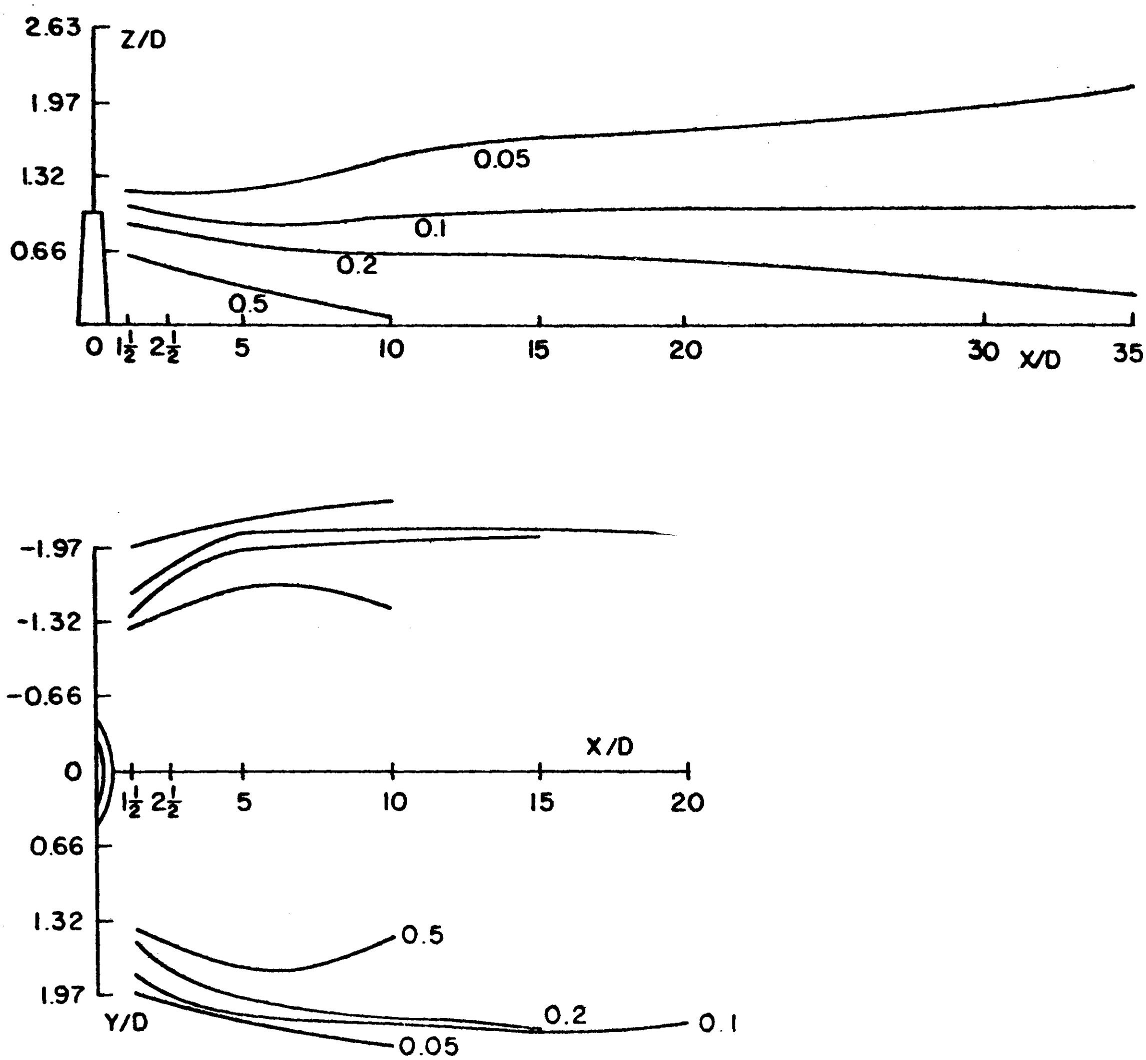

Fig. 77. Frustum 3 side bottom θ = 0° release.

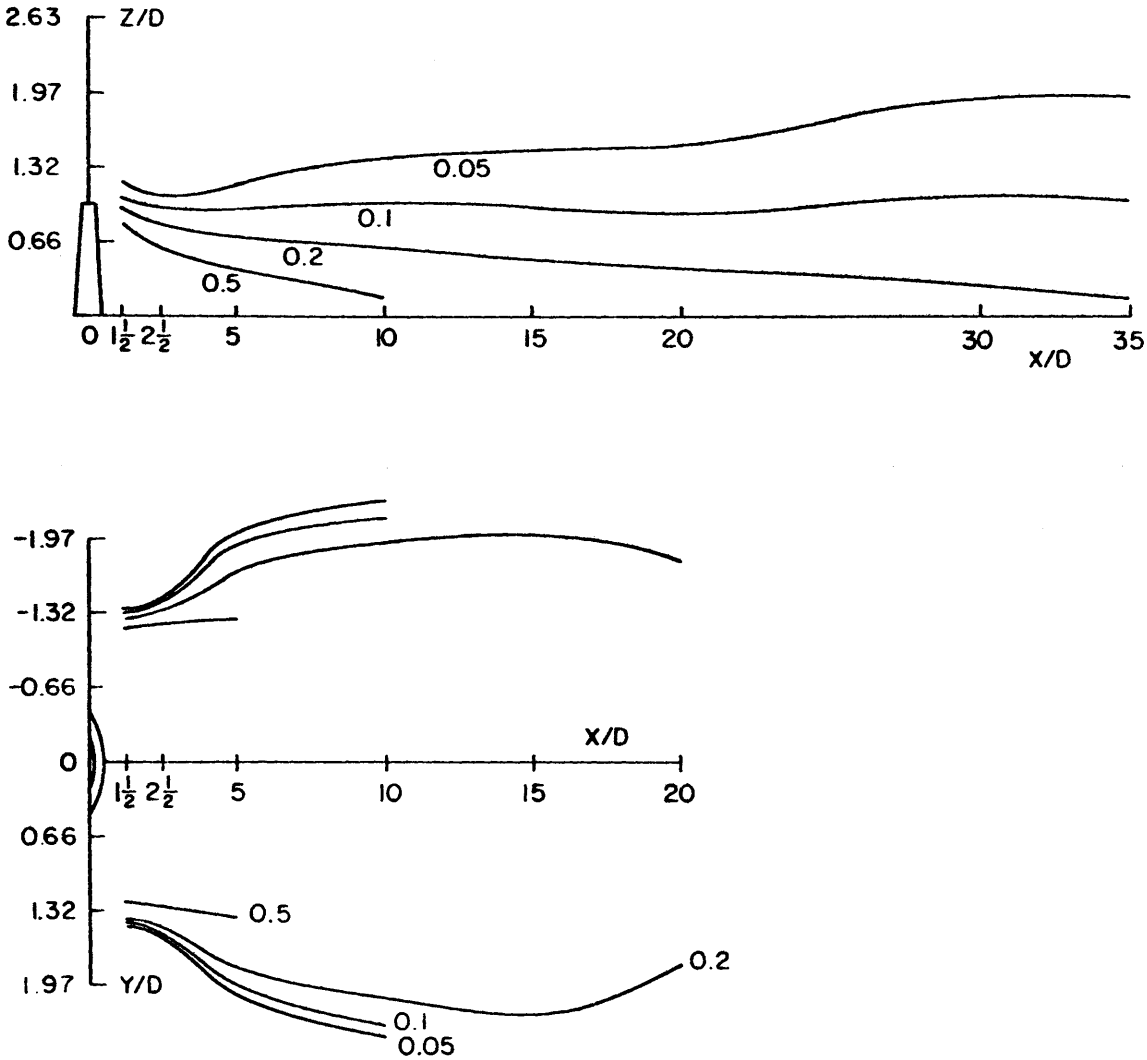

Fig. 78. Frustum 2 side bottom $\theta = 0°$ release.

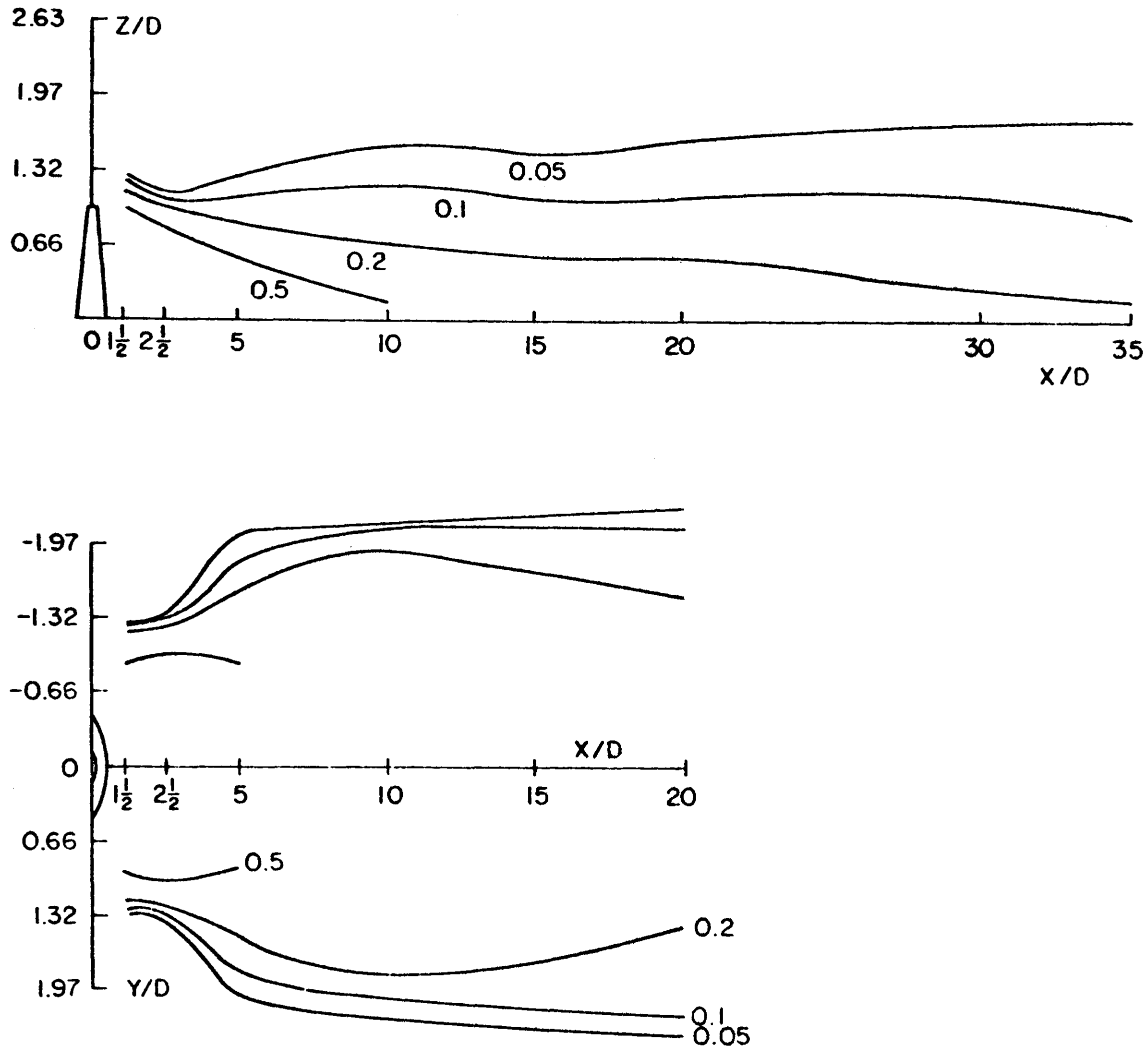

Fig. 79. Frustum 1 side bottom θ = 0° release.

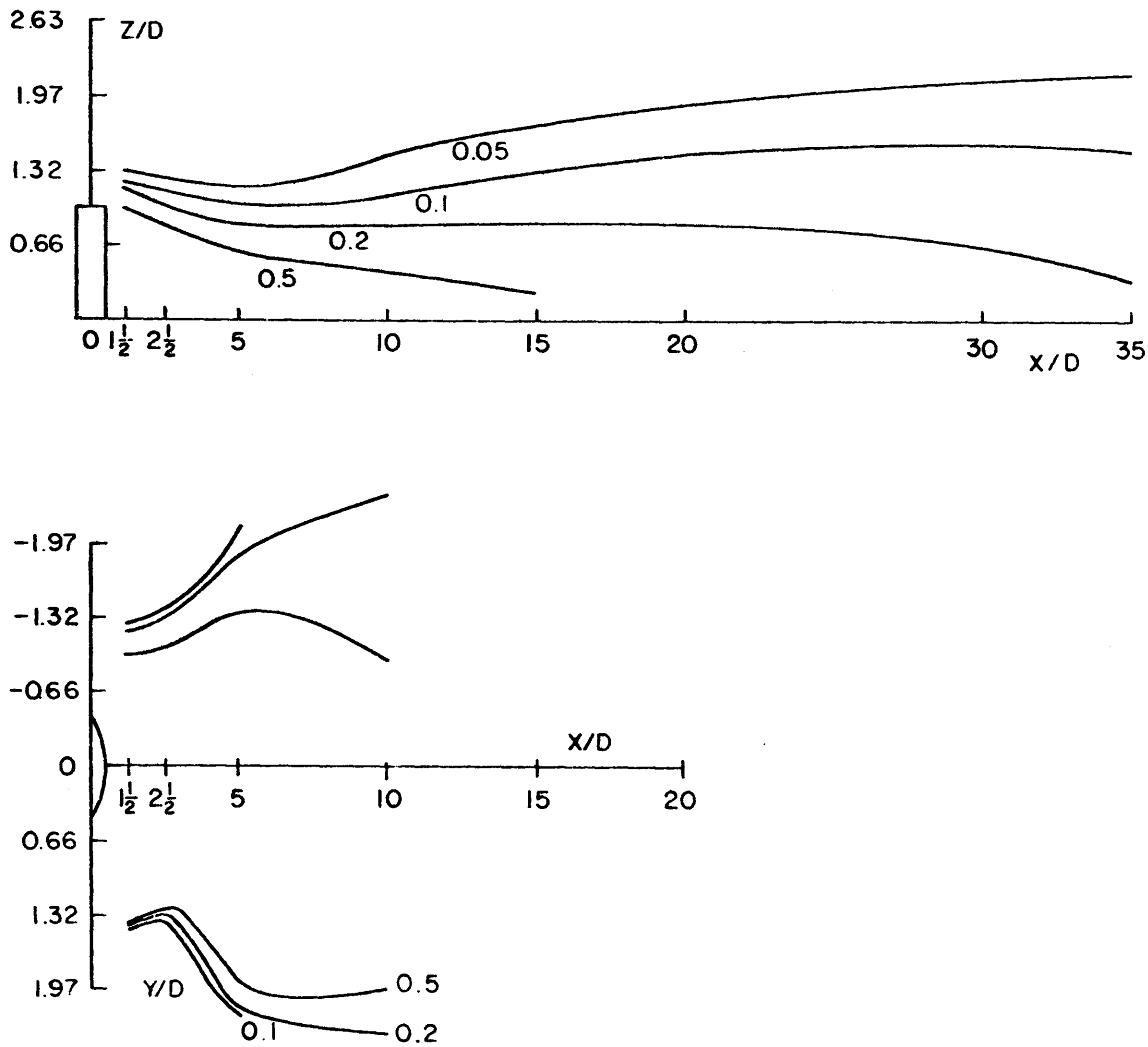

Fig. 80. Cylinder side bottom θ = 90° release.

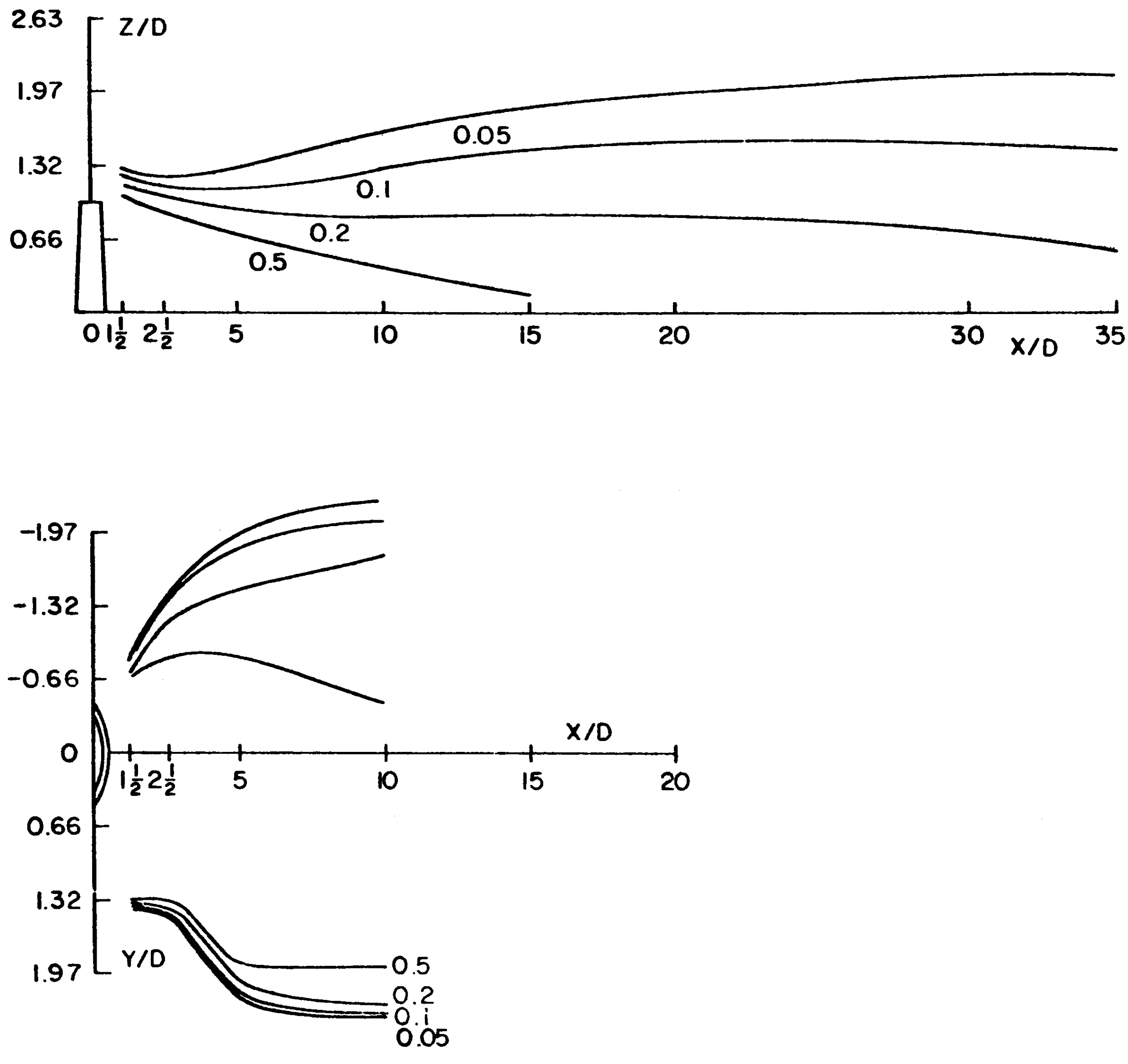

Fig. 81. Frustum 4 side bottom $\theta = 90°$ release.

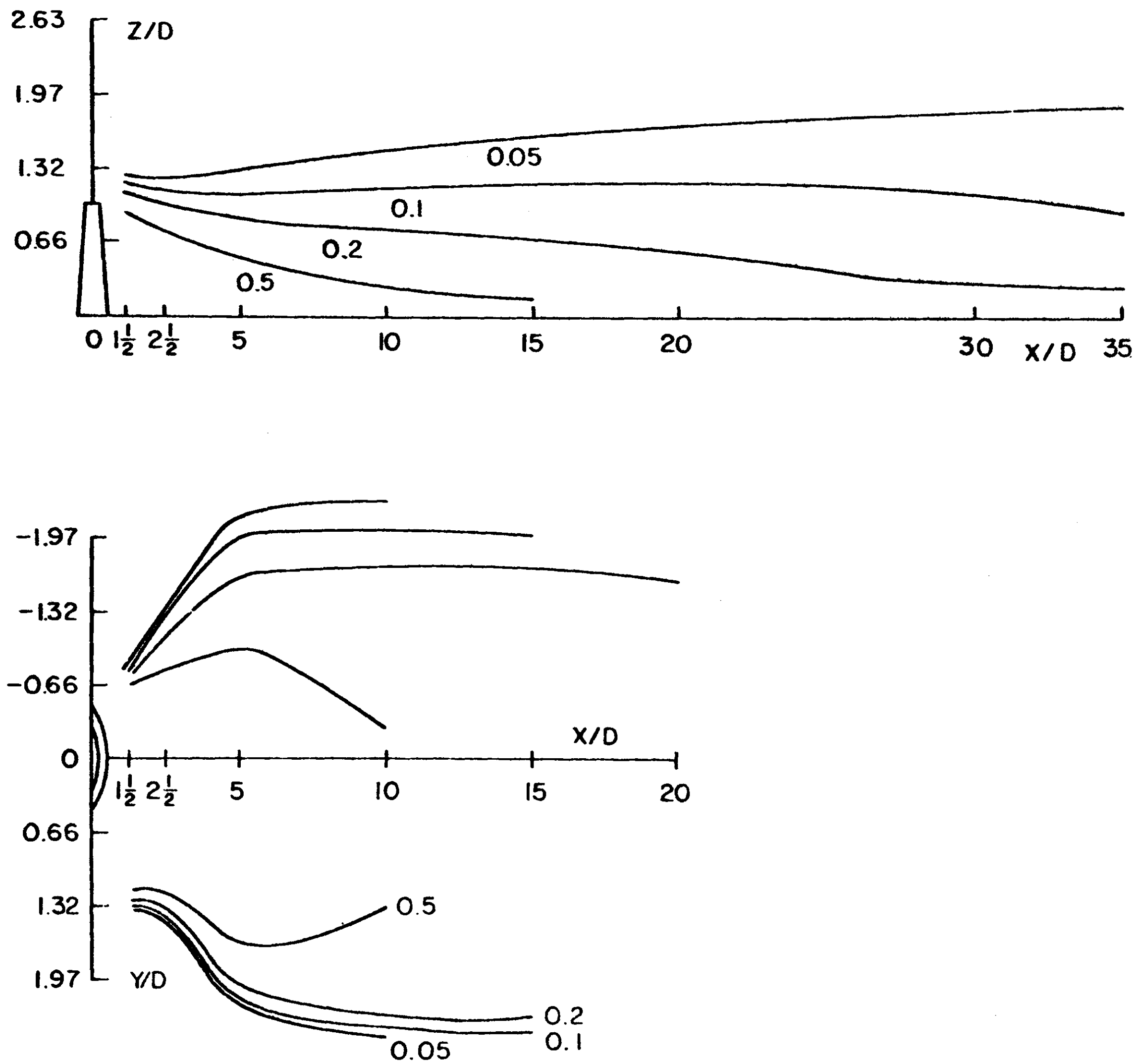

Fig. 82. Frustum 3 side bottom θ = 90° release.

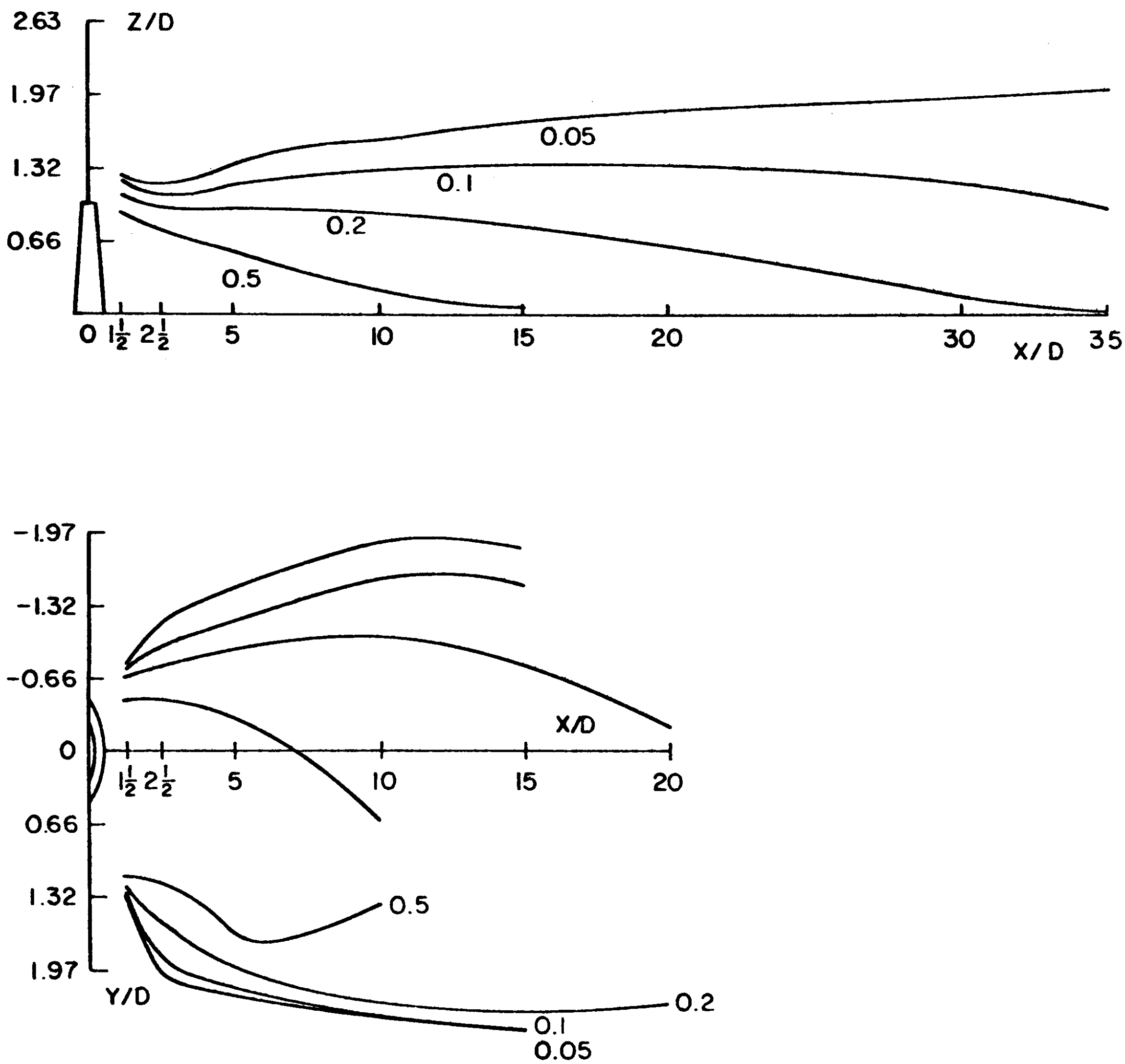

Fig. 83. Frustum 2 side bottom θ = 90° release.

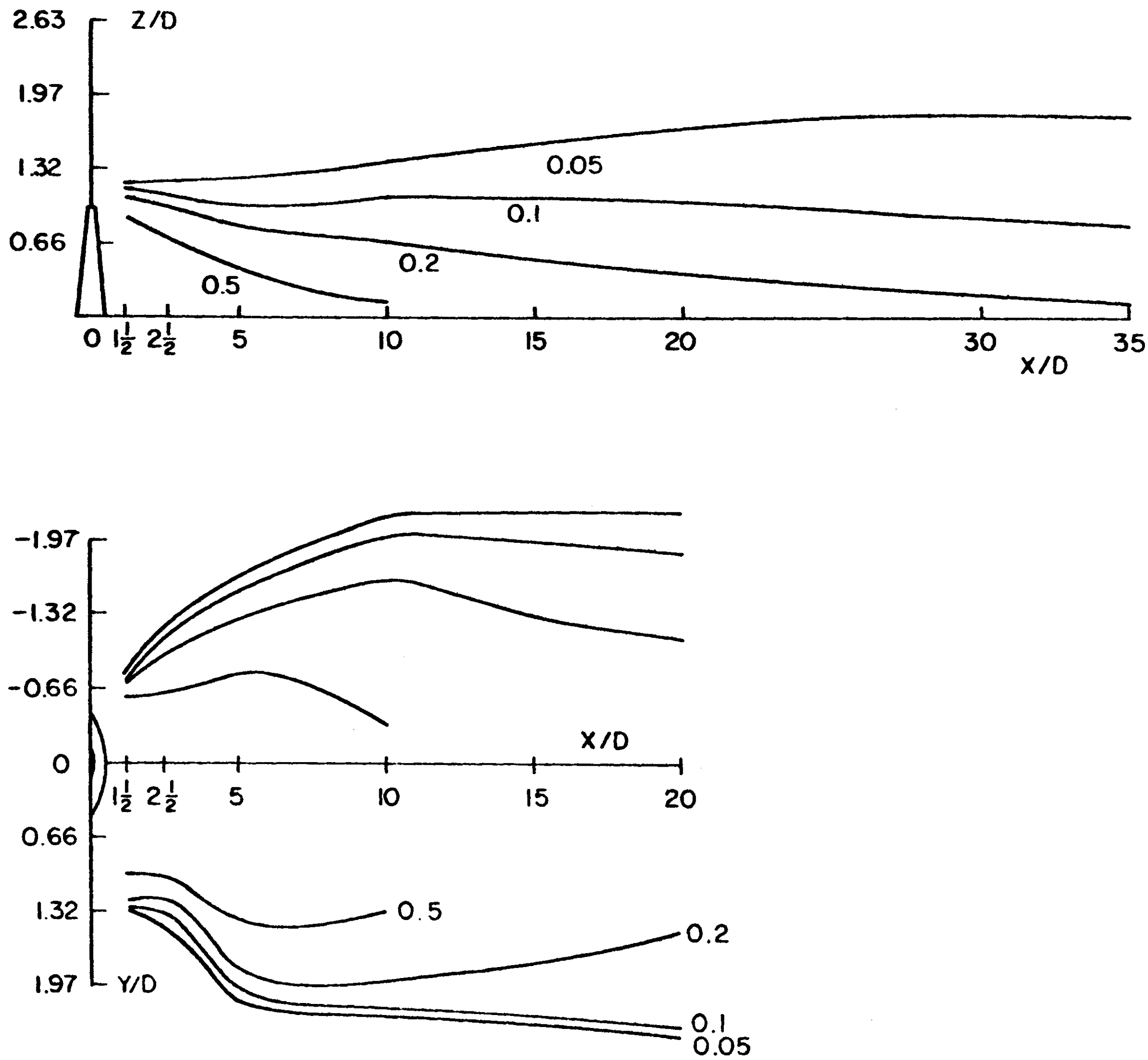

Fig. 84. Frustum 1 side bottom θ = 90° release.

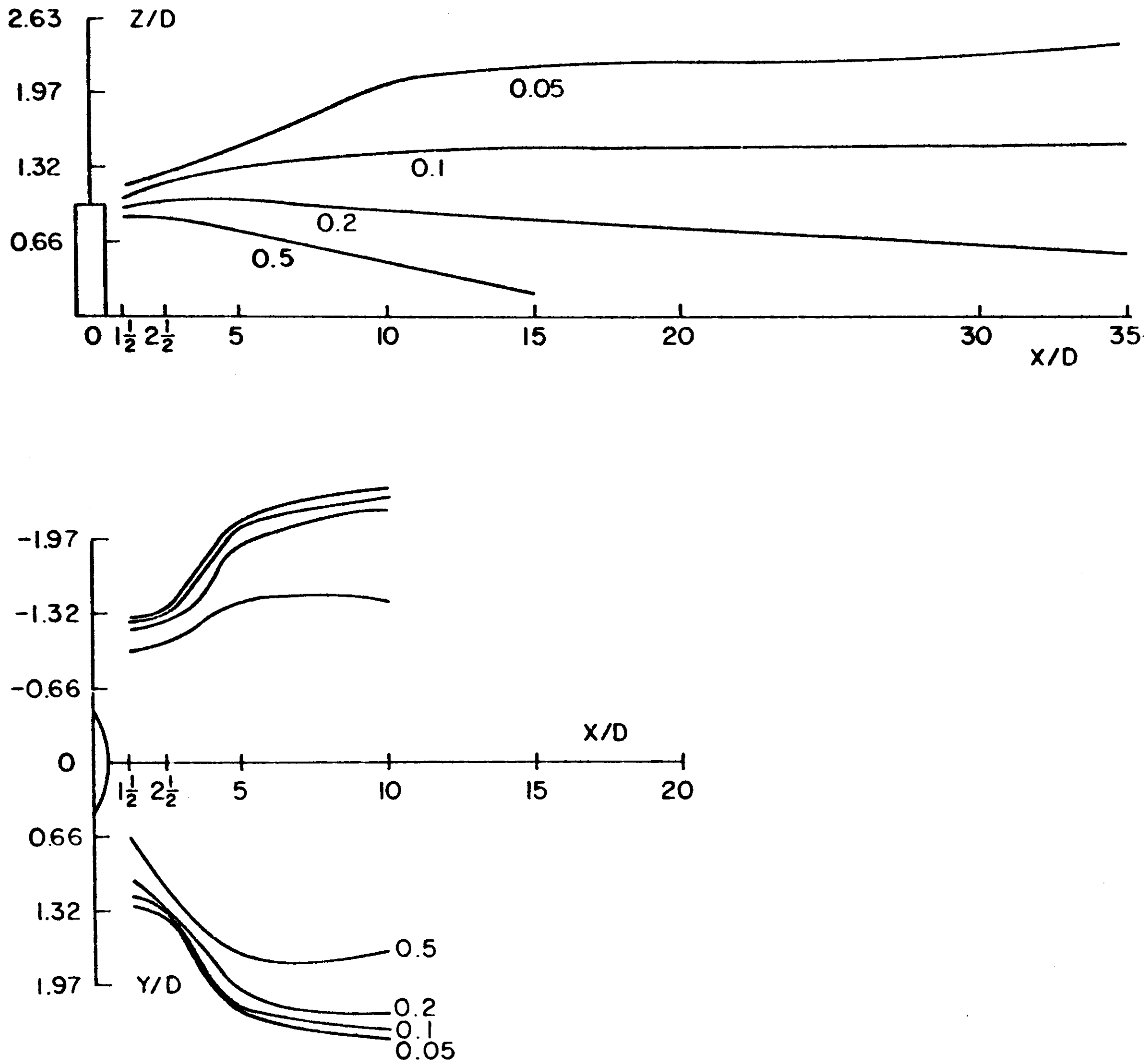

Fig. 85. Cylinder side bottom θ = 180° release.

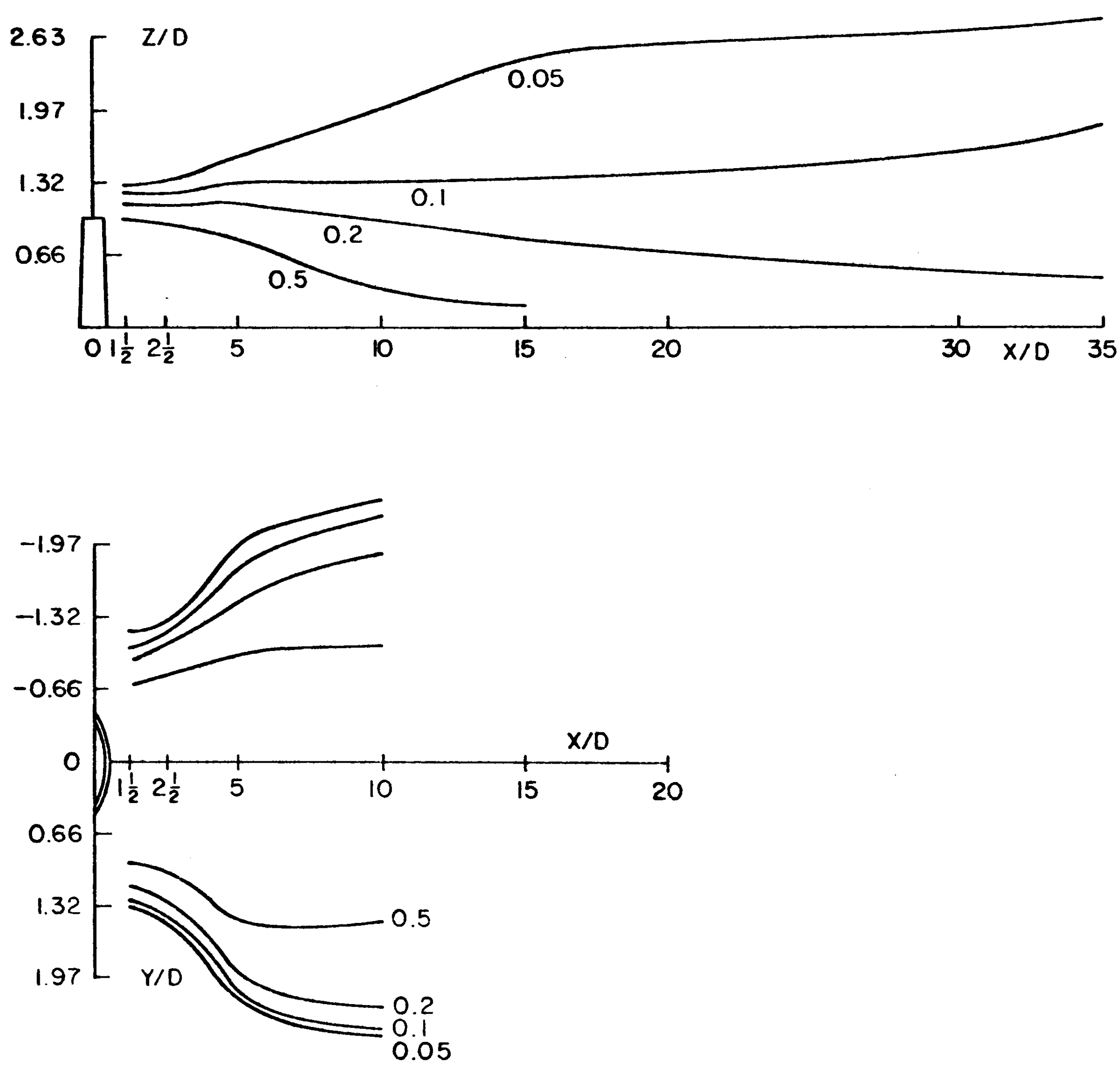

Fig. 86. Frustum 4 side bottom θ = 180° release.

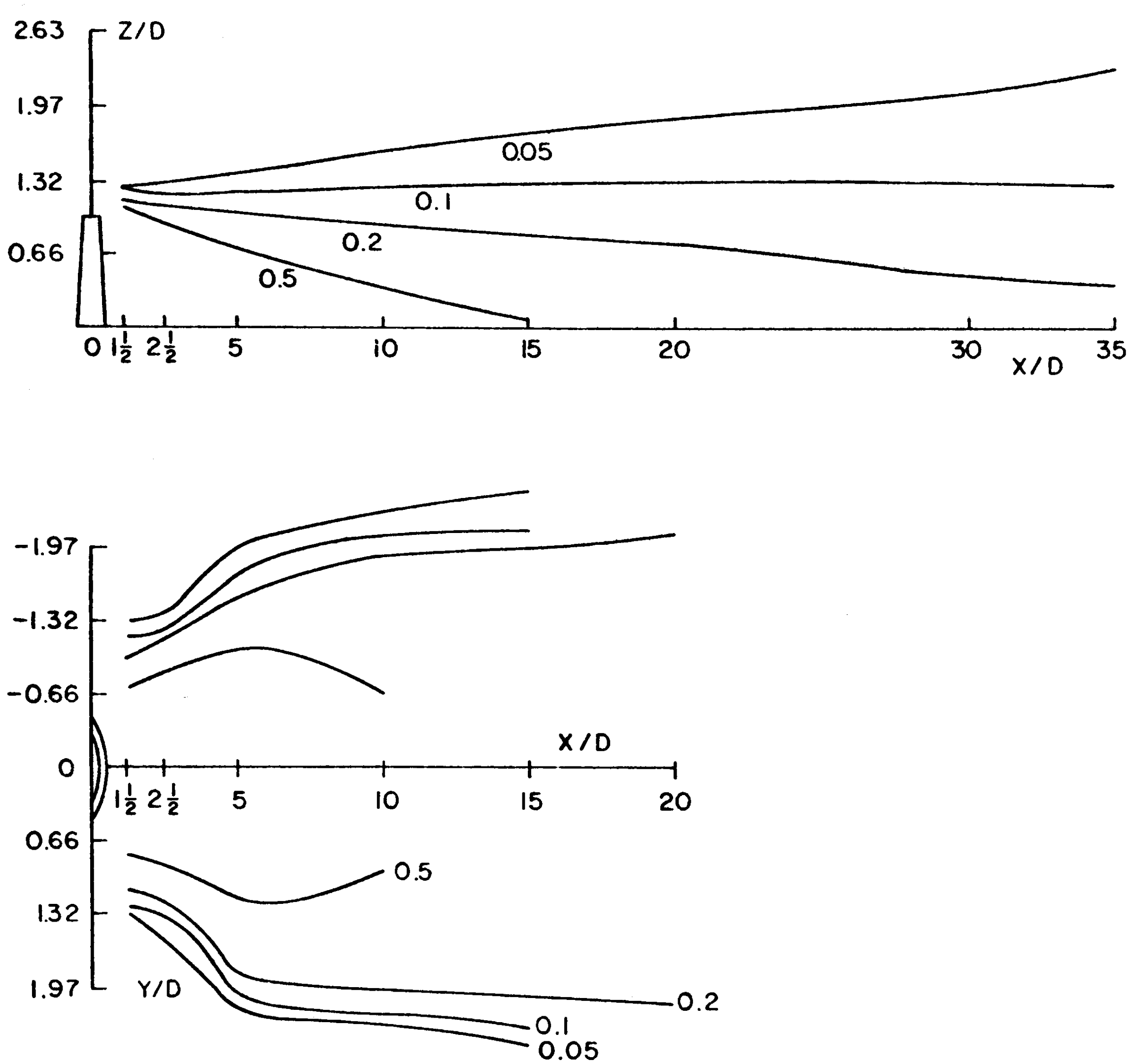

Fig. 87. Frustum 3 side bottom θ = 180° release.

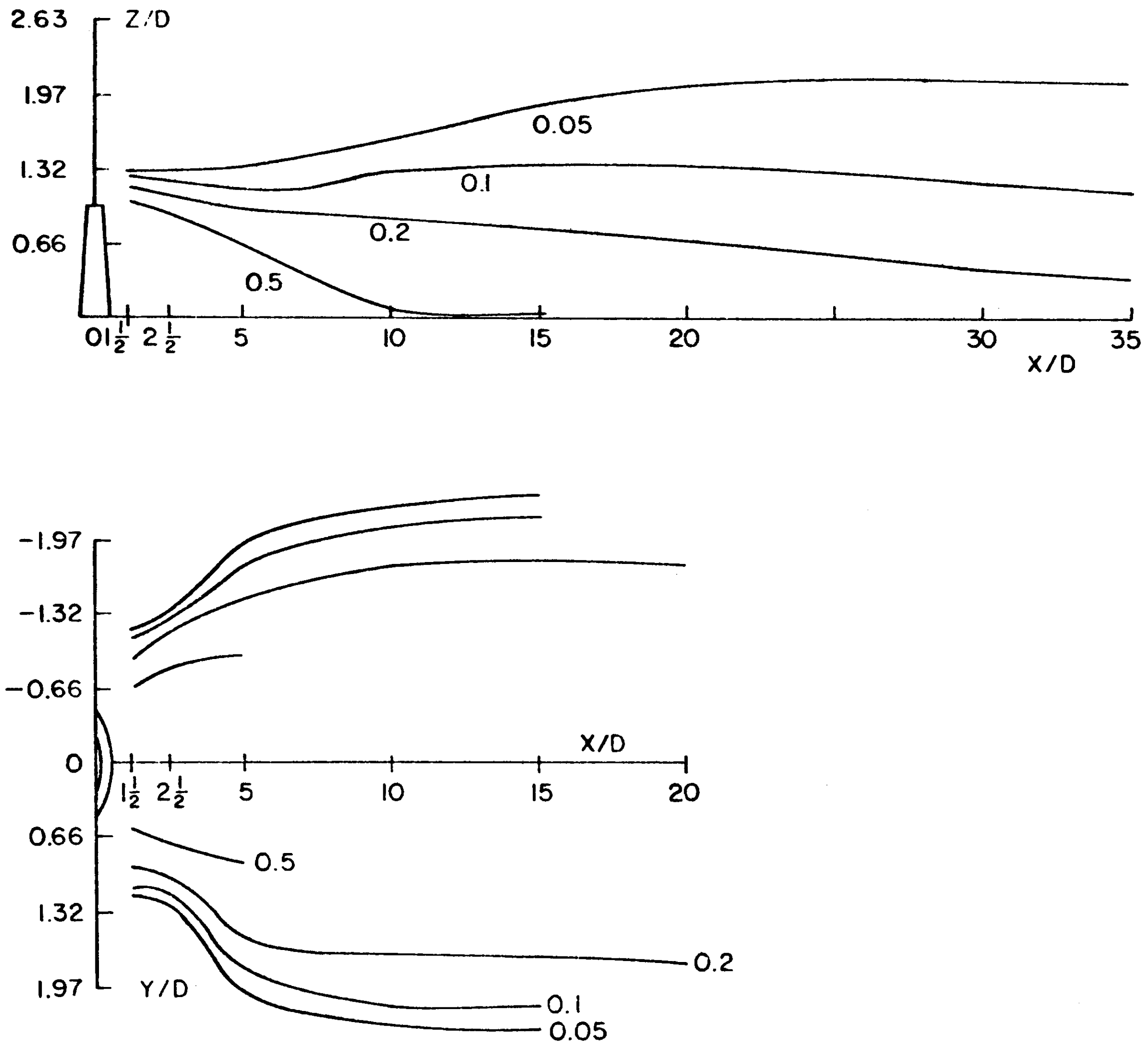

Fig. 88. Frustum 2 side bottom $\theta = 180°$ release.

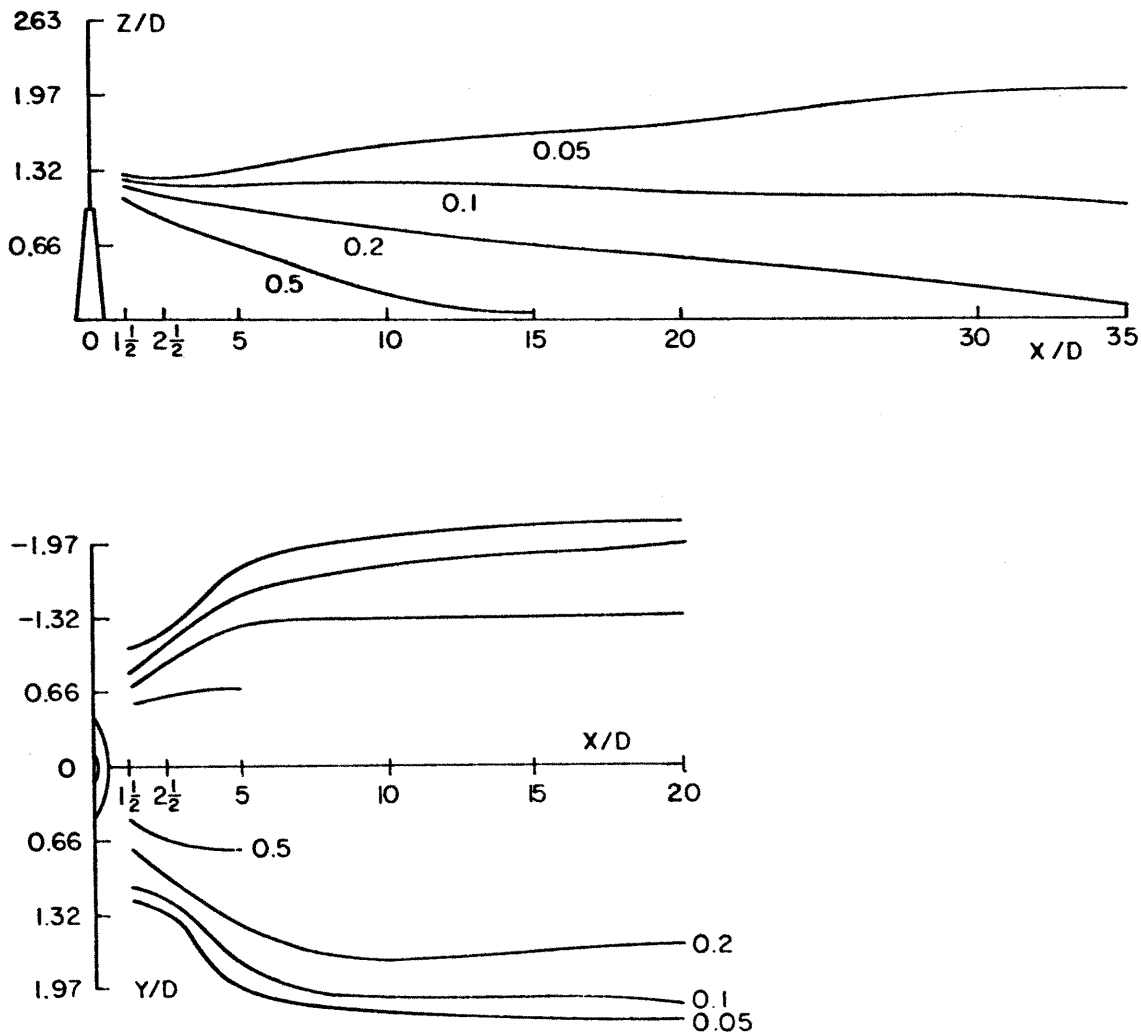

Fig. 89. Frustum 1 side bottom θ = 180° release.

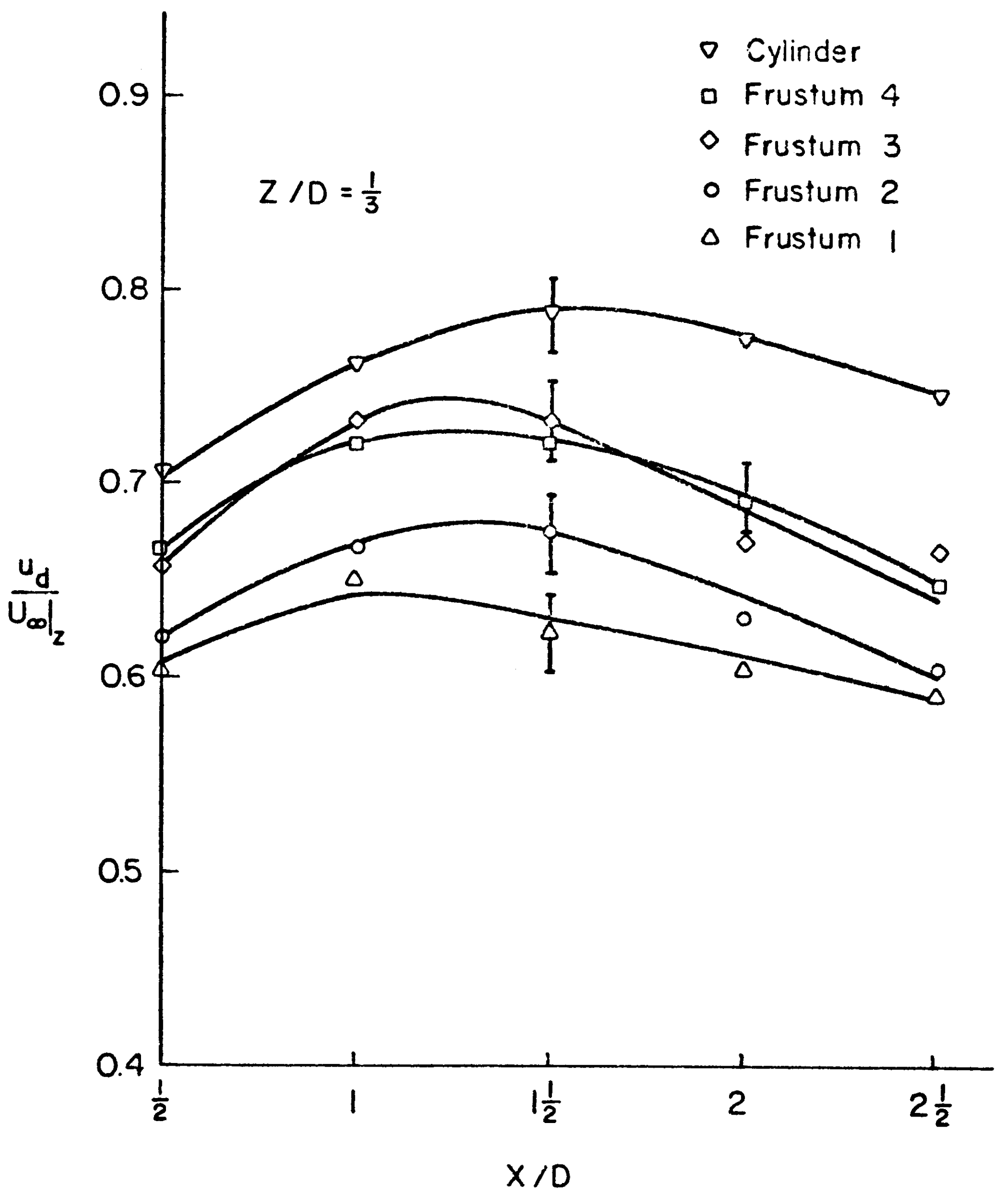

Fig. 90. Wake defect parameter at Z/D = 1/3.

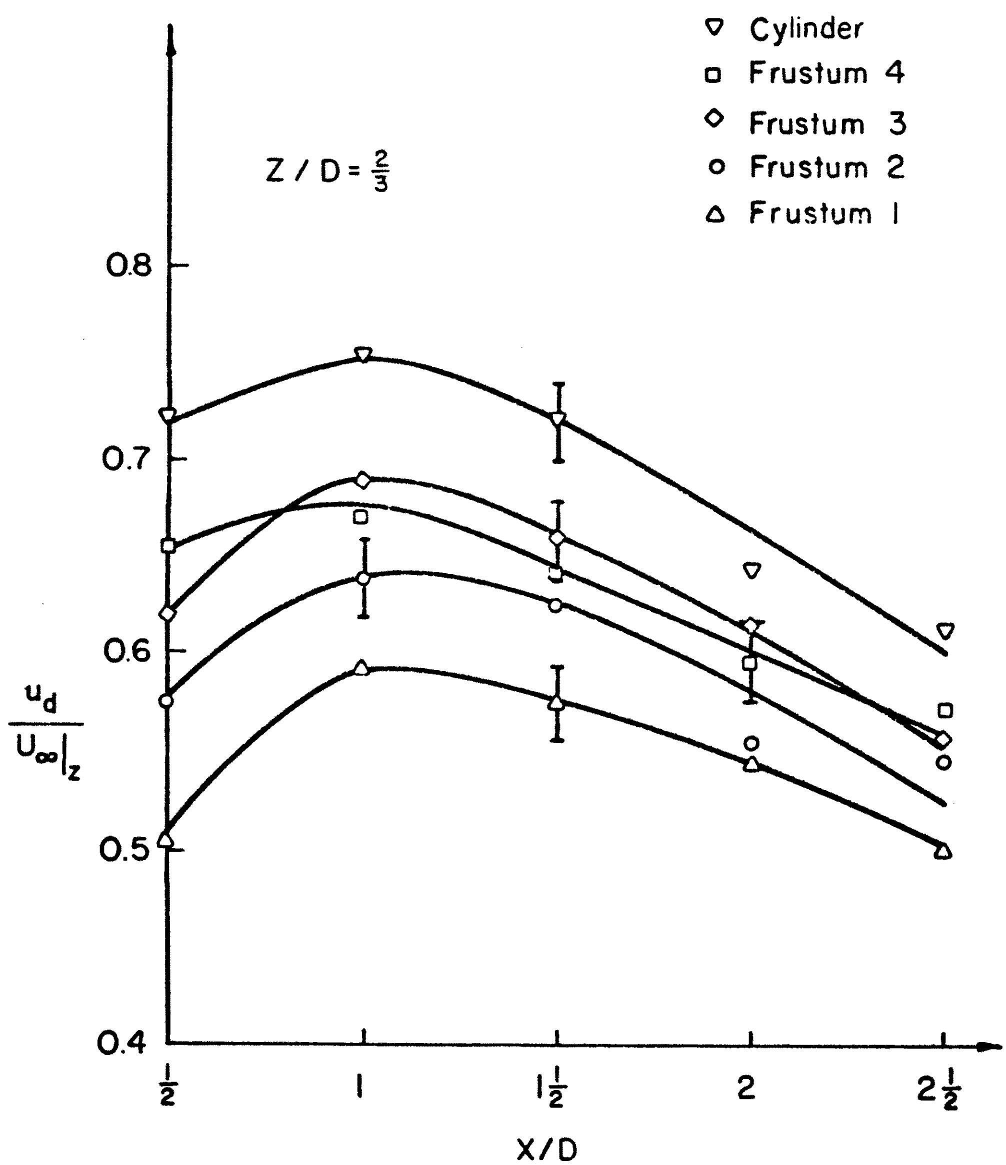

Fig. 91. Wake defect parameter at Z/D = 2/3.

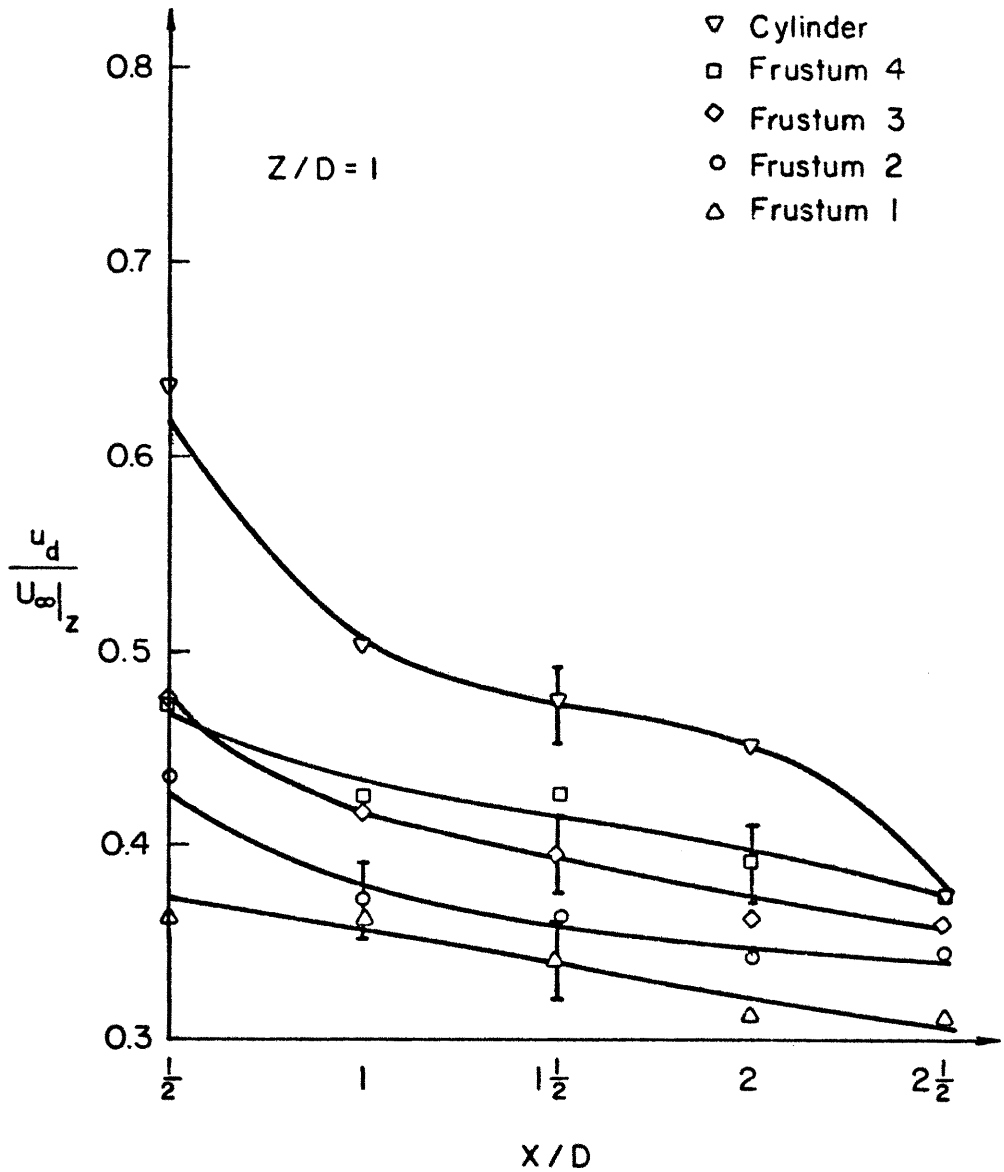

Fig. 92. Wake defect parameter at Z/D = 1.

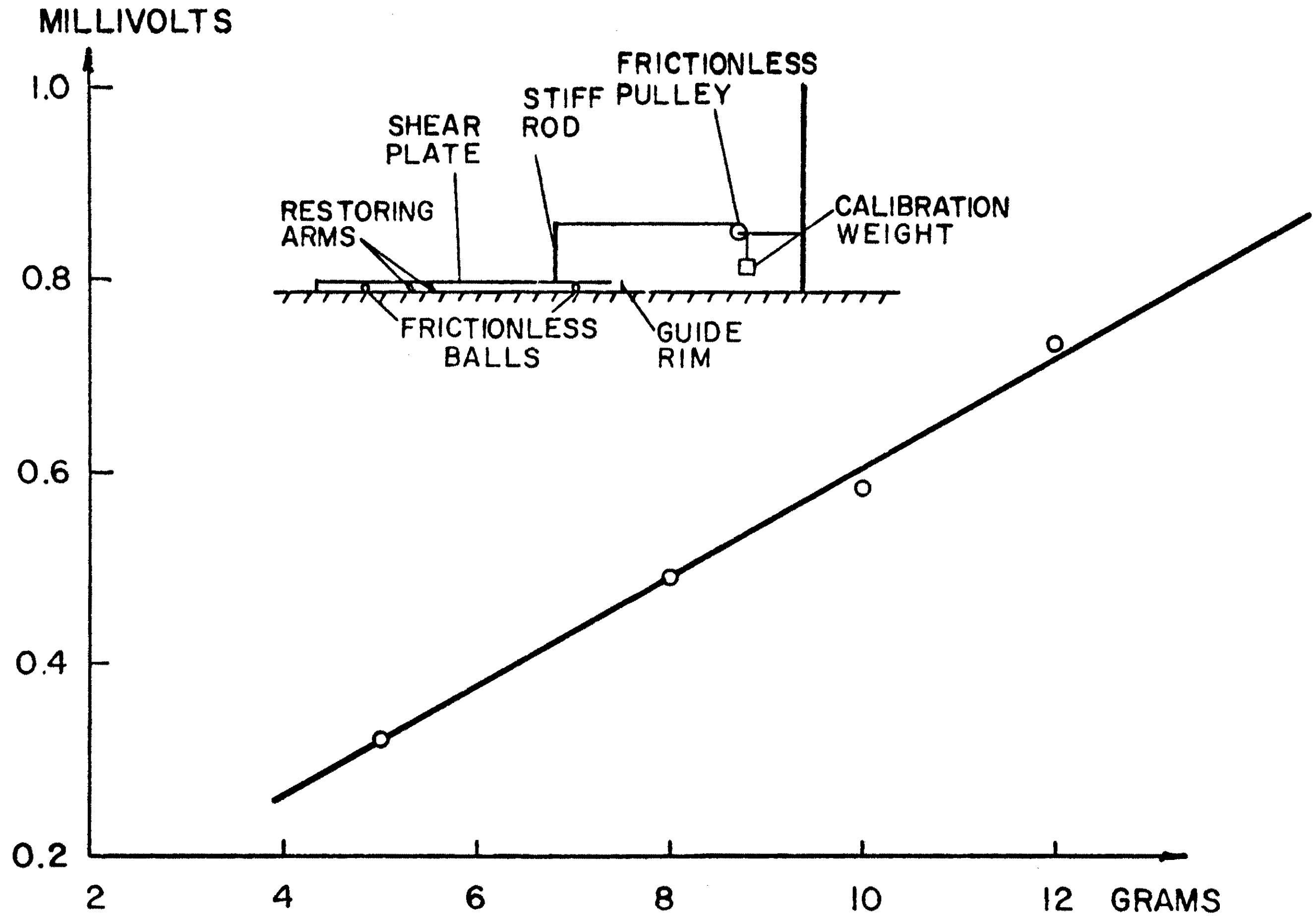

Fig. 93. Shear plate calibration curve.

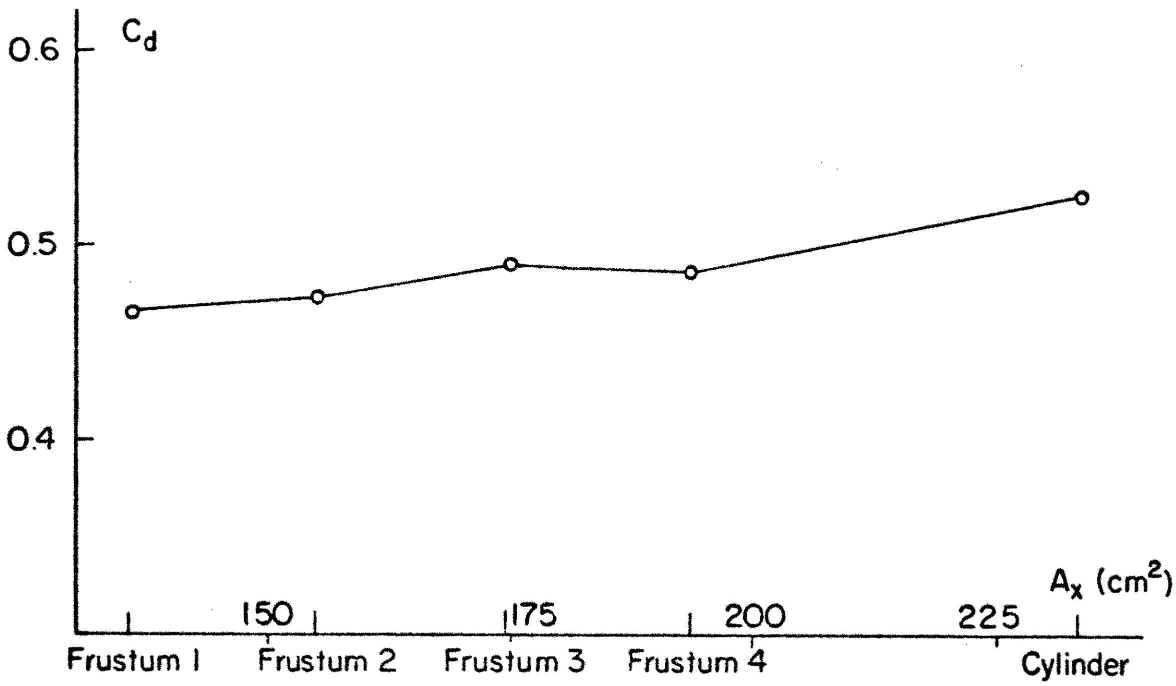

Fig. 94. Drag coefficient for all models.

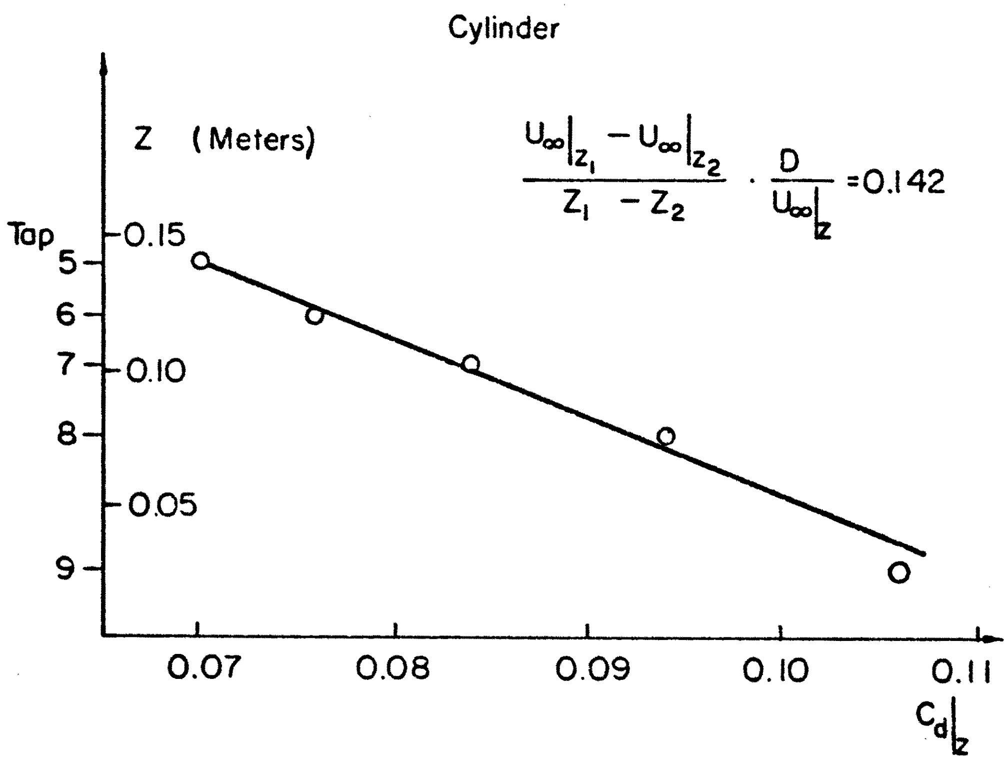

Fig. 95. Cylinder local drag coefficient.

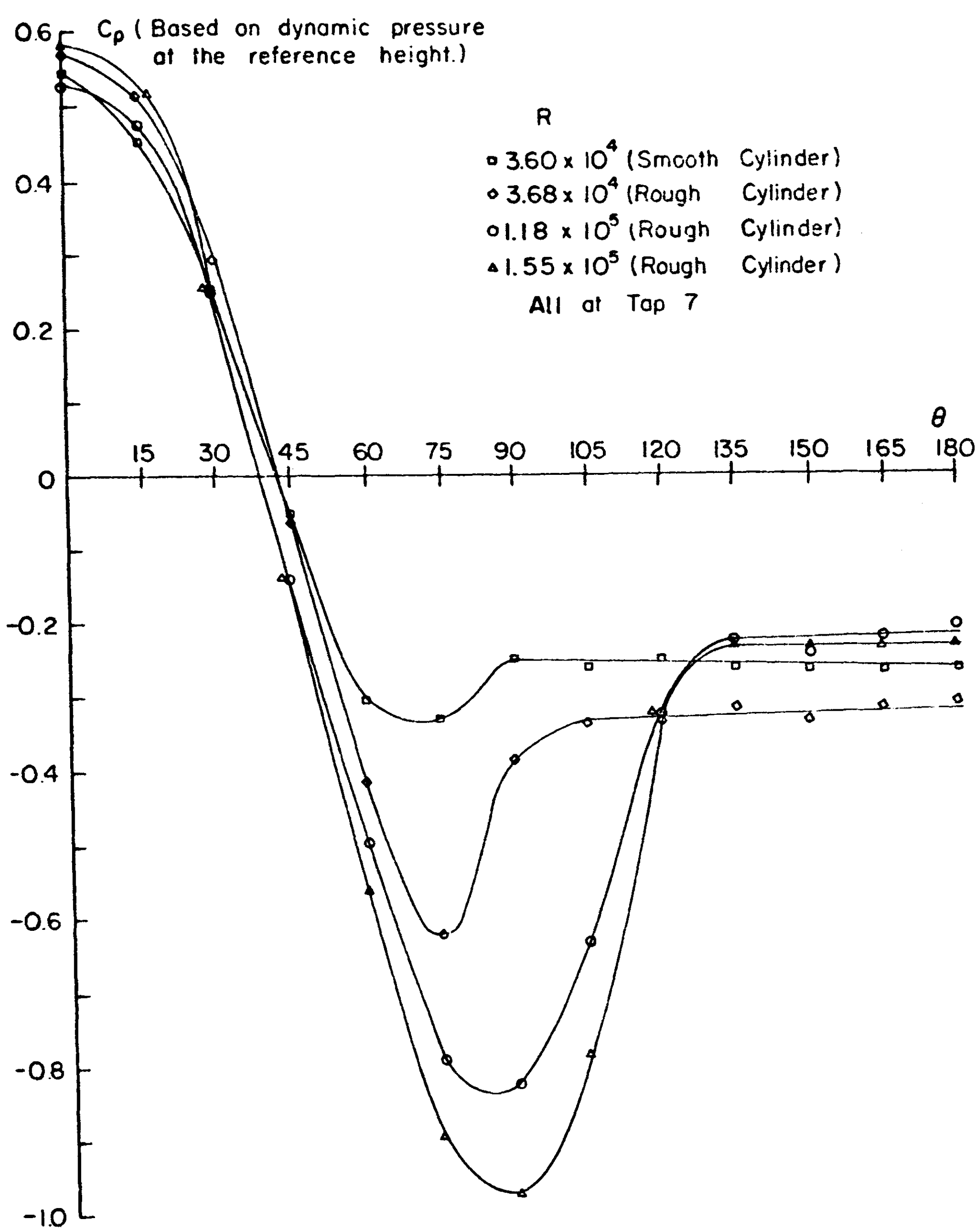

Fig. 96. Pressure coefficient distribution for cylinder at three Reynolds numbers.

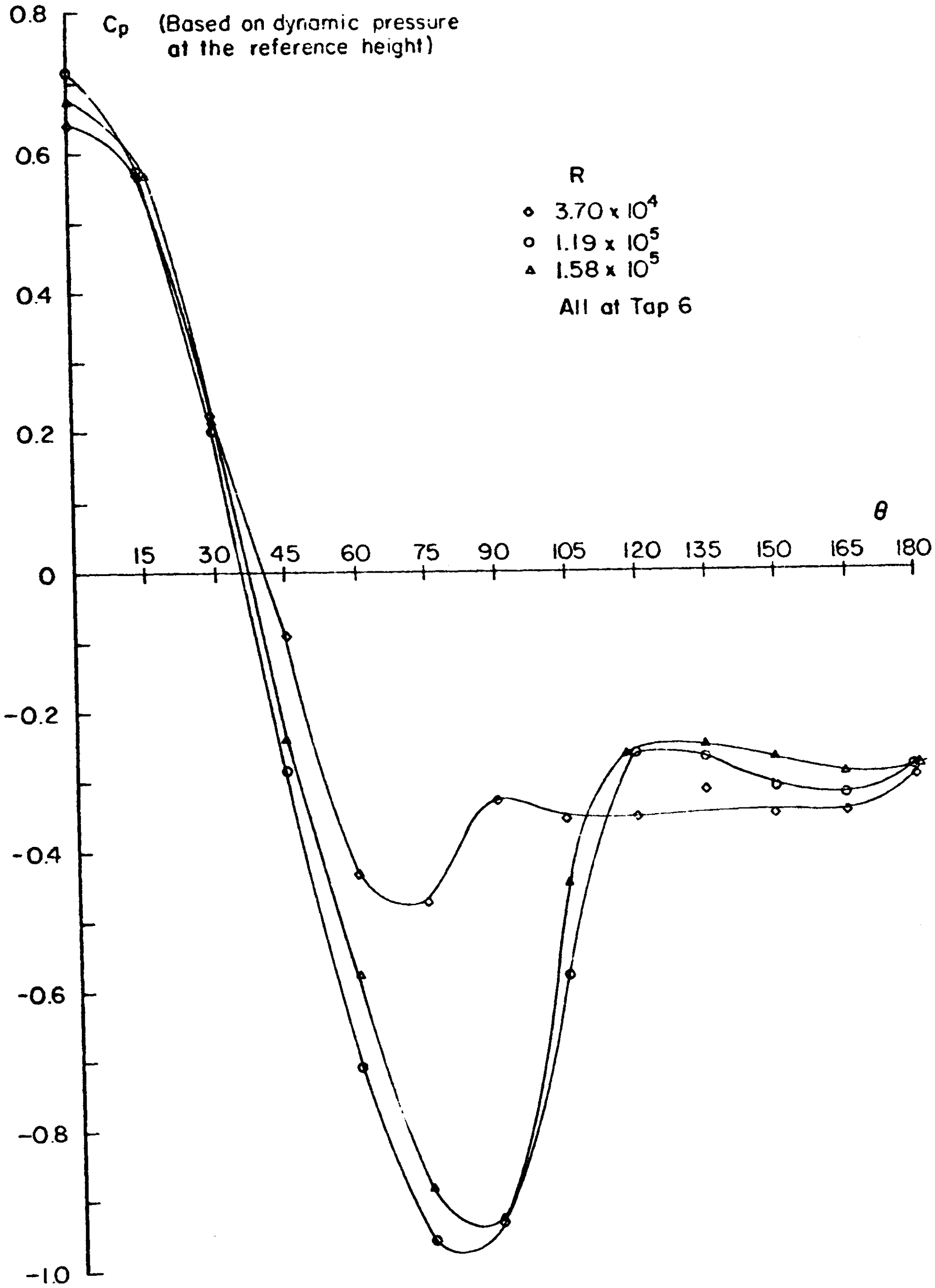

Fig. 97. Pressure coefficient distribution for frustum 4 at three Reynolds numbers.

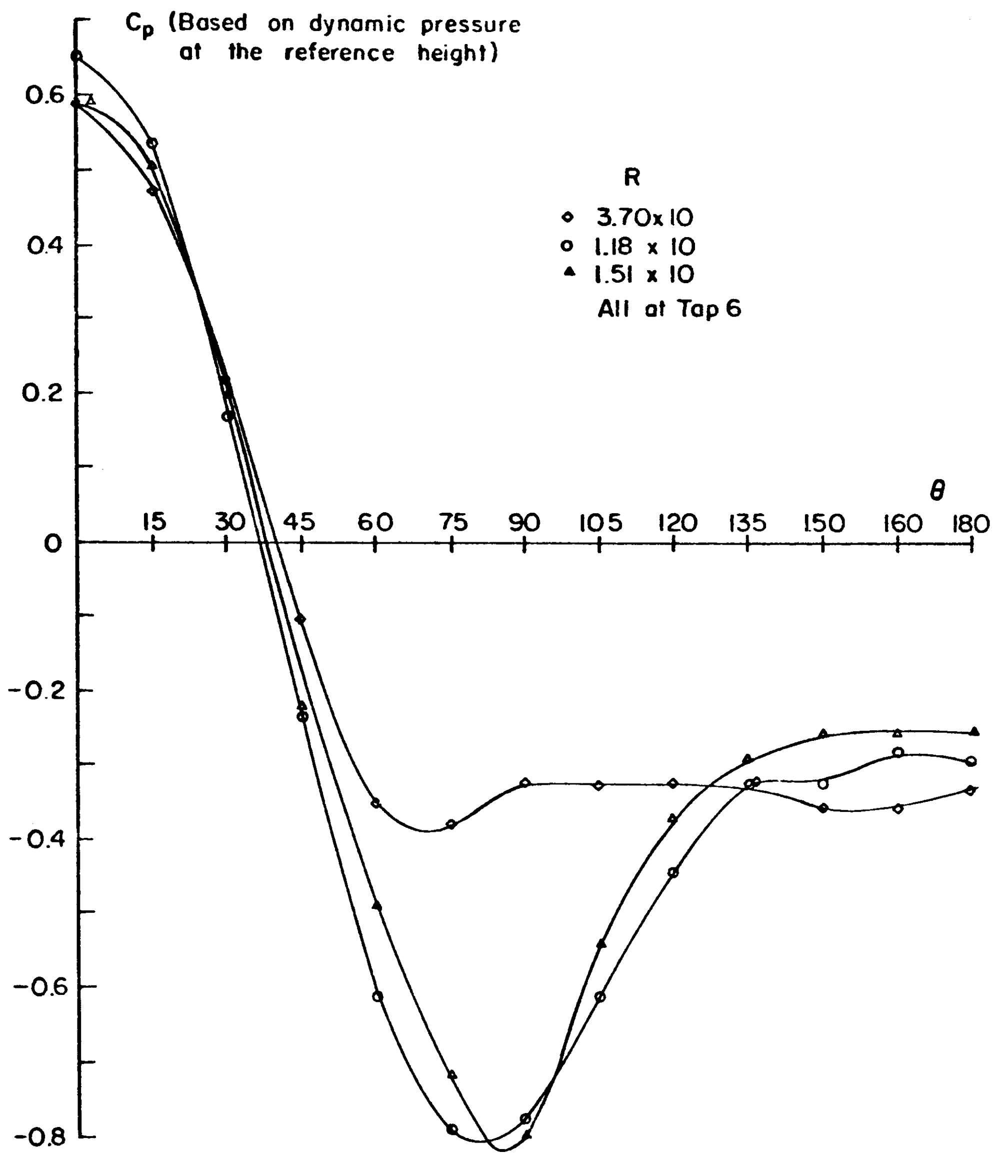

Fig. 98. Pressure coefficient distribution for frustum 3 at three Reynolds numbers.

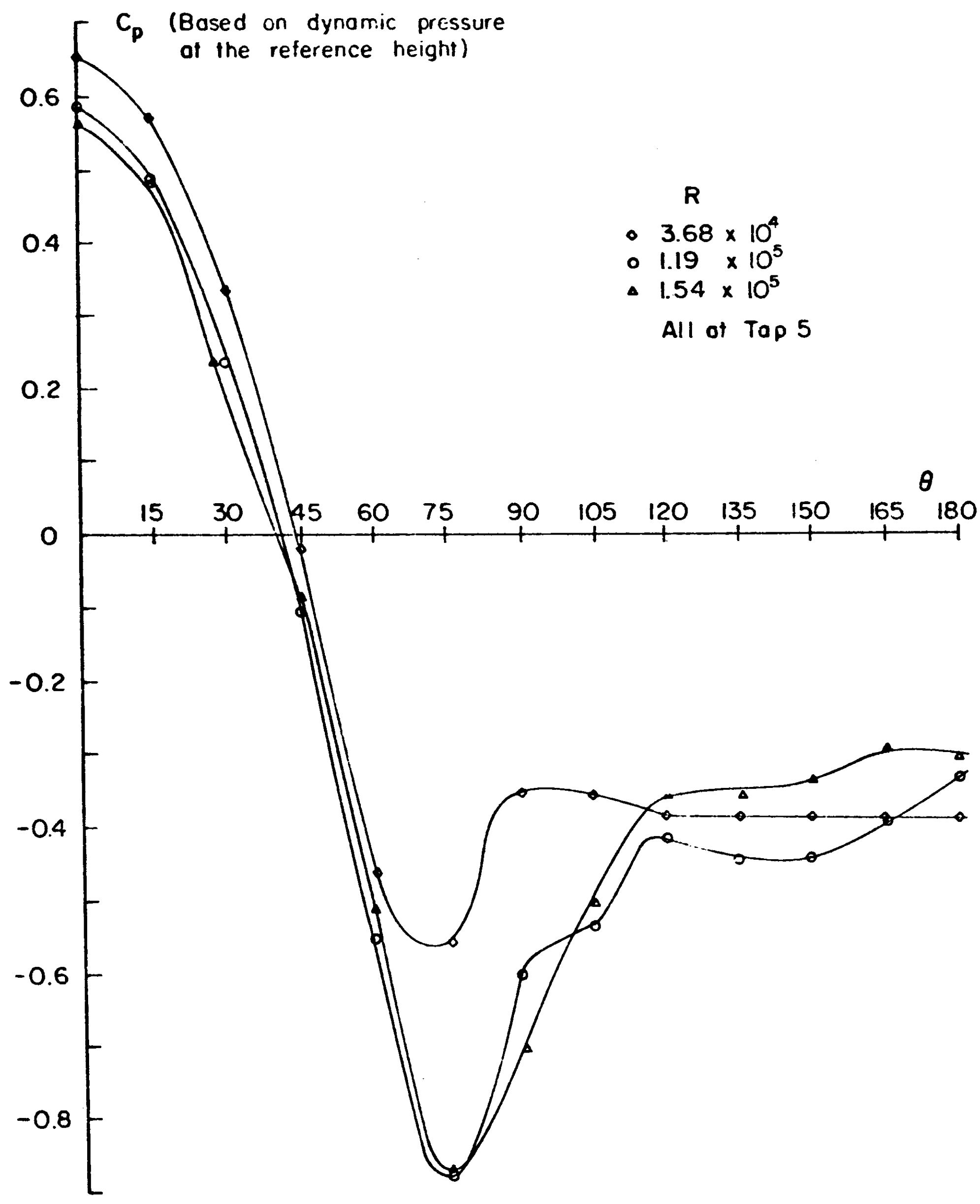

Fig. 99. Pressure coefficient distribution for frustum 2 at three Reynolds numbers.

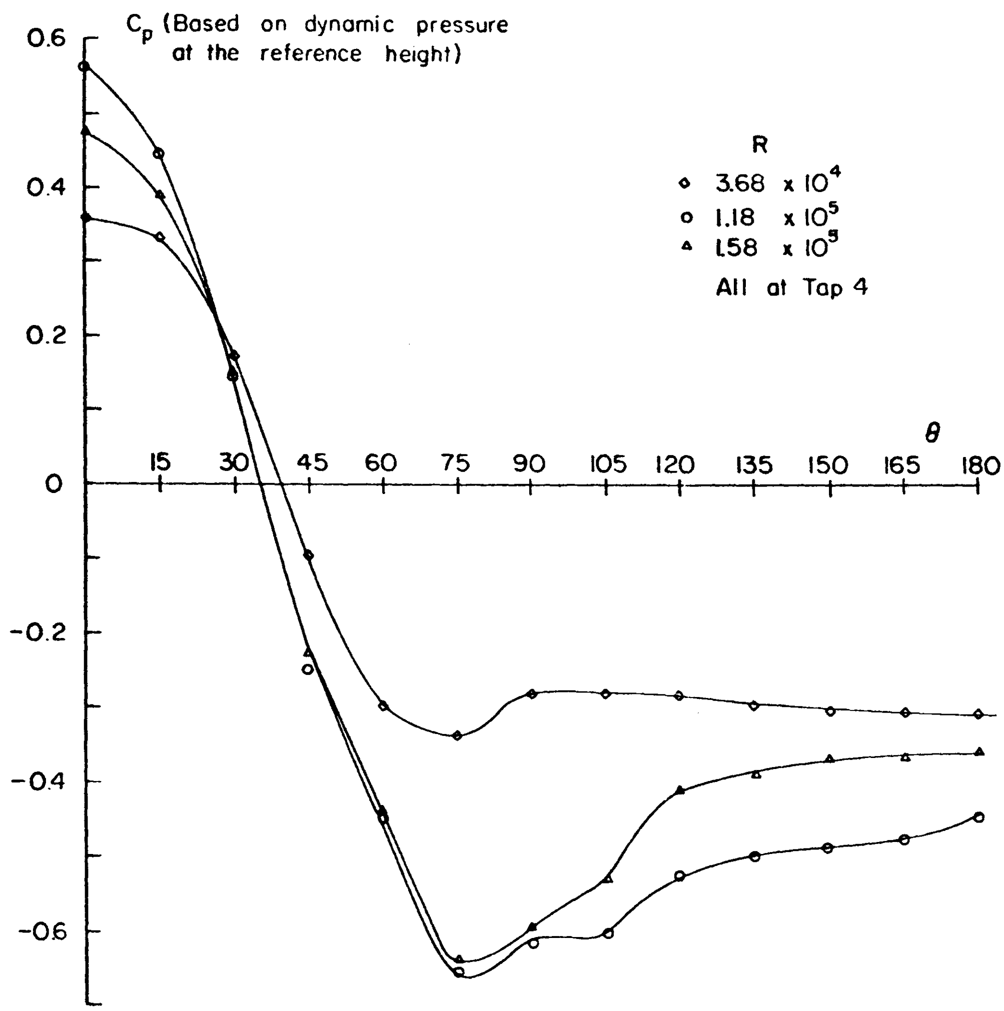

Fig. 100. Pressure coefficient distribution for frustum 1 at three Reynolds numbers.

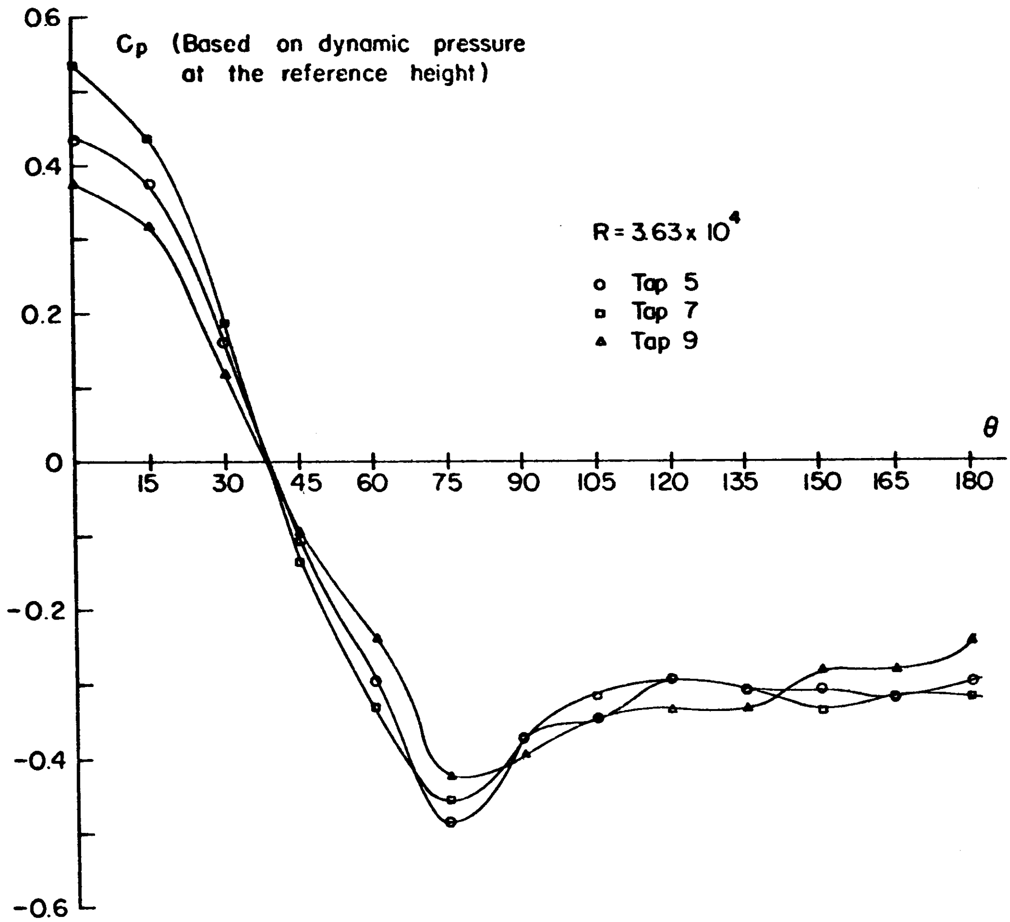

Fig. 101. Pressure coefficient distribution down side of rough cylinder.

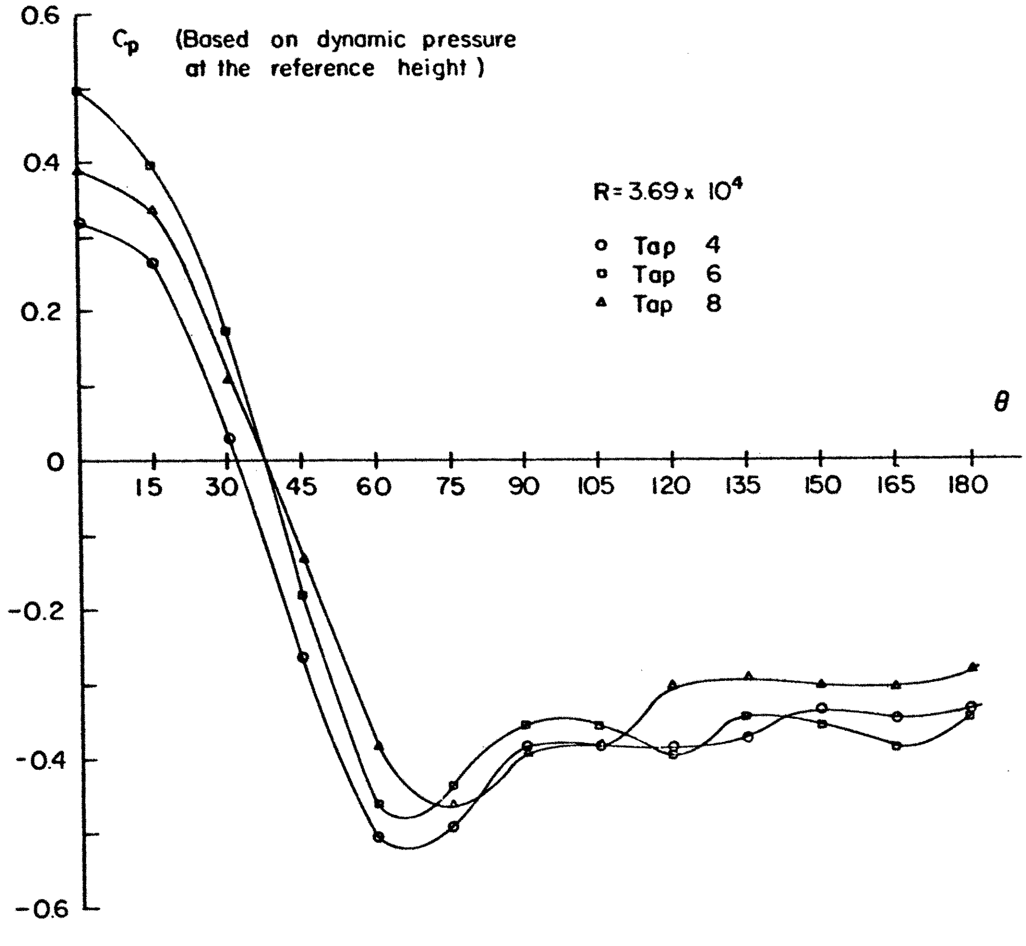

Fig. 102. Pressure coefficient distribution down side of frustum 4.

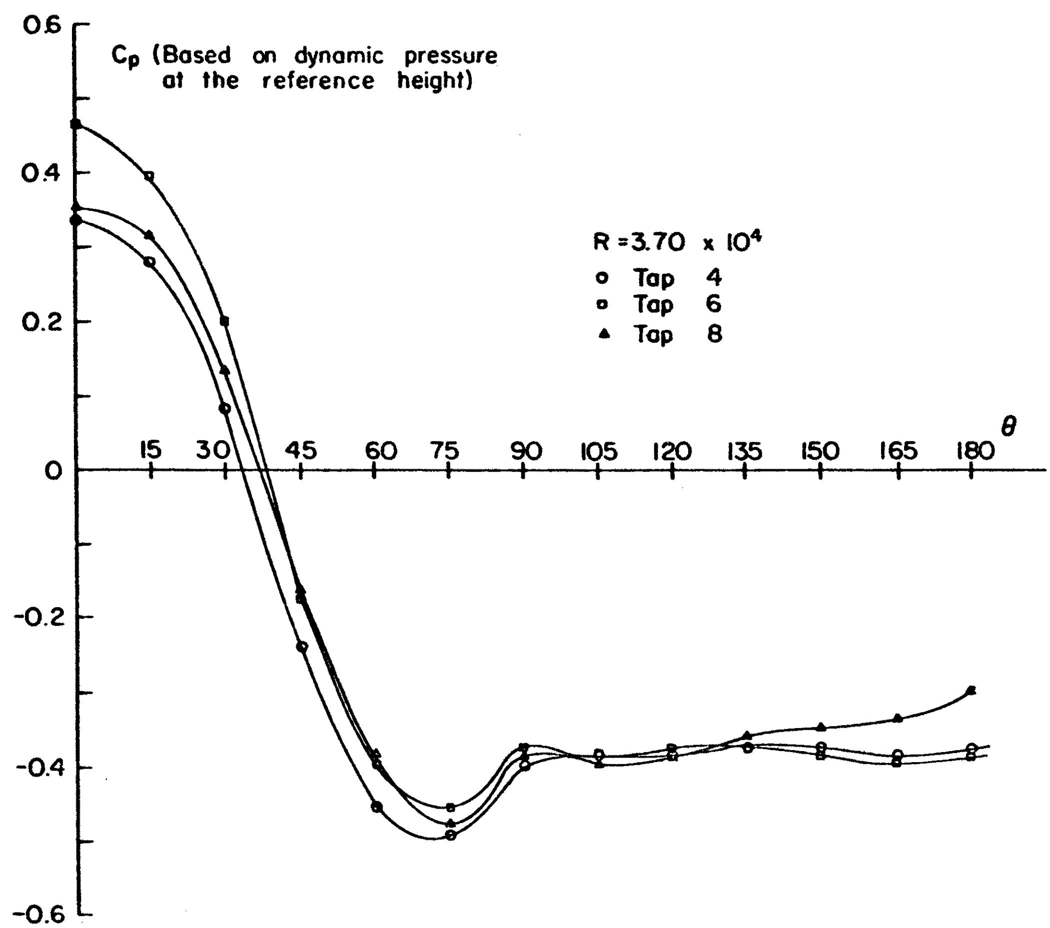

Fig. 103. Pressure coefficient distribution down side of frustum 3.

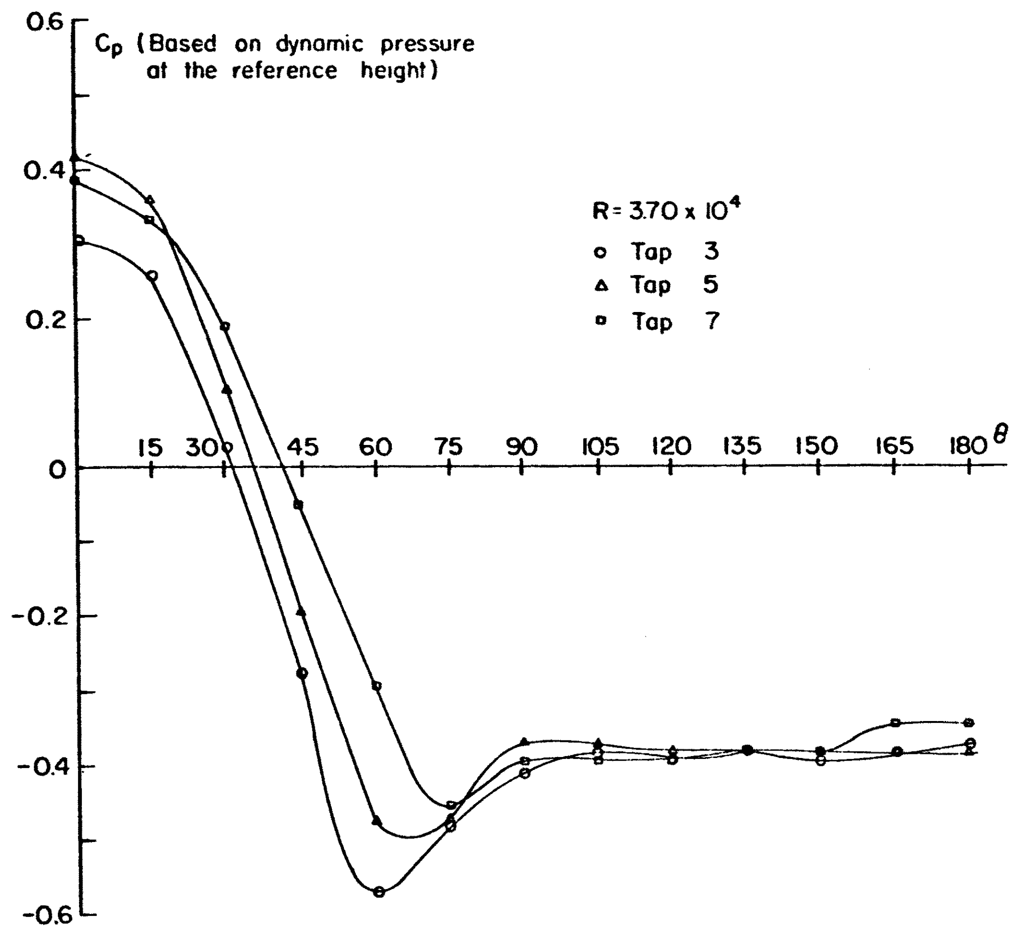

Fig. 104. Pressure coefficient distribution down side of frustum 2.

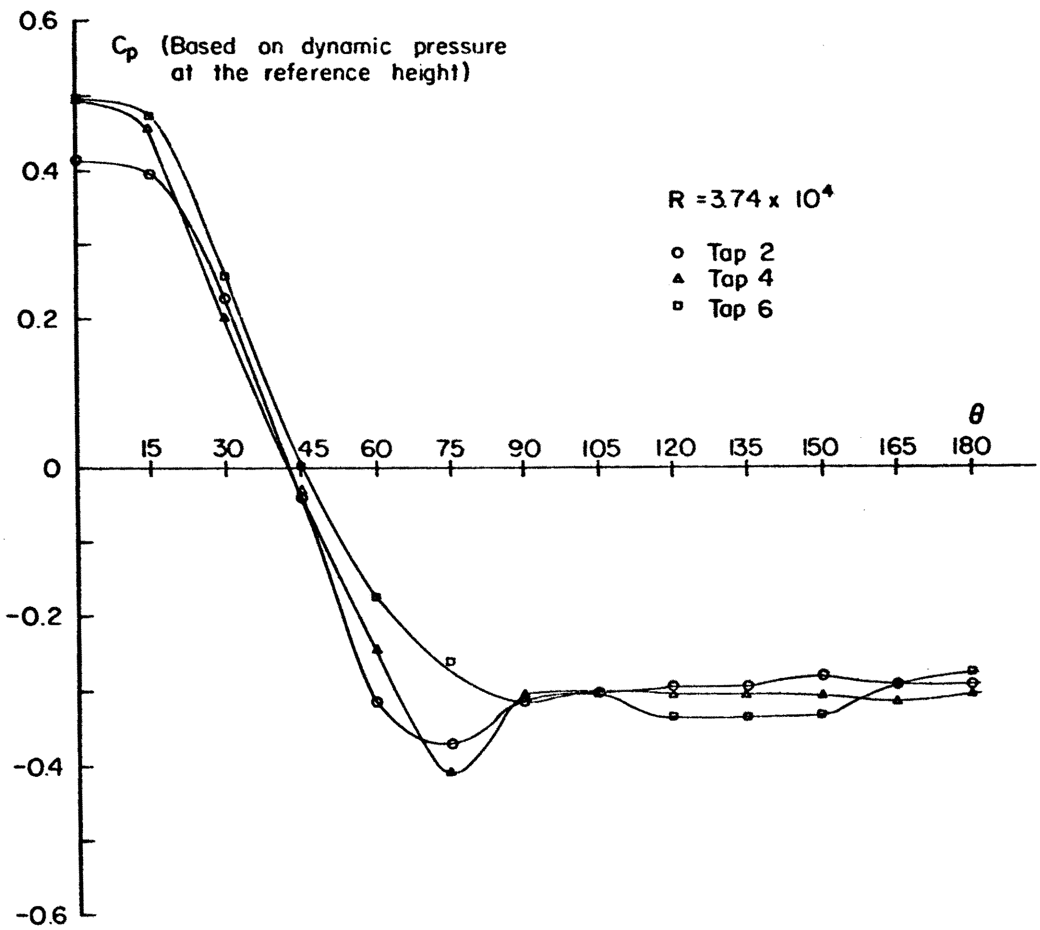

Fig. 105. Pressure coefficient distribution down side of frustum 1.